Developing Multifunctional Surface Chemistry for Plasmonic Biosensing in Complex Media

Fang Sun

A dissertation

submitted in partial fulfillment of the

requirements for the degree of

Doctor of Philosophy

University of Washington

2016

Reading Committee:

Shaoyi Jiang, Chair

Qiuming Yu, Co-Chair

Daniel M. Ratner

Program Authorized to Offer Degree:

Chemical Engineering

University of Washington

Abstract

Developing Multifunctional Surface Chemistry for Plasmonic Biosensing in Complex Media

Fang Sun

Chair of the Supervisory Committee:

Professor Shaoyi Jiang

Chemical Engineering

During the past decades, plasmonic sensors have been explored extensively due to their ultra-sensitivity and emerged as a new generation of analytical tools. Two of the most widely used and studied plasmonic sensors are surface enhanced Raman scattering (SERS) sensors and surface plasmon resonance (SPR) sensors, which are focused in this dissertation. SERS is a phenomenon which can significantly magnify the Raman signals of the molecules adsorbed on a nanostructured metal surface for up to millions of folds and have led to the detections of single molecules. SERS can also provide chemical fingerprints representing vibrational or rotational transitions specific to the molecular structure to identify the analyte. The SPR optical sensor can enable the direct observation

of molecular interaction in real-time and offer the benefits of rapid, sensitive and label-free detection of chemical and biological species. Based on these advantages such as ultra-sensitivity and molecular specificity, both of the sensors have already been used for a variety of applications ranging from chemical and biological sensing, environmental monitoring to diagnostics.

However, reliable biosensing in complex biological media based on these two advanced plasmonic sensors is still very challenging due to several reasons. For example, SERS is a near-field effect; the enhancement effect decreases exponentially with increasing distance from the surface. A bare SERS-active surface lacks selectivity; anything adsorbed onto the surface can be detected. In the complex media, the background noise from interfering species could mask the signals from target analytes. In addition, nonspecific adsorption from the complex media could impede the adsorption of target analytes to SERS-active substrate surfaces. Thus, a method which can amplify the detection signals over unwanted background is highly desirable and it is also essential to introduce nonfouling modifications to protect the SERS-active surface from nonspecific adsorption. For an SPR sensor, the specificity of the SPR sensor is totally dependent on the biomolecular recognition species employed while the sensitivity depends on the amount of nonspecific binding. Thereby, the surface chemistry which can not only effectively resist nonspecific protein adsorption but also provides abundant sites for the ligand immobilization is desired.

In this dissertation, we discuss the design and selection of probe molecules on the SERS surface for specific detection and signal amplification of target analytes with small Raman activity or no activity such as fructose or hydrogen ion. In addition, to overcome

the protein fouling problem, we introduce a zwitterionic nonfouling surface modification to the SERS sensor. We design and synthesize a zwitterionic short thiol, which contains a carboxybetaine head group resisting the protein adsorption effectively. The CBT possesses a small Raman activity generating negligible background noise even with high packing density. To future improve the nonfouling property of the modification, we also introduce the zwitterionic poly(carboxybetaine acrylamide) (pCBAA) polymer brush on the SERS surface via surface-initiated atom transfer radical polymerization (SI-ATRP). This modification enables the SERS detection of several therapeutic drugs directly in the human undiluted plasma. For the SPR sensor, we develop a facile and stable nonfouling coating method based on the zwitterionic hydrogel. The hydrogel coating demonstrate ultra-low fouling property from the undiluted blood serum and high antibody loading capacity due to the three-dimensional structure. At last, we also propose a new method to detect the anti-PEG antibody in blood sample based on the PEG coated SPR sensor. The surface chemistry is studied and optimized to achieve an extremely low limit of detection showing better sensitivity compared with traditional ELISA detection methods.

By tailoring and tuning the surface chemistry, we explore and expand the applications of the plasmonic sensor in complex media. On the one hand, we introduce the attracting and probing molecules to enhance the detection signals. And on the other hand, we modify the zwitterionic nonfouling materials on the surface of sensors to decrease the background noise and interference. With the improved signal/noise ratio, the sensitivity of sensors can be dramatically increased.

Table of Contents

Abstract iii

List of Tables ix

List of Schemes ix

List of Figures x

Acknowledgements xiii

Chapter 1 Introduction 1

Chapter 2 Sensitive and Fast Detection of Fructose in Complex Media via Symmetry Breaking and Signal Amplification Using SERS 7

2.1 Introduction 7

2.2 Experimental Section 10

2.3 Results and Discussion 13

2.4 Conclusions 21

2.5 Tables 22

2.6 Figures 23

Chapter 3 Functionalized Plasmonic Nanostructure Arrays for Direct and Accurate Mapping Extracellular pH of Living Cells in Complex Media Using SERS 33

3.1 Introduction 33

3.2 Experimental Section 36

3.3 Results and Discussion 38

3.4 Conclusions 43

3.5 Tables 44

3.6 Figures 45

Chapter 4 Stealth Surface Modification of Surface-Enhanced Raman Scattering Substrates for Sensitive and Accurate Detection in Protein Solutions 50

4.1 Introduction 51

4.2 Experimental Section 55

4.3 Results and Discussion 60

4.4 Conclusions 68

4.5 Tables 69

4.6 Figures 70

Chapter 5 Hierarchical Zwitterionic Modification of a SERS Substrate Enables Real-Time Drug Monitoring in Blood Plasma 79

5.1 Introduction 79

5.2 Experimental Section 81

5.3 Results and Discussion 88

5.4 Conclusions 97

5.5 Tables 99

5.6 Figures 103

Chapter 6 Ultra-Low Fouling and High Antibody Loading Zwitterionic Hydrogel Coatings for Sensing and Detection in Complex Media 116

6.1 Introduction 116

6.2 Experimental Section 120

6.3 Results and Discussion 124

6.4 Conclusions 128

6.5 Tables 130

6.5 Schemes 131

6.6 Figures 133

Chapter 7 Rapid and Sensitive Detection of Anti-PEG in Blood Serum Based on SPR Sensor 138

7.1 Introduction 138

7.2 Experimental Section 141

7.3 Results and Discussion 144

7.4 Conclusions 147

7.5 Figures 148

Chapter 8 Conclusions 153

References 156

Curriculum Vitae 167

List of Tables

Table 2.1 Raman and SERS vibrational frequencies for 4-MPBA..... 22

Table 3.1 The assignment of SERS vibrational frequencies for 4-MBA 44

Table 4.1 SERS vibrational frequencies for 4-MPBA and CBT 69

Table 5.1 SERS vibrational frequencies for 100% human blood plasma..... 99

Table 5.2 SERS vibrational frequencies for pCBAA modification..... 100

Table 5.3 Film thickness of pure and mixed SAMs measured by ellipsometry and the molar ratio of mixed SAMs estimated from the film thicknesses. 101

Table 5.4 Elemental composition and surface ratio of mixed SAMs analyzed by XPS. 102

Table 6.1 The selection of hydrophilic SAM modification on the gold SPR chips..... 130

List of Schemes

Scheme 6.1 Overview of the coating process to generate CBHTFs on the surface of SPR chips 131

Scheme 6.2 Chemical synthesis of carboxybetaine diacrylamide (CBAAX)..... 132

List of Figures

Figure 1.1 Schematic illustrations of SERS and SPR 2

Figure 2.1 Scheme and characterizations of Q3D-PNA 23

Figure 2.2 SERS and Raman spectra of 4-MPBA and SERS spectrum of 4-MPBA-fructose 24

Figure 2.3 SERS spectra of benzenethiol with and without fructose 25

Figure 2.4 Control experiments with 3-MPBA 26

Figure 2.5 SERS spectra of the 8a and 8b modes of 4-MPBA SAMs upon the interaction with fructose 27

Figure 2.6 Quantitative detection of fructose 28

Figure 2.7 Interactions with other sugars 29

Figure 2.8 SERS spectrum of undiluted artificial urine 30

Figure 2.9 SERS spectra of 4-MPBA immersed in undiluted artificial urine, BSA solution, R6G solution, and PBS 31

Figure 2.10 Fructose detection curve in undiluted artificial urine 32

Figure 3.1 Schematic illustration of mapping pH_e of a single living cell cultured on a 4-MBA modified Q3D-PNA SERS substrate in the culture media. 45

Figure 3.2 SERS spectrum of 4-MBA and reproducibility test 46

Figure 3.3 SERS spectra of 4-MBA responding to pH changes 47

Figure 3.4 Influence of cations on pH detections 48

Figure 3.5 Optical images and pH_e SERS mapping of NIH/3T3 and HepG2 cells 49

Figure 4.1 Schematic illustration of mixed SAM of 4-MPBA and CBT on a gold Q3D-PNA SERS-active surface for fructose detection 70

Figure 4.2 Scheme of the reaction route for the synthesis of CBT 71
Figure 4.3 SERS spectra of pure 4-MPBA, 4-MPBA/CBT mixed SAMs and pure CBT on Q3D-PNAs in PBS 72
Figure 4.4 XPS studies 73
Figure 4.5 High-resolution XPS spectrum of the S 2p region of pure CBT SAM 74
Figure 4.6 SPR tests of the mixed SAMs 75
Figure 4.7 Fructose detection with the mixed SAM 76
Figure 4.8 PLS analysis 77
Figure 4.9 Detection in BSA solutions 78
Figure 5.1 Schematic of Q3D-PNAs SERS optofluidic system and hierarchical zwitterionic surface modifications 103
Figure 5.2 PCBAA surface modification enabling SERS detection in undiluted human blood plasma. 104
Figure 5.3 OEG SAM and C11 SAM modified SERS sensors challenged with undiluted human blood plasma 106
Figure 5.4 Real-time quantitative monitoring of doxorubicin in undiluted human plasma using the pCBAA-modified SERS optofluidic system 107
Figure 5.5 SERS spectra of DOX in plasma with different concentrations 109
Figure 5.6 Free DOX percentages in plasma measured by ultrafiltration and SERS methods 110
Figure 5.7 Optimizations of mixed SAM compositions 111
Figure 5.8 Hierarchical pCBAA surface modification to attract analytes and enable drug detection in undiluted human plasma 113

Figure 5.9 Limit of detection (LOD) experiments for CARB (a), PHEN (b) and AH (c), using the hierarchical pCBAA-modified SERS optofluidic system 114
Figure 5.10 Hierarchical pCBAA surface modification with probing molecules to enable pH and fructose detection in undiluted human plasma 115
Figure 6.1 Thickness control and stability test 133
Figure 6.2 Optimization of nonfouling performance 134
Figure 6.3 CBHTF coated on SiO_2 135
Figure 6.4 Typical SPR sensorgram for anti-TSH immobilization on CBTHF and followed with TSH antigen detection 136
Figure 6.5 Antibody loading, antigen response, and nonfouling properties of CBTHFs as the function of CBAAX crosslinker ratio 137
Figure 7.1 Anti-PEG detection by using the PEG coated SPR biosensor 148
Figure 7.2 Selection of surface chemistry 149
Figure 7.3 SPR detection of anti-PEG with different dilution factors 150
Figure 7.4 IgG/IgM differentiation 151
Figure 7.5 Quantification of anti-PEG 152

Acknowledgements

For all the works presented here, the author would like to thank his advisors, Professor Shaoyi Jiang and Professor Qiuming Yu for support, monetary, inspiration and funding for all presented works. The author would like to thank all the members of Jiang and Yu research groups for their kind help and discussion. The author would also like to express his special appreciation to his family, Zeran, Oliver, and Evelyn, and his parents, Wen and Shiqian for their unflagging support.

Chapter 1 Introduction

Blue sky, white clouds, red sunset and even the black letters printed here all depend on the interaction between light and molecules which can reveal fundamental information regarding these molecules. When the amount of molecules decreases, it becomes more challenging to observe their interactions with light. Fortunately, with the help of enhancing media such as metals, light-molecule interactions can be improved. For example, Raman spectroscopy and optical absorbance can be enhanced by the introduction of metal interfaces [1]. The enhancement is primarily from an electromagnetic contribution, which originates from the interaction of light with the free conduction electrons on a metal surface [2]. This creates surface plasmon polaritons (SPPs) which significantly increase the electromagnetic field. The study of light-metal interaction is known as plasmonics, which has attracted a lot of attention due to its potential applications in optical devices, catalysis, medicine as well as sensors [2-4]. Recently, the plasmonic sensors have been explored extensively due to their ultra-sensitivity and emerged as a new generation of analytical tools.

Among the plasmonic sensors, two of the most widely used and studied sensors are surface enhanced Raman scattering (SERS) sensors and surface plasmon resonance (SPR) sensors. SERS is a phenomenon which can significantly magnify the Raman signals of the molecules adsorbed on a nanostructured metal surface for up to millions of folds [5]. The enhancement is due to the extremely high local electromagnetic fields that arise from localized surface plasmon resonance (LSPR), and it has led to the detection of single molecules. Meanwhile, the resulting SERS spectrum consists of bands corresponding to vibrational or rotational transitions specific to the molecular structure,

and thereby providing chemical fingerprints to identify the analyte (**Figure 1a**). Based on the ultra-sensitivity and molecular specificity, SERS have already be used for a variety of applications ranging from chemical and biological sensing, environmental monitoring to diagnostics. SPR is based on the propagating SPPs excited on thin metal films using grating or prism couplers [6]. Changes in the refractive index above the metal induced by a binding event shifts the plasmon resonance condition, which can be detected as intensity, wavelength, or angle shifts in sensing applications (**Figure 1b**). The SPR

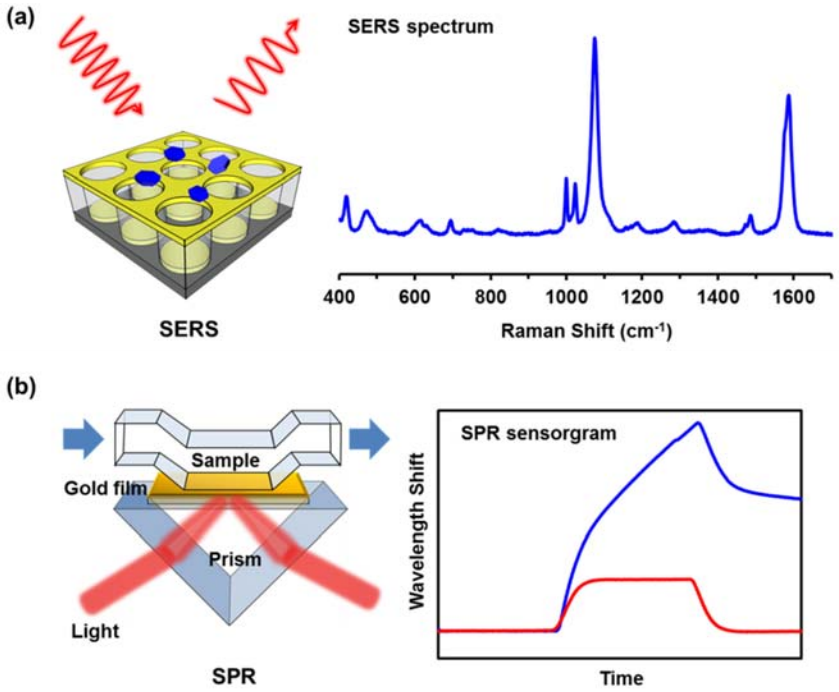

Figure 1.1 Schematic illustrations of SERS and SPR

(a) Schematic illustration of SERS substrate and typical SERS spectrum. (b) Schematic illustration of SPR biosensor and typical SPR sensorgram.

sensor can enable the direct observation of molecular interaction in real-time and offer the benefits of rapid, sensitive and label-free detection of chemical and biological species with potential applications in numerous important areas.

However, reliable biosensing in complex biological media based on these two advanced plasmonic sensors is still very challenging due to several reasons. For the SERS plasmonic sensor, one limitation is that SERS is a near-field effect [7]. The enhancement effect decreases exponentially with increasing distance from the surface. Meanwhile, a bare SERS-active surface lacks selectivity; anything adsorbed onto the surface can be detected. When the SERS sensor is exposed to complex media, there are huge amounts of interfering species in the media which can nonspecifically adsorb onto the SERS-active surface, thus generating background noise and masking the signals of the target analytes. In addition, the nonspecific adsorption of biomacromolecules such as proteins on the SERS active surface can also inhibit the adsorption of analytes onto the surface, thereby ruining the sensor. The situations worsen when the target analytes have relatively small or no Raman activities. A method which can amplify the detection signals over unwanted background is highly desirable and it is also essential to introduce nonfouling modifications to protect the SERS-active surface from nonspecific adsorption. Thus the tailoring of specific and multifunctional surface chemistry on the SERS sensor is necessary and it is one of the objectives of this dissertation.

In this dissertation, we discuss how to achieve the specific recognition and signal amplification of target analytes with small or no Raman activity using SERS. We propose a solution to immobilize a probe molecule on the SERS surface, which can specifically respond to the target molecule. In Chapter 2, we study the SERS detection of fructose,

which is a monosaccharide related with abnormal diabetes and obesity usually showing very weak Raman activity. To enable the detection, we select 4-mercaptophenylboronic acid (4-MPBA) as a probe molecule. The molecule of 4-MPBA possesses three key functions: molecule recognition and reversible binding of the analyte via the boronic acid group, amplification of SERS signals by the phenyl group, and immobilization on the surface of SERS-active substrates via the thiol group. The symmetry breaking of the 4-MPBA molecule upon fructose binding leads to the change of area ratio between totally symmetric 8a ring mode and nontotally symmetric 8b ring mode, which enables the detection. The limit of detection of 0.05 mM fructose in PBS and undiluted artificial urine is achieved. In Chapter 3, we investigate the usage of 4-mercaptobenzoic acid (4-MBA), which contains a carboxylic acid functional group on a thiophenol, for pH SERS sensing. We carefully study the influences of cations and the complexity of detecting solutions on the responses of 4-MBA SERS spectra to pH variations. Based on reliably generated calibration curves, we use the 4-MBA modified SERS substrates to image the extracellular pH (pH_e) distribution of live cells. From our results, localized pH_e is detected and mapped showing good spatial resolution and pH sensitivity showing pH_e domains in live cells. These two examples demonstrate the strategy for the design and selection of probe molecules on the SERS sensor to achieve the specific detection and signal amplification.

Despite successful detections using these probes, suppressions of sensitivity and accuracy in complex media are observed in comparison to the results obtained in simple buffered solutions. Due to the aforementioned reasons, nonspecific adsorption from the complex media can impede the analytes from attaching to the SERS-active surface. In

Chapter 4, we first introduce the zwitterionic nonfouling materials to the SERS surface. We design and synthesize a short zwitterionic thiol, N,N-dimethyl-cysteamine-carboxybetaine (CBT), and use it to modify SERS-active substrate surfaces. The carboxybetaine head group of CBT can bind water strongly and effectively resist protein adsorption. CBT also has a remarkably small Raman cross section. Thus when CBT is modified on the SERS-active surface, it does not generate any strong background signals. When CBT is mixed with probe molecules, due to the sharp difference between their intrinsic Raman activities, CBT can hide its own signal even though it dominates the surface demonstrating excellent nonfouling performance. The nonfouling property and invisibility in SERS spectra make CBT a stealth surface modification. However, CBT is a short thiol, which cannot withstand real-world complex media such as undiluted human blood plasma or serum. To further improve the nonfouling performance, in Chapter 5, we modify the SERS surface with zwitterionic polymer brush poly(carboxybetaine acrylamide) (pCBAA), a state-of-art nonfouling coating. The pCBAA is coated on the SERS-active surface via surface-initiated atom transfer radical polymerization (SI-ATRP), rendering the coating with high packing density showing undetected protein adsorption from the undiluted blood plasma. The probe molecules are also mixed inside the pCBAA coating to enable the specific detection. In addition, several drug molecules with strong Raman activity are directly detected by the pCBAA-coated SERS optofluidic system through the partitioning process demonstrating the potential of this technique to be used for real-time therapeutic drug monitoring.

Besides the SERS sensor, appropriate surface chemistry is also needed for the SPR plasmonic sensor. The specificity of the SPR sensor is totally dependent on the

biomolecular recognition species employed while the sensitivity will depend on the amount of nonspecific binding. In Chapter 6, we discuss a novel high antibody-loading, ultra-low fouling coating based on a thickness-controllable zwitterionic hydrogel thin film for SPR sensor. The coating is a hydrogel composed of CBAA monomer crosslinked with newly designed carboxybetaine diacrylamide crosslinker (CBAAX) showing exceptional good nonfouling property (< 5ng/cm^2 from undiluted blood plasma). The gel coating is a three-dimensional matrix, providing a large number of sites for ligand immobilization. The optimizations of nonfouling performance and antibody immobilization of the gel coating is studied by varying the crosslinking density. In Chapter 7, for the detection of anti-PEG antibodies in the blood, we also investigate the specific surface chemistry for the SPR sensor. With the selected surface modifications, the limit of detection of anti-PEG antibodies can be 10 ng/mL, which is even lower than the traditional ELISA test. This developed technology could be used for study the occurrence of pre-existing anti-PEG antibodies in the general population.

To introduce specific probe molecules on the SERS sensor or to increase the antibody loading on the SPR sensor, the purposes are the same aiming at enhancing detection specificity and signals. To introduce the zwitterionic nonfouling coatings to these sensors is to reduce the nonspecific adsorption from the background thus diminishing the noise. Combining these multifunctional modifications, we can increase the signal/noise ratio, thereby dramatically improving the sensitivity of the sensors.

Chapter 2 Sensitive and Fast Detection of Fructose in Complex Media via Symmetry Breaking and Signal Amplification Using SERS

A new strategy is proposed to sensitively and rapidly detect analytes with weak Raman signals in complex media using surface-enhanced Raman spectroscopy (SERS) via detecting the SERS signal changes of the immobilized probe molecules on SERS-active substrates upon binding of the analytes. In this work, 4-mercaptophenylboronic acid (4-MPBA) was selected as the probe molecule which was immobilized on the gold surface of a quasi-3D plasmonic nanostructure array (Q3D-PNA) SERS substrate to detect fructose. The molecule of 4-MPBA possesses three key functions: molecule recognition and reversible binding of the analyte via the boronic acid group, amplification of SERS signals by the phenyl group and thus shielding of the background noise of complex media, and immobilization on the surface of SERS-active substrates via the thiol group. Most importantly, the symmetry breaking of the 4-MPBA molecule upon fructose binding leads to the change of area ratio between totally symmetric 8a ring mode and nontotally symmetric 8b ring mode, which enables the detection. The detection curves were obtained in PBS and in undiluted artificial urine at clinically relevant concentrations and the limit of detection of 0.05 mM was achieved.

2.1 Introduction

In past decades, surface-enhanced Raman spectroscopy (SERS) has become a powerful analytical and sensing tool for applications in many areas ranging from biomedical diagnostics [8-11], environmental monitoring [12, 13], to chemical and biological sensing [7, 14-19], SERS offers the benefits of molecular specificity directly

related to the vibrational modes of analytes and ultra-sensitivity due to electromagnetic and chemical enhancement [20, 21]. However, there is a great challenge for SERS detection of small molecules in complex media due to the fact that: (1) SERS is a near-field effect. The extremely strong local electric fields, so-called hot spots, in the vicinity of the plasmonic nanostructures decay significantly beyond 2-3 nm from the metal surfaces [5, 22], Therefore, Raman signals can be greatly enhanced only when target analytes adsorb on the hot spots of SERS substrates. (2) Even for high surface-affinity analytes, the weak SERS signals of analytes with small intrinsic Raman scattering cross-section could be buried by background noise from nonspecific adsorption and interfering environment. The signals of interferences may cover or overlap with those of analytes, making the feature peaks of target analytes indiscernible.

Sugar detection using SERS in complex media encounters the same dilemma due to small Raman activity and low surface affinity of sugar molecules as well as high background noise from complex media. It was reported that saccharides such as glucose cannot be detected even in aqueous solution if a bare gold or silver SERS substrate was used [23, 24]. Van Duyne and co-workers developed a promising approach to address this problem by modifying the SERS substrate surfaces with a mixed self-assembled monolayer (SAM) to promote glucose partitioning to the surface [25]. Quantitative glucose detection was demonstrated by analysing glucose SERS signals from the subtracted SERS spectra of glucose solutions from the SAM background. This method was also applied for *in vivo* detection of glucose [26]. However, the SERS signals of glucose are weak due to its small Raman activity and a distance from the metal surface mediated by mixed SAM. Thus, the detection sensitivity is limited. To enhance detection

sensitivity, a strategy was developed by conjugating sugar molecules with those molecules having large Raman activity, or so-called SERS tags [27]. The SERS signals of the tags rather sugar molecules were detected. The complexity of the conjugation process and the specific design only for glycomic analysis make this method not a general approach. Therefore, to enable sensitive detection of small molecules in complex media using SERS, it is highly desirable to develop new detection platforms which not only promote the adsorptions of target analytes on the surface of SERS-active substrates but also amplify detection signals.

Fructose, a simple monosaccharide, is an important dietary source of carbohydrates, also involved in the pathogenesis of diabetic complications and may play a role in epidemic of obesity [28-30]. Sensitive and fast fructose detection especially in complex media can benefit the study and diagnostic of diabetic symptoms and be applied to food industry. Boronic acid has been known for reversibly binding to 1, 2- or 1, 3-diols [31] and has been used for the development of different kinds of sugar sensors [32-34]. Fructose not only has the highest binding constant to phenylboronic acid over other simple sugars but also can bind to boronic acid at neutral pH [35]. Fructose sensors base on gold electrodes, microcantilevers and photonic crystals utilizing the molecular recognition of boronic acid have been developed [36-38]. However, the high limit of detection and long detection time limit their clinical applications.

In this work, we report a method to sensitively and rapidly detect fructose in undiluted artificial urine by monitoring SERS spectral changes upon fructose binding to a pre-formed 4-mercaptophenylboronic acid (4-MPBA) SAM on a gold quasi-3D plasmonic nanostructure array (Q3D-PNA) SERS substrate. As shown in **Figure 2.1a**,

the probe molecule 4-MPBA contains three key functional groups: a boronic acid group that reversibly binds fructose; a benzene ring that amplifies the SERS signal upon fructose binding and thus shields the noise from complex media; and lastly a thiol group that immobilizes the probe molecule to the gold surface forming a well-packed SAM. We deliberately choose a structurally symmetric phenylboronic acid as the probe molecule because the binding of fructose breaks the nearly C_{2v} structural symmetry of 4-MPBA to C_s, leading to significant changes of the SERS peaks related to the totally symmetric (8a) and nontotally symmetric (8b) vibrational modes of the benzene ring due to the Herzberg-Teller contribution [39]. The extra chemical enhancement resulted from the charge transfer effect of thiol conjugated benzene of 4-MPBA provides strong and reproducible SERS signals, which can effectively shield the noises from complex media (e.g., undiluted artificial urine), proteins (e.g., bovine serum albumin (BSA)), and even strong Raman active dye molecules (e.g., Rhodamine 6G (R6G)). Selectivity was investigated by comparing the sensor's fructose response to the response invoked by glucose, mannose, or sucrose. Fructose detection was demonstrated in PBS buffer and undiluted artificial urine with a clinically relevant concentration range under physiological pH conditions.

2.2 Experimental Section

2.2.1 Materials

4-mercaptophenylboronic acid (> 90%), 3-mercaptophenylboronic acid (> 95%), benzenethiol (> 98%), 1-octanethiol (> 98.5%), D-(−)-fructose (> 99%), D-(+)-glucose (> 99.5%), D-(+)-mannose (> 99%), sucrose (> 99%), Rhodamine 6G (> 99%), phosphate buffered saline packet (PBS, pH 7.4 and ionic strength 150 mM) and albumin from

bovine serum were purchased from Sigma-Aldrich. High-purity deionized (DI) water was obtained with a Millipore water system. An artificial urine matrix was prepared according to the recipe provided in the previous studies [40] which was consisted of 55 mM sodium chloride, 67 mM potassium chloride, 2.6 mM calcium sulfate, 3.2 mM magnesium sulfate, 29.6 mM sodium sulfate, 19.8 mM sodium dihydrogen phosphate, 310 mM urea, and 9.8 mM creatinine.

2.2.2 Fabrication of gold Q3D-PNA SERS substrates

Gold Q3D-PNAs (50 μm × 50 μm) with a square grid of 400 nm diameter and 100 nm spacing were fabricated by electron beam lithography (EBL, JEOL JBX-6300FS). A layer of 300 nm-thick poly(methyl methacrylate) (PMMA) photoresist was spin-coated on a 4" silicon wafer and exposed to an electron beam. A total of 280 arrays were fabricated on the silicon wafer, arranged as 2 x 2 arrays per cm^2. Nanoholes were generated after development in 1:3 methyl isobutyl ketone/isopropanol (MIBK/IPA) PMMA developer for 70 s, followed by an IPA rinse and a post-bake at 95℃ for 30 min. Finally, the Au Q3D-PNAs were prepared by thermally evaporating a 50 nm Au (99.99%) film over the PMMA surface using thermal evaporator (Edwards, Auto 306). Scanning electron microscope (SEM, FEI Sirion) and tapping mode atomic force microscope (AFM, DI MultiMode with Nanoscope IVa controller) were used to characterize the dimensions of the nanostructures.

2.2.3 Surface modification of Q3D-PNA SERS substrates

4-MPBA, 3-MPBA, benzenethiol or 1-octanethiol SAMs were formed on the surface of a gold Q3D-PNA SERS substrate by soaking an UV ozone-cleaned substrate in a 0.1 mM 4-MPBA, 3-MPBA, benzenethiol or 1-octanethiol aqueous solution with 5 v.%

of ethanol for 12 h, followed by rinsing with deionized water and blowing dry in a stream of nitrogen.

2.2.4 Measurements of SERS and Raman spectra

Raman spectroscopy was carried out on a Renishaw InVia Raman spectroscope connected to a Leica DMLM upright microscope. A 50x (N.A. = 0.8) objective was used to focus a 785 nm laser on a Q3D-PNA or a neat sample and to collect the 180° scattered light from the sample surface. A surface modified SERS substrate was submersed in PBS solution in a custom-made container and a cover glass was carefully placed over the top to avoid air bubbles. SERS spectra were acquired in wet conditions. Spectral resolution of 1.1 cm^{-1} can be achieved and spectra ranging from 400 to 2600 cm^{-1} were collected. SERS spectra were taken continuously with laser power of 1 mW after the objective lens, CCD exposure time of 10 s, and single accumulation. Raman spectra were taken from the powder of neat materials with the laser power of 48 mW after the objective lens, CCD exposure time of 30 s, and single accumulation. All spectra were baseline corrected by fitting the raw spectrum to a fourth-order polynomial and then subtracted. The baseline corrected spectra were normalized with respect to the peak at 1075 cm^{-1} for 4-MPBA modified samples.

2.2.5 Detection of fructose in PBS and in undiluted artificial urine

The 4-MPBA SAM modified Q3D-PNA SERS substrate was placed in a custom-made container to take SERS spectra under wet conditions. A volume of 150 μL PBS solution or undiluted artificial urine spiked with concentrations of fructose from 0.02 to 10 mM was added on the SERS substrate surface carefully. Then the container was covered with a piece of microscope cover glass. The SERS spectra were collected at 0, 5,

10, 20, 30 and 40 min after adding each fructose solution. For the detection curve measurements in PBS and undiluted artificial urine, SERS spectra were collected after immersion in each concentration solution for 10 min. Three replicates were measured for each concentration or at each time and the error bar stands for the standard deviation.

2.3 Results and Discussion

2.3.1 Q3D-PNA SERS substrates

SERS substrates are critical to sensitive and reproducible detections. Here, we use gold Q3D-PNAs developed in our group as substrates. As shown in **Figure 2.1a**, the Q3D-PNA is composed of physically separated gold thin films with subwavelength nanoholes on the top and gold nanodiscs at the bottom of the wells. Unlike clusters of gold or silver nanoparticles, Q3D-PNAs are fabricated via electron beam lithography [41] or soft lithography [42] with excellent tunable plasmonic and optical properties as well as reproducible SERS signals for detection of a variety of analytes, from small molecules to large microorganisms [43].

The Q3D-PNA SERS substrate used in this work is a piece of ~1 cm x 1 cm silicon chip with 2 x 2 patterns of Q3D-PNA with 50 μm x 50 μm for each pattern and 200 μm apart between each pattern**.** The lateral and vertical dimensions of the Q3D-PNA are confirmed by SEM and AFM shown in **Figure 2.1b,c**, respectively. Strong SERS signals of 4-MPBA SAM in PBS buffer solution were obtained (**Figure 2.2**) and the spectra were highly reproducible taken at different positions on one pattern or on different patterns. The strong signals and the high reproducibility enable the sensitive and robust detections.

2.3.2 Fructose detection via symmetry breaking of 4-MPBA SAMs on Q3D-PNA SERS substrates

Prior to taking the SERS spectra of fructose binding to 4-MPBA SAMs on gold Q3D-PNA SERS substrates, the SERS spectrum of 4-MPBA SAM on a Q3D-PNA SERS substrate in PBS (pH 7.4) and the normal Raman spectrum of 4-MPBA neat powder were taken first, which are shown in **Figure 2.2**. The wavenumbers and the assignments of Raman and SERS vibrational modes of 4-MPBA are given in **Table 2.1**. The notable spectral changes of these two spectra are due to the formation of a well packed and orientated 4-MPBA SAM on the gold Q3D-PNA surface and the surface selection rules of SERS. The absence of the SH stretching mode at 2561 cm^{-1} and the in-plane bending mode of CSH at 907 cm^{-1} indicate that 4-MPBA adsorbs dissociatively as the thiolate and forms a gold-sulfur bond as illustrated in **Figure 2.2**. The in-plane benzene ring breathing mode (1) coupled with the CS stretching mode is shifted downward from 1092 to 1075 cm^{-1} and greatly enhanced, indicating a head-on close to the vertical orientation of 4-MPBA on the surface, which is similar to the benzenethiol SAM [44, 45]. The totally symmetric 8a mode is shifted downward from 1595 to 1587 cm^{-1} and slightly enhanced. A small shoulder appears at 1574 cm^{-1}, which is related to the nontotally symmetric 8b mode. The retained strong intensity of the 8a mode indicates that the nearly C_{2v} symmetry of 4-MPBA is not disrupted while forming a SAM on the SERS substrate. Due to the para-substitution by -SH and $-B(OH)_2$ as well as the formation of SAM via the S-Au bond, some peaks in the range of 1300-1050 cm^{-1} related to the in-plane movement of the ring carbons and substituents are enhanced. Also amplified are some peaks in the range of 850-620 cm^{-1} related to the CH wag vibration and ring out-of-plane vibrations [46].

The peaks at 1283, 1187, 694, 614, 473, and 420 cm^{-1} are attributed to these effects. Aforementioned ring modes demonstrate higher intensity while the peaks of BO stretching (1310, 1345 and 1370 cm^{-1}) are diminished. This indicates that the charge transfer of thiol-conjugated benzene contributes to extra enhancement [47].

It is well known that boronic acid binds with fructose at neutral pH and the binding changes the boronic acid from the uncharged trigonal form to the anionic tetrahedral form, resulting in the symmetry breaking from pseudo C_{2v} to C_s as shown in the illustration of **Figure 2.2** [35]. To evaluate the influence of fructose binding on the SERS spectrum, the PBS solution with 10 mM fructose was added on a 4-MPBA SAM modified Q3D-PNA substrate. The SERS spectrum was taken after 1 h immersion to ensure the binding reach equilibrium. The SERS spectra of 4-MPBA in PBS and in 10 mM fructose PBS solution are normalized to the peak at 1075 cm^{-1} since this peak is the strongest one and remains almost unchanged before and after fructose binding. An obvious relative intensity change of 8a (1587 cm^{-1}) and 8b (1574 cm^{-1}) modes was observed with a significantly decrease of the 8a mode and an increase of the 8b mode. The intensities of the 19a (1487 cm^{-1}) and 19b (1472 cm^{-1}) modes varied in a similar trend. These are mainly due to the change of the symmetry of a 4-MPBA molecule from nearly C_{2v} to C_s because of forming fructose-4-MPBA ester upon fructose binding [39, 48]. Other changes were also observed. The increase of the peaks at 420, 694, 1000, and 1024 cm^{-1} related to the 7a, 6a, 12 and 18a modes, respectively, suggests the possible reorientation [44] or charge redistribution of the benzene ring.

The critical roles played by the boronic acid functional group as well as the symmetry of the probe molecule in the detection of fructose were further verified by two

control experiments. In one control experiment, gold Q3D-PNA SERS substrates were modified with benzenethiol SAMs. As shown in **Figure 2.3**, there is no difference between the SERS spectra of benzenethiol SAM in PBS and in 10 mM fructose PBS solution, indicating that boronic acid functional group is essential for detecting fructose via forming the ester. In the second control experiment, the necessity of the C_{2v} symmetry of the probe molecule 4-MPBA was verified by forming C_s symmetric 3-MPBA SAMs on Q3D-PNA SERS substrates. As shown in **Figure 2.4**, the SERS spectrum of 3-MPBA SAM in PBS solution shows dramatically different 8a and 8b ring modes as those of 4-MPBA SAM in PBS. Because of the C_s symmetry of 3-MPBA SAM, the 8a and 8b ring modes split into two distinct peaks at 1555 and 1575 cm^{-1}, respectively, with the intensity of the 8b mode stronger than that of the 8a mode. The SERS spectrum taken on the 3-MPBA SAM modified Q3D-PNA substrate immersed in a10 mM fructose PBS solution for 1 h shows an almost identical spectrum as that in PBS. Unlike C_{2v} symmetric 4-MPBA, binding of fructose to 3-MPBA does not change the symmetry of 3-MPBA molecule, and thereby, makes no significant difference to the SERS spectrum.

2.3.3 Quantitative detection of fructose and the limit of detection in PBS

Since the symmetry breaking of 4-MPBA after fructose binding leads to a significant spectral change of the 8a and 8b ring modes, monitoring the variation of the area ratio of these two peaks upon fructose binding can provide a fast and quantitative detection of fructose. The SERS spectra of 4-MPBA upon fructose binding as a function of time were first acquired. **Figure 2.5a** shows the SERS spectra of the 8a and 8b peaks of 4-MPBA modified Q3D-PNA substrates in PBS and after immersing in10 mM fructose PBS solution for 5, 10, 20, 30 and 40 min, respectively. Clearly, the intensity of

the 8a mode at 1587 cm^{-1} decreases while the 8b mode at 1574 cm^{-1} increases over the time. To obtain the area ratio, two peaks were deconvoluted by assuming each peak has a Lorentzian shape and by fixing the peak position and the full widths at half maxima (FWHM). **Figure 2.5b** summarises the variation of the average area ratio of the 8a and 8b peaks for the concentration of fructose in the range of 0.05 to 10 mM as a function of time. Higher fructose concentrations result in more area ratio change and faster reaching of binding equilibriums. The variation of the area ratio caused by different fructose concentrations could even be detected less than 5 min. In this work, the detection curves were measured by taking the SERS spectra of each concentration at a fixed time, i.e., in 10 min immersion to ensure quick yet quantitative measurement. **Figure 2.6a** shows the SERS spectra of the 8a and 8b peaks of 4-MPBA modified Q3D-PNA substrates immersed in the fructose PBS solutions with the concentrations from 0.02 to 10 mM for 10 min. The decrease of the 8a mode and the increase of the 8b are clearly shown as the fructose concentration is increased. The detection curve of fructose in PBS is shown in **Figure 2.6b**, where the average area ratio of the peaks at 1574 to 1587 cm^{-1} taken after immersion for 10 min is plotted as a function of the fructose concentration. The inset of **Figure 2.6b** shows a linear relationship for the physiologically relevant concentrations ranging from 0.02 to 0.5 mM. Therefore, this method provides a fast and sensitive detection of fructose that could be of interest for the study and diagnostic of diabetic symptoms [48]. The limit of detection (LOD) was determined according to the definition of the concentration of fructose for which the average area ratio is equal to the sum of the average area ratio for 0 mM fructose plus 3 times its standard deviation. The LOD of 0.05 mM was obtained for fructose in PBS. Comparing to other biosensors which also utilized

the boronic acid–diol binding to detect fructose, our results showed about one order of magnitude lower LOD, indicating better sensitivity. For example, a microcantilever-based biosensor modified with 4-MPBA was used to detect fructose. A linear detection range of 2-25 mM and a LOD of 2 mM were reported [36]. An electrochemical-based biosensor using a 4-MPBA modified gold electrode showed a LOD of 3 mM in detection of fructose [38].

2.3.4 Selective detection of fructose over other simple sugars

The binding kinetics of simple sugars to phenylboronic acid has been investigated in solution phase [35]. The association constants (K_{eq}) of fructose, mannose, glucose, and sucrose to phenylboronic acid at pH 7.4 were determined to be 160, 13, 4.6, and 0.67 M^{-1}, respectively. The very high association constant of fructose to phenylboronic acid could be used for selective detection of fructose in the presence of other simple sugars. The selective detection of fructose over other simple sugars using 4-MPBA SAM modified SERS substrates was demonstrated by immersion of the substrates in PBS solutions with 10 mM fructose, mannose, glucose, and sucrose, respectively. The SERS spectra were collected after 1h immersion in sugar solutions to allow slower binding occur. The average area ratio of the peaks at1574 to 1587 cm^{-1} was calculated and the difference of the average area ratios between each sugar solution and PBS were plotted in **Figure 2.7**. In consistent with the association constant of each sugar to phenylboronic acid in solution, the binding of sugar to 4-MPBA SAM follows the same trend as shown in **Figure 2.7**. While a very small change was observed for 10 mM mannose PBS solution, there were no detectable changes for both 10 mM glucose and sucrose PBS solutions. Therefore, the

selective detection of fructose in the presence of other simple sugars can be achieved by conducting the experiment in neutral pH solutions.

2.3.5 Effective shielding of background noises in complex media

The fructose level in serum and daily urinary excretion has been used as a biomarker for monitoring sugar consumption and potential diabetic complications. Therefore, we evaluated the sensing capability of our platform in the detection of fructose in complex media. The undiluted artificial urine was selected. In a control experiment, we immersed a bare Q3D-PNA SERS substrate in undiluted artificial urine. **Figure 2.8** shows the SERS spectrum of undiluted artificial urine, which is similar to the spectrum reported before [49, 50], indicating nonspecific adsorptions of urea and creatinine in the artificial urine to the gold surface. However, when a 4-MPBA modified Q3D-PNA SERS substrate was used, the SERS spectrum exhibits no changes compared to that taken in PBS (**Figure 2.9**). We also immersed a 4-MPBA modified Q3D-PNA SERS substrate in 1 mg/ml BSA solution and acquired the SERS spectrum. As shown in **Figure 2.9**, the SERS spectrum of 4-MPBA SAM is completely unaffected even though a strong BSA adsorption (148 ± 16 ng/cm^2) to the 4-MPBA SAM surface was detected by an SPR biosensor. All these experiments demonstrated that despite strong nonspecific adsorptions on the surfaces of 4-MPBA modified Q3D-PNA SERS substrates, the strong SERS signals of 4-MPBA SAMs are not influenced and can effectively shield the background noise. This is mainly because the Raman scattering cross-section of benzene ring is much larger than that of the urine media and the protein. Meanwhile, the benzene ring is in the close proximity to the SERS-active surface because of forming a SAM. An extra chemical enhancement could be induced by the excitation of a resonance arising from the

charge-transfer between the metal surface and the adsorbate. It has been reported that thiolated linkers with conjugated π-electrons allow more efficient electron transfer and molecular orbital overlapping between metal surface than saturated alkanethiols [51].

To further evaluate the effectiveness of the 4-MPBA modified Q3D-PNA SERS substrates in shielding the background noises, a solution containing R6G, a dye molecule with a large Raman scattering cross-section, was used to serve as a test medium. 10^{-5} M R6G solution is supposed to show very strong SERS signals on a bare gold SERS substrate [52]. However, the SERS spectrum taken from the 4-MPBA SAM modified Q3D-PNA substrate immersed in the same concentration of R6G solution (**Figure 2.9**) shows very weak R6G peaks, of which the wavenumbers are labeled. All the peaks related to 4-MPBA SAM are not influenced. Therefore, the extremely strong SERS signals of the 4-MPBA SAM can effectively shield the background noises which make 4-MPBA an excellent probe molecule for detecting fructose in complex media using SERS.

2.3.6 Fructose detection in undiluted artificial urine

The detection curve of fructose in undiluted artificial urine was measured by taking the spectra of 4-MPBA SAM modified SERS substrates submersed in the urine spiked with different concentrations of fructose (0.02-0.5 mM) after 10 min. The average area ratio of the peaks at 1574 to 1587 cm^{-1} as a function of the fructose concentration is shown in **Figure 2.10**. The smaller area ratio in urine at each concentration compared to the corresponding ratio in PBS could be due to the partially blocked boronic acid functional groups by nonspecific adsorptions. Nonetheless, the same limit of detection of 0.05 mM in undiluted artificial urine was achieved as that in PBS. Since the detection of fructose is enabled by monitoring the SERS signal change of the probe molecule upon

binding of the analyte rather than the direct detection of the SERS signal of the analyte itself, this method not only ensures the detection specificity, considering the SERS signal of the probe molecule only change upon the binding of the target analyte in the complex media, but also greatly improves the detection sensitivity, benefiting from the signal amplification of the probe molecule. This method takes the advantage of greater chemical enhancement of the probe molecule than the fouling molecules and thereby, the background noise of complex media can be effectively shielded.

2.4 Conclusions

In summary, we described a method for sensitive and fast fructose detection in undiluted artificial urine by monitoring SERS spectral changes of 4-MPBA probe molecules upon fructose binding which breaks the structural symmetry of the probe molecules. The greater chemical enhancement of the probe molecules not only improves the detection sensitivity but also amplifies the SERS signal that effectively shields the background noise in complex media. The limit of detection of 0.05 mM fructose in PBS and undiluted artificial urine was achieved and a linear response was shown in the range of clinically relevant concentrations. The idea of using a probe molecule with the functions to recognize analytes and to amplify signals can be adopted as a general strategy for detection of analytes with weak Raman scattering in complex media using SERS.

2.5 Tables

Table 2.1 Raman and SERS vibrational frequencies for 4-MPBA

Raman Neat Powder (cm^{-1})	SERS SAM (cm^{-1})	Assignments[a]
	420	7a; $\beta_{CCC} + \nu_{CS}$
	473	16b; $\gamma_{CCC} + \beta_{OBO}$
	614	6b; $\beta_{CCC} + \beta_{OBO}$
631		ν_{CS}
	694	6a; $\beta_{CCC} + \nu_{CS}$
722	728	4b; γ_{CCC}
757	754	11; γ_{CH}
803		10a; γ_{CH}
907		β_{CSH}
1006	1000	12; β_{CCC}
1027	1024	18a; β_{CH}
1092	1075	1; $\beta_{CCC} + \nu_{CS}$
1107	1106	15; β_{CH}
1187	1187	9a; $\beta_{CH} + \beta_{BOH}$
	1283	3; $\beta_{CH} + \beta_{BOH}$
1310,1345,1370		ν_{BO}
	1472[b]	19b; ν_{CC}
	1487	19a; ν_{CC}
	1574[b]	8b; ν_{CC}
1595	1587	8a; ν_{CC}
2561		ν_{SH}

[a] ν; stretching, β; in plane bending, γ; out of plane bending

[b] 8b and 19b nontotally symmetric ring-stretching vibrational modes increase while 8a and 19a totally symmetric ring-stretching vibrational modes decrease in SERS spectra of 4-MPBA after fructose binding due to Herzberg-Teller contributions.

2.6 Figures

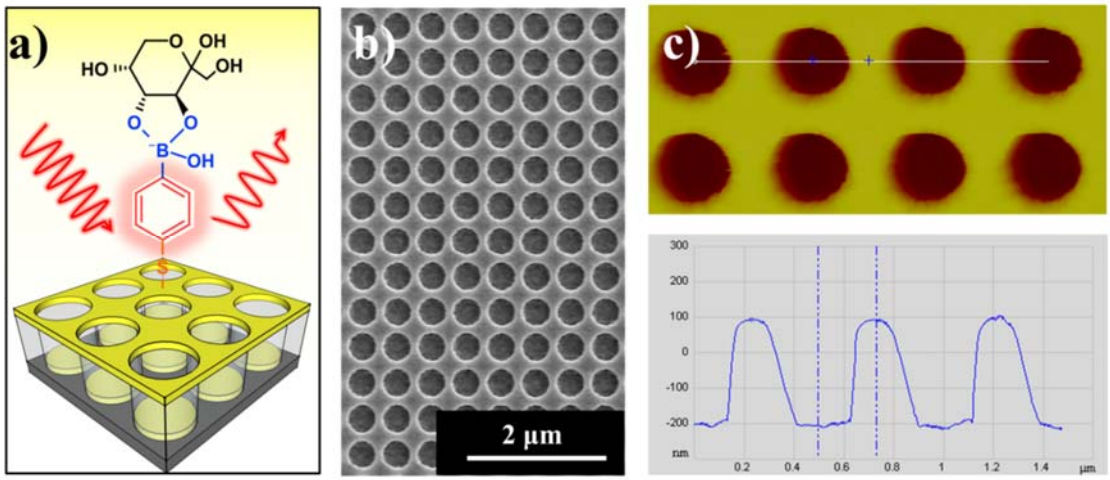

Figure 2.1 Scheme and characterizations of Q3D-PNA

(a) Schematic illustration of 4-MPBA on a gold Q3D-PNA for sensitive and fast detection of fructose using SERS. (b) The top-view SEM image of a Q3D-PNA showing the diameter of ~400 nm. (c) The 2 µm × 1 µm AFM image of a Q3D-PNA and a line profile showing the depth of ~300 nm.

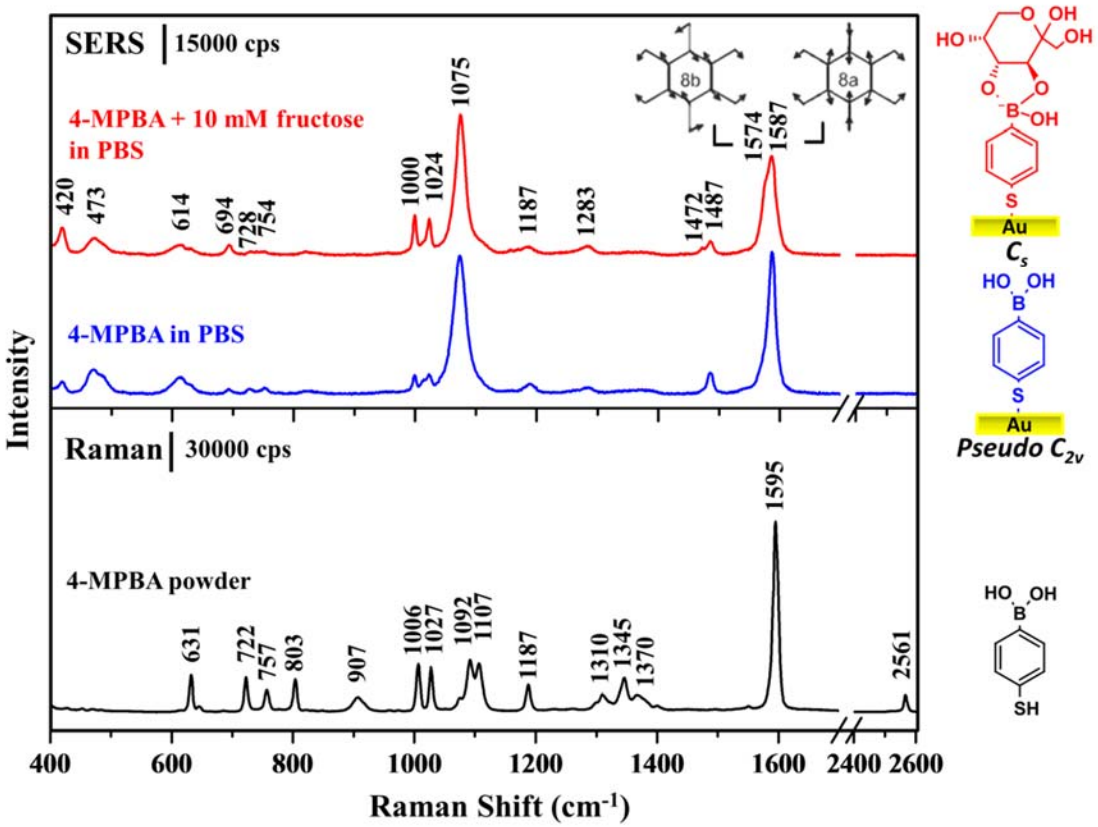

Figure 2.2 SERS and Raman spectra of 4-MPBA and SERS spectrum of 4-MPBA-fructose

(Black) Normal Raman spectrum of 4-MPBA neat powders along with the molecular structure of 4-MPBA. The λ_{ex} = 785 nm, P_{laser} = 48 mW, and t = 30 s. (Blue) SERS spectrum of 4-MPBA SAM on a Q3D-PNA in PBS along with the illustration of 4-MPBA SAM on Au with the pseudo C_{2v} molecular structure. (Red) SERS spectrum of fructose binding to 4-MPBA SAM on a Q3D-PNA in PBS with 10 mM fructose taken after 1 h immersion. The illustration shows the symmetry breaking of 4-MPBA from pseudo C_{2v} to C_s upon fructose binding. The λ_{ex} = 785 nm, P_{laser} = 1 mW, and t = 10 s. Two SERS spectra were normalized to the peak at 1075 cm^{-1}.

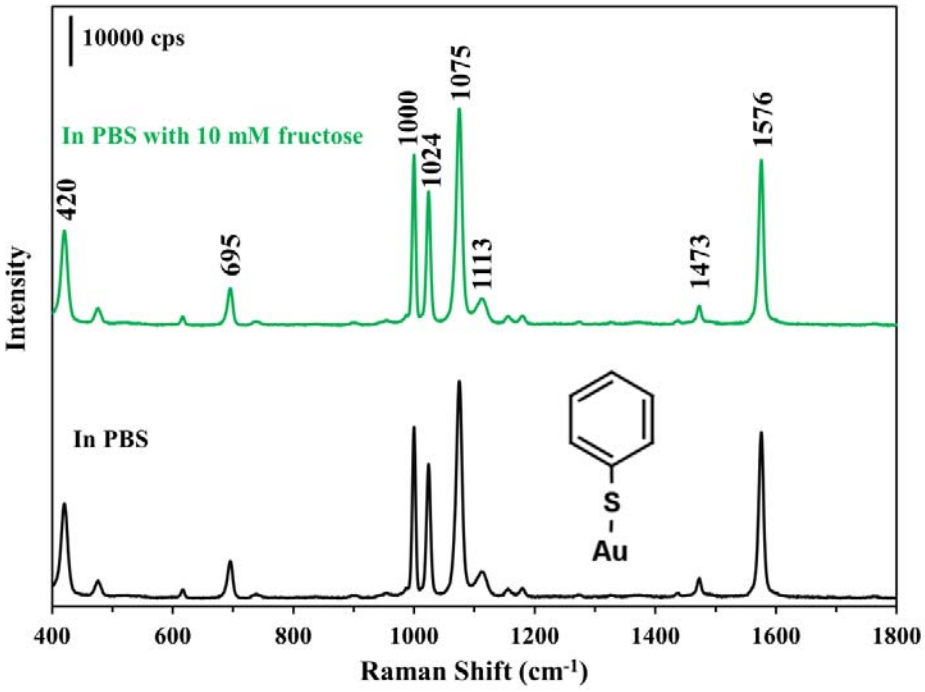

Figure 2.3 SERS spectra of benzenethiol with and without fructose

SERS spectra of benzenethiol SAMs on Q3D-PNA SERS substrates in PBS (black) and in PBS with 10 mM fructose after immersion for 1 h (green). There is no difference between two spectra, indicating that the boronic acid functional group is necessary for specific binding of fructose. Two SERS spectra were normalized to the peak at 1075 cm^{-1}. The λ_{ex} = 785 nm, P_{laser} = 1 mW, and t = 10 s.

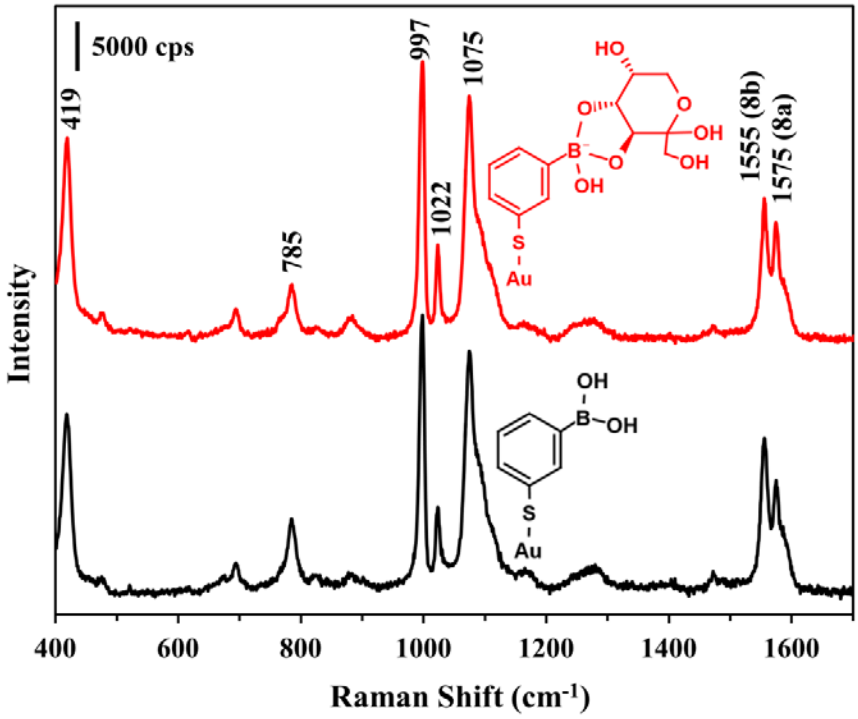

Figure 2.4 Control experiments with 3-MPBA

SERS spectra of 3-MPBA SAMs on Q3D-PNA SERS substrates in PBS (black) and in 10 mM fructose PBS solution after immersion for 1 h (red). There is no significant difference between two spectra, indicating that the C_{2v} symmetry of the probe molecule is necessary for detecting fructose via symmetry breaking of the probe molecule upon fructose binding. Two SERS spectra were normalized to the peak at 997 cm^{-1}. The λ_{ex} = 785 nm, P_{laser} = 1 mW, and t = 10 s.

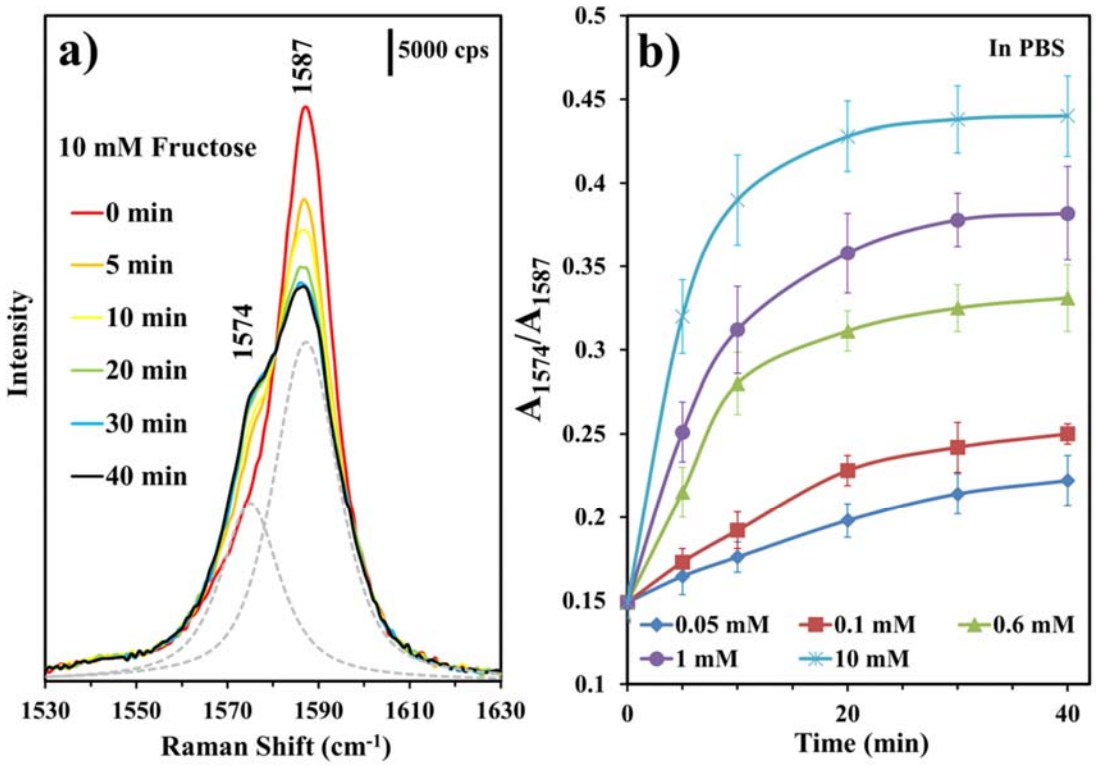

Figure 2.5 SERS spectra of the 8a and 8b modes of 4-MPBA SAMs upon the interaction with fructose

(a) The SERS spectra of the 8a and 8b modes of 4-MPBA SAMs upon the interaction with 10 mM fructose in PBS at different immersion times. The λ_{ex} = 785 nm, P_{laser} = 1 mW, and t = 10 s. The spectra were normalized to the peak at 1075 cm^{-1}. (b) The viariation of the average area ratio of the peaks at 1574 to 1587 cm^{-1} for each concentration of fructose in PBS as a function of time.

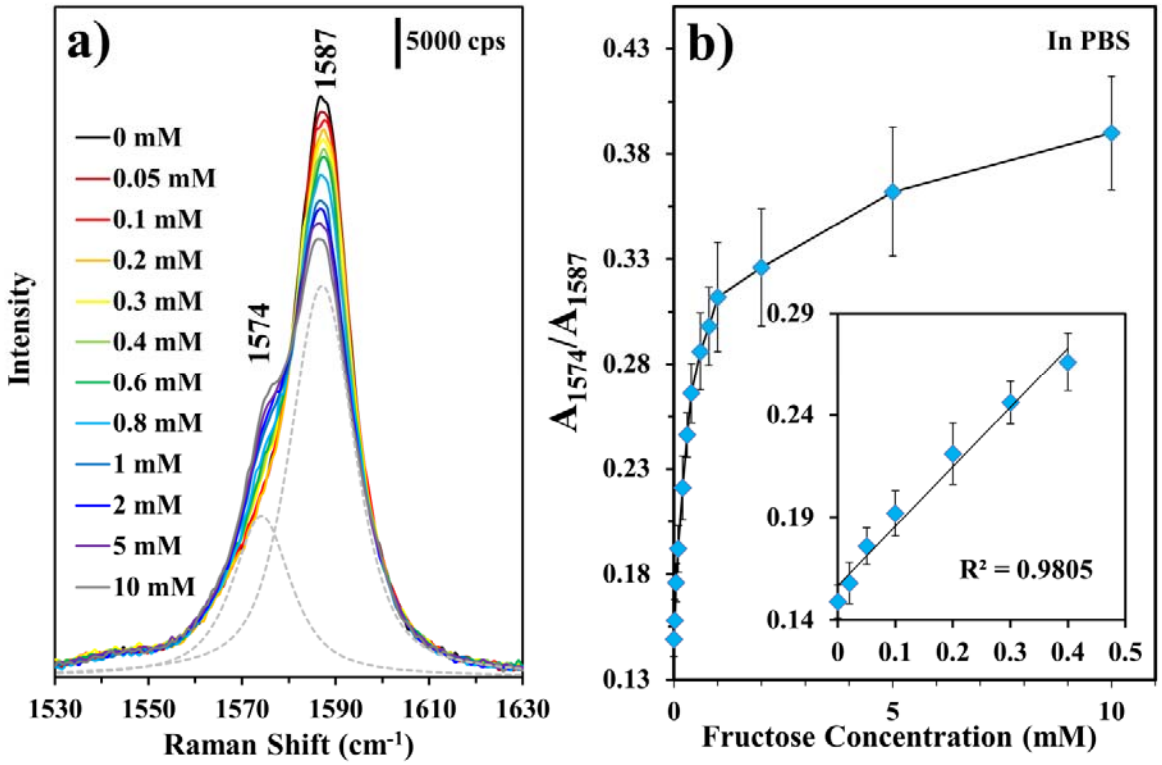

Figure 2.6 Quantitative detection of fructose

(a) The SERS spectra of the 8a and 8b modes of 4-MPBA SAMs in fructose PBS solutions with the concentrations of 0.02 – 10 mM after immersion for 10 min. The λ_{ex} = 785 nm, P_{laser} = 1 mW, and t = 10 s. The spectra were normalized to the peak at 1075 cm^{-1}. (b) The fructose detection curve in PBS by plotting the average area ratio of the peaks at 1574 to 1587 cm^{-1} as a function of the fructose concentration after immersion for 10 min. Inset: a linear relationship for the physiologically relevant concentrations.

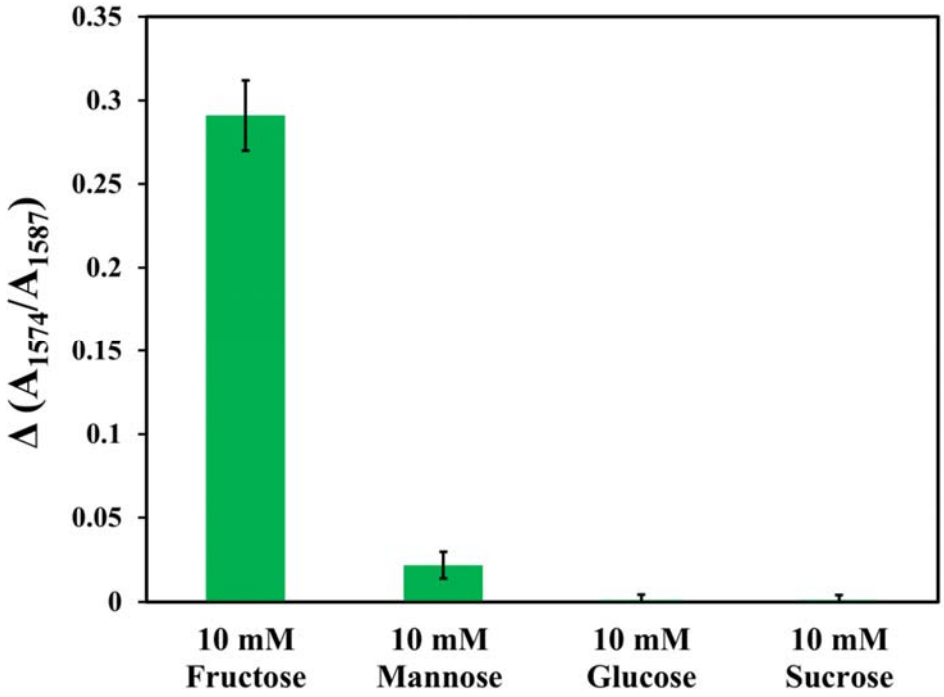

Figure 2.7 Interactions with other sugars

The difference of the average area ratios of the peaks at 1574 to 1587 cm^{-1} between immersed in each10 mM sugar solution and PBS for 1 h. The sugar solutions are 10 mM fructose, mannose, glucose, and sucrose in PBS, respectively. Δ (A_{1574}/A_{1587}) = A_{1574}/A_{1587} (sugar) - A_{1574}/A_{1587} (PBS)

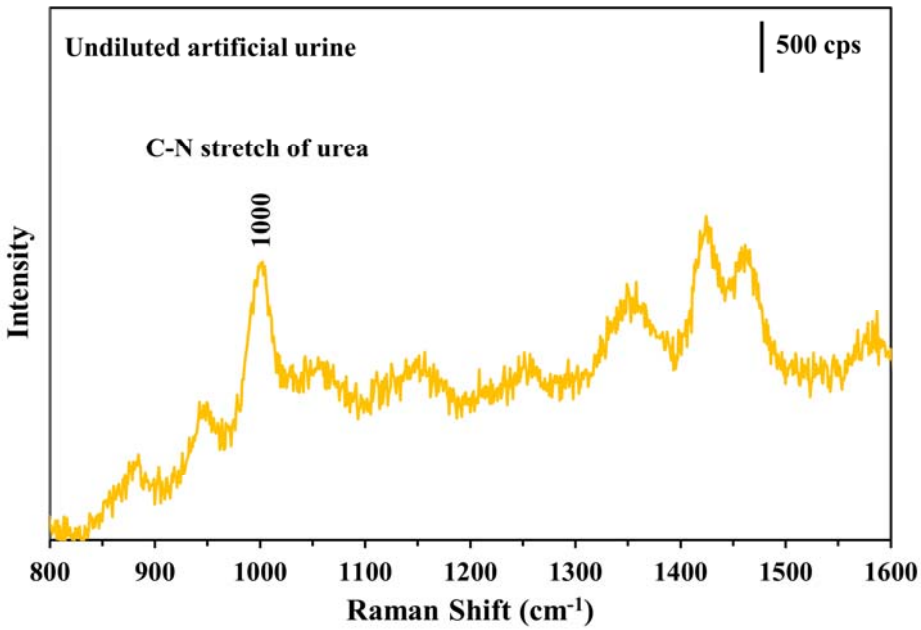

Figure 2.8 SERS spectrum of undiluted artificial urine

SERS spectrum of undiluted artificial urine on a bare gold Q3D-PNA SERS substrate. The labeled peak at 1000 cm^{-1} corresponds to the symmetrical C-N stretch of urea. The λ_{ex} = 785 nm, P_{laser} = 1 mW, and t = 30 s.

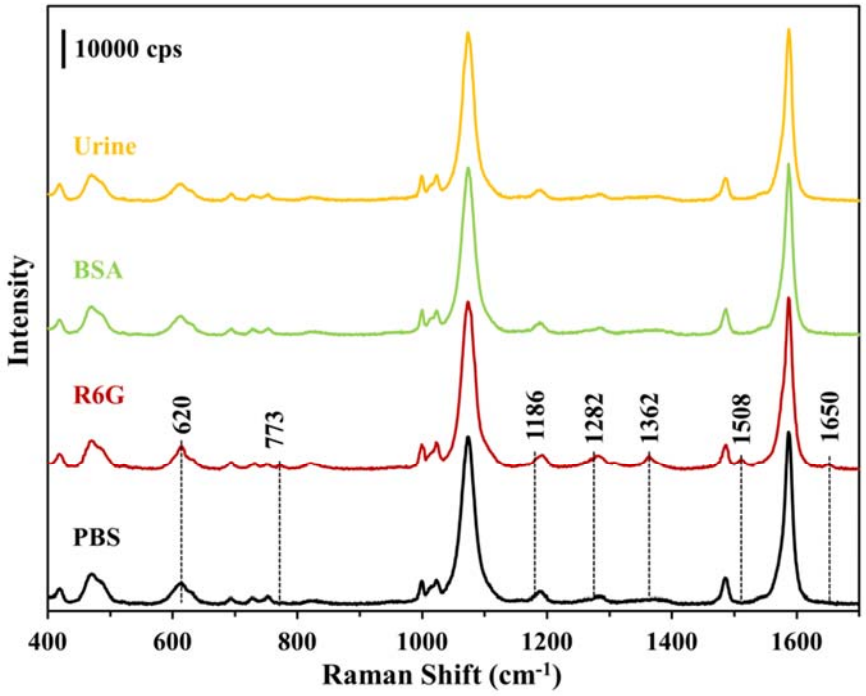

Figure 2.9 SERS spectra of 4-MPBA immersed in undiluted artificial urine, BSA solution, R6G solution, and PBS

The SERS spectra of 4-MPBA SAM modified Q3D-PNA SERS substrates immersed in undiluted artificial urine, 1 mg/ml BSA solution, 10^{-5} M R6G solution, and PBS. The labeled peaks belong to R6G. The λ_{ex} = 785 nm, P_{laser} = 1 mW, and t = 10 s. The spectra were normalized to the peak at 1075 cm^{-1}.

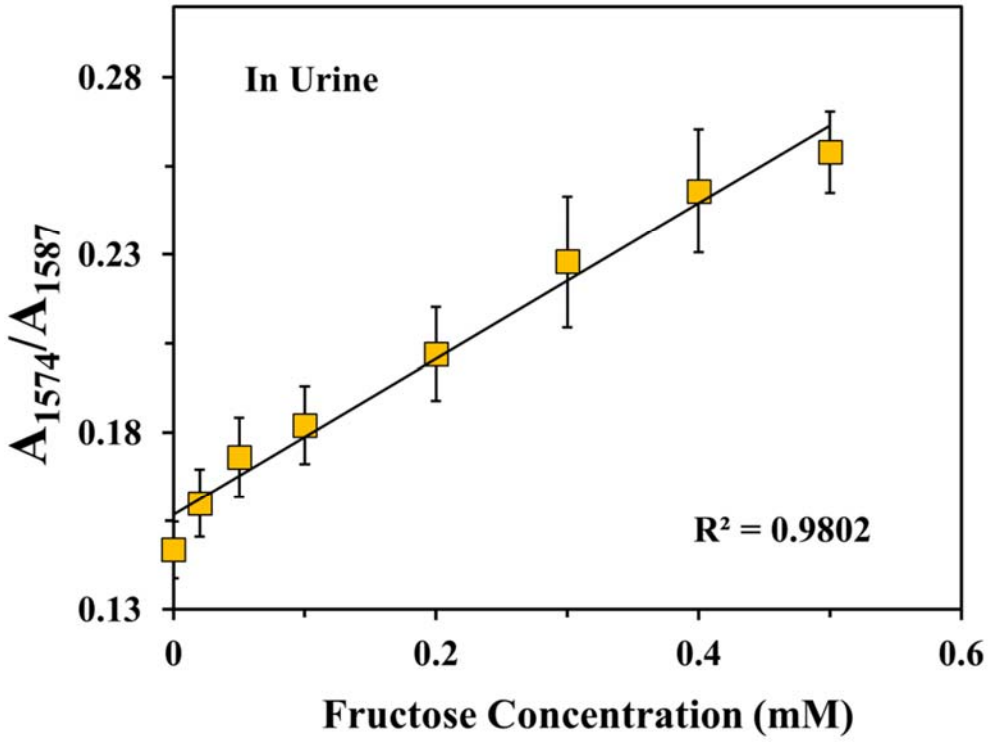

Figure 2.10 Fructose detection curve in undiluted artificial urine

The fructose detection curve in undiluted artificial urine by plotting the average area ratio of the peaks at 1574 to 1587 cm^{-1} as a function of the fructose concentration after immersion in each concentration solution for10 min.

Chapter 3 Functionalized Plasmonic Nanostructure Arrays for Direct and Accurate Mapping Extracellular pH of Living Cells in Complex Media Using SERS

The extracellular pH (pH_e) of living cells is one of the major factors that influence cell behaviors including cycle progression, migration, and proliferation, as well as metastasis and invasion of tumor cells. Thus, accurate sensing and mapping of the pH_e is still a critical yet challenging task in the study of pH_e-dependent cell behaviors. In this work, we present a method to map pH_e of living cells based on surface-enhanced Raman spectroscopy (SERS). We immobilized a pH probe molecule, 4-mercaptobenzoic acid (4-MBA), on a gold quasi three-dimensional plasmonic nanostructure array (Q3D-PNA) to enable an exceptionally sensitive and reproducible pH measurement. We prudentially investigated the influences of cations and complexity of detecting solutions on the responses of 4-MBA SERS spectra to pH variations to ensure the accuracy. Herein, a normal cell line (NIH/3T3) and a tumor cell line (HepG2) were cultured on the 4-MBA modified SERS substrates. Localized pH_e was detected and mapped with good spatial resolution and pH sensitivity showing pH_e domains on both cells. Moreover, the averaged pH_e of tumor cells was shown to be more acidic compared with that of normal cells.

3.1 Introduction

The extracellular pH (pH_e) plays a critical role in the function and metabolism of cells. The molecular processes involved in cell cycle progression, proliferation, and differentiation are all influenced by the extracellular acidity [53]. In addition, the pH_e of tumor cells is suggested to be more acidic than the normal cells. Tumor cells can secrete

protons (H^+) through ion exchangers on the plasma membrane acidifying their extracellular environment, which is related with the tumor cells' adhesion, malignant transformation, and metastasis [54]. Meanwhile, the pH gradient across the membrane affects the response of tumors to various treatments such as chemotherapy, radiotherapy and hyperthermia. The effects of pH_e on immune functions have also been reported [55]. Thus, an accurate method to measure the extracellular pH is highly desirable. More challenges are posted in mapping the pH_e distributions of single living cells with good spatial resolution and pH sensitivity.

Glass or fiber optic pH microelectrodes were used to determine the pH_e of animal and human tumors [56]. However, these invasive techniques are not suitable for the mapping of pH_e on a single living cell because the diameters of the electrodes are larger than those of cells. Tumor pH_e can be mapped noninvasively by magnetic resonance spectroscopic imaging [57, 58]. However, the mapping is usually conducted on a larger region of tumor tissue, and the spatial resolution is too low to be applied for the study of single living cells. Fluorescence-based pH probes provide excellent spatial resolution, but most have been designed to detect the intracellular pH [59]. Recently, several fluorescent pH_e indicators were developed based on the linked membrane protein or lipid-DNA for cell-surface anchoring [60]. However, whether the probe can be anchored uniformly on the membrane without forming domains is questionable and the process is complex. Furthermore, the fluorophores are prone to bleaching under repeated and intense illuminations.

Raman microspectroscopy is a rapid, noninvasive, and label-free technique that can be used to analyze and image cells with local molecular specificity. Surface-

enhanced Raman spectroscopy (SERS) can magnify the Raman signals of molecules or species in the proximity of the surfaces of plasmonic nanostructures a million fold, rendering ultra-sensitivity [61]. The pH sensing based on SERS has been explored before [62-66]. Several groups have demonstrated that the pH of solutions and living cells can be detected by using gold or silver nanoparticles functionalized with 4-mercaptobenzoic acid (4-MBA), a probe molecule with a pH dependent SERS spectrum. Since the functionalized nanoparticles were taken up by the cells, intracellular pH (pH_i) rather than pH_e were measured. In addition, due to the clustering of nanoparticles and uncontrolled uptake process, it is difficult to obtain reproducible and accurate pH measurement and mapping. In contrast, using a two-dimensional SERS-active surface instead of nanoparticles can prevent cell uptake, enabling the measurement and mapping of pH_e of cells.

Herein, we immobilized 4-MBA on a gold quasi three-dimensional plasmonic nanostructure array (Q3D-PNA) to map the local pH_e of single living cells using SERS (**Figure 3.1**). The 4-MBA functionalized Q3D-PNA SERS substrates demonstrated good sensitivity and reproducibility across the entire nanopatterned area for the pH measurement, which are essential for SERS pH_e mapping of single living cells. The influence of cations in detecting solutions on the responses of 4-MBA SERS spectra to pH variations were investigated and the calibration curves were established to ensure the detection and mapping accuracy in complex media such as cell culture media. As a proof of concept, a normal cell line (NIH/3T3) and a tumor cell line (HepG2) were cultured on the 4-MBA modified Q3D-PNA SERS substrates. The values of local pH_e of living cells

were detected and mapped with high spatial resolution and pH sensitivity. The tumor cells displayed more acidic averaged pH_e.

3.2 Experimental Section

3.2.1 Materials

4-Mercaptobenzoic acid (4-MBA, 99%), phosphate buffered saline packet (PBS, pH 7.4 and ionic strength 150 mM), sodium chloride (NaCl, 99%), potassium chloride (KCl, 99%), potassium phosphate dibasic (K_2HPO_4, 98%), HEPES ($C_8H_{18}N_2O_4S$, 99.5%), calcium chloride ($CaCl_2$, 97%), magnesium chloride ($MgCl_2$, 98%), sodium phosphate dibasic (Na_2HPO_4, 99%), and citric acid ($C_6H_8O_7$, 99%) were purchased from Sigma-Aldrich (St. Louis, MO). High-purity deionized (DI) water was obtained with a Millipore water system. Gibco® Dulbecco's modified eagle medium (DMEM, high glucose, GlutaMAX™ Supplement) and fetal bovine serum (FBS) were purchased from Life Technologies (Grand Island, NY).

3.2.2 Fabrication and surface modification of gold Q3D-PNA SERS substrates

Gold Q3D-PNAs (50 μm × 50 μm) with a square grid of 400 nm diameter and 100 nm spacing were fabricated by electron beam lithography (EBL) following the same method reported previously [67, 68]. Scanning electron microscope (SEM, FEI Sirion) and tapping mode atomic force microscope (AFM, DI MultiMode with Nanoscope Iva controller) were used to characterize the dimensions of the nanostructures. The 4-MBA self-assemble monolyaer (SAM) was formed on the surface of the Q3D-PNA SERS substrate by soaking an UV ozone-cleaned substrate in a 0.1 mM 4-MBA in ethanol for 12 h, followed by rinsing with ethanol, deionized (DI) water and blowing dry in a stream of nitrogen.

3.2.3 Generation of pH calibration curves

The pH calibration curves were generated from different solutions including, intracellular mimic (IC: 5 mM NaCl; 120 mM KCl; 10 mM K_2HPO_4; 25 mM HEPES; 0.15 mM $CaCl_2$; 5 mM $MgCl_2$; pH adjusted with KOH and HCl), cell culture medium (CM: DMEM with additional 25 mM HEPES and 10% fetal bovine serum; pH adjusted with NaOH and HCl), PBS (10 mM Na_2HPO_4; 1.8 mM KH_2PO_4; 138 mM NaCl; 2.7 mM KCl; pH adjusted with NaOH and HCl), DI water (pH adjusted with NaOH and HCl) and phosphate citrate buffer (PC: mixing aqueous solutions of Na_2HPO_4 (200 mM) and citric acid (100 mM) with different volume ratios for desired pH).

Raman spectroscopy was carried out on a Renishaw InVia Raman spectroscope connected to a Leica DMLM upright microscope. A 50×/N.A. = 0.8 objective was used to focus a 785 nm laser on a Q3D-PNA, and to collect the 180° scattered light from the sample surface. The 4-MBA modified SERS substrates were submersed in different solutions in a custom-made container and covered with a glass slide on the top to take SERS spectra in a wet condition. The laser power was set at 1 mW and the exposure time was 10 s. Spectral resolution of 1.1 cm^{-1} can be achieved and spectra ranging from 400 to 1800 cm^{-1} were collected. The pH calibration curves were generated by plotting the relative intensities of the νCOO^- mode to the benzene ring *v8a* mode as a function of pH.

3.2.4 Cell seeding on the Q3D-PNA SERS substrates

Prior to cell culture, the 4-MBA modified Q3D-PNA SERS substrates were sterilized by soaking and rinsing with copious amounts of ethanol. Two sterilized SERS substrates each with 4 of 50 μm × 50 μm Q3D-PNA patterns were attached to custom-made Teflon holders and then they were placed in two petri dishes. To them, NIH/3T3

and HepG2 cells (ATCC, Manassas, VA) were plated separately in each at about 4×10^4 cells/mL in DMEM with additional 25 mM HEPES and 10% FBS in a 5% CO_2 incubator at 37 °C for 24 h.

3.2.5 Optical imaging and SERS mapping of pH_e of living cells

The optical images of NIH/3T3 and HepG2 after 24 h incubation on the 4-MBA modified Q3D-PNA SERS substrates were taken using 10×/N.A. = 0.3 and 50×/N.A. = 0.8 lenses. The Teflon holders with SERS substrates and cultured cells were taken out of the petri dishes after 24 h incubation. A cover glass was carefully put over the top opening of the Teflon holder. The optical and Raman images were taken directly from these samples by impinging the light or laser through the cover glass and focsing on the sample surface.

The bright field and dark field images of cells on the Q3D-PNA patterns were taken with the 50×/N.A. = 0.8 lens. The SERS spectra of NIH/3T3 and HepG2 cells were taken using the Renishaw InVia confocal Raman microspectrocope in the mapping mode with 1 mW laser power, 10 s exposure time and spectral range from 1300 to 1800 cm^{-1} using a 50×/N.A. = 0.8 objective with a pinhole to focus the beam to a ~2 μm diameter spot. The mapping area was a square of 50 μm × 50 μm covering the Q3D-PNA pattern and the step size was 2 μm in both x- and y-direction.

3.3 Results and Discussion

3.3.1 High reproducibility of Q3D-PNA SERS substrates

The SERS substrate for mapping pH_e of single live cells is critical because it has to be stable, sensitive, spatially uniform and reproducible. In this work, we used the gold Q3D-PNA SERS substrate, which is composed of physically separated subwavelength

gold nanodiscs at the bottom and a gold thin film with nanoholes on the top (**Figure 3.1**). Q3D-PNAs were designed using finite-difference time-domain (FDTD) electromagnetic simulations and fabricated via EBL, which have demonstrated excellent tunable plasmonic and optical properties as well as strong and reproducible SERS signals [67, 69]. **Figure 3.2a** shows the SERS spectrum of 4-MBA SAM formed on the Q3D-PNA in PBS at pH 7.4. The peak assignments are summarized in **Table 3.1**. **Figure 3.2b** shows the contour of 32 SERS spectra of 4-MBA collected from the same chip at 32 different locations. The high reproducibility indicates an exceptional uniformity of the substrate, which is crucial for SERS mapping in order to yield a complete and meaningful spectral map.

3.3.2 pH response of 4-MBA modified Q3D-PNA SERS substrates in PBS

To measure pH response, a 4-MBA modified Q3D-PNA SERS substrate was immersed in PBS with the pH being adjusted from ~4.0 to ~9.0. **Figure 3.3a** shows the SERS spectra in the window of 1300-1800 cm^{-1}, which is the range with the most prominent spectral changes as a function of pH. All the spectra are normalized at the intense peak at 1586 cm^{-1}, assigned as the aromatic ring breathing mode (*v8a*). The peak at ~1420 cm^{-1}, which belongs to the symmetric COO^- stretching mode ($vCOO^-$), increases with the increasing of pH. A larger increase was observed for the pH greater than ~6.5 because of the deprotonation of more carboxyl groups (**Figure 3.3b**). The peak also redshifts with the increasing of pH suggesting that some 4-MBA molecules may still be involved in hydrogen bonding in addition to the possible interaction between COO^- groups and the ring hydrogens. It was also noticed that the shoulder at ~1690 cm^{-1} due to the symmetric C=O stretching mode decreases with the increasing of pH (**Figure 3.3a**).

The inverse behaviors of these two peaks were observed in the previous reports [62-66]. Because of the sensitive response to solution pH, the intensity of the *vCOO*$^-$ peak will be used as the pH indicator in this work.

3.3.3 Interferences from cations and calibrations in different solutions

However, the *vCOO*$^-$ peak of 4-MBA not only responds to the variation of solution pH due to protonation/deprotonation, but also changes with the presence of cations in solution due to chelation. This effect has been used to detect heavy metal ions using SERS by monitoring the shift and intensity change of the *vCOO*$^-$ peak [70]. In this work, mapping pH_e of living cells using SERS would be conducted *in situ* in cell culture media after 24 h incubation. Na^+ and K^+ are the major cations in cell culture media and they have a reverse concentration gradient across the cell membrane to maintain the resting potential [71]. A small amount of divalent cations Ca^{2+} and Mg^{2+} are also present in most of the cell culture media. Cells maintain relative high concentrations of Mg^{2+} but pump Ca^{2+} out [72]. Thus, we studied the potential interferences of these four types of cations (Na^+, K^+, Ca^{2+} and Mg^{2+}) on the SERS peak of *vCOO*$^-$ by adding them one at a time to the pure deionized (DI) water while keeping a constant pH of 7.0 in order to evaluate the cation effect. **Figure 3.4a** shows the SERS spectra in the window of 1350-1500 cm^{-1} of these solutions and DI water. Adding 10 mM Na^+ or K^+ in DI water does not induce any spectral change of the *vCOO*$^-$ peak. The presence of 10 mM Ca^{2+} causes the *vCOO*$^-$ peak to redshift about 6 cm^{-1} and to slightly decrease peak intensity. By adding 10 mM Mg^{2+}, the peak also shows a shift of about 8 cm^{-1} to high wavenumber and a relatively large intensity increase. The SERS spectral changes imply the variations of polarizability of COO^- induced by the chelation of different cations. The divalent cations

exhibit more influences on the *vCOO*$^-$ peak comparing with the monovalent cations because of their higher binding affinities to the carboxylate group [73]. Since the relative intensity of the *vCOO*$^-$ peak to the benzene ring *v8a* peak is used to detect pH, the intensity change of the *vCOO*$^-$ peak with the presence of cations, especially divalent cations, does affect the detection accuracy of this method. In addition, the detection could also be affected by the ionic strength of a solution due to the formation of an electrical double layer that affects the diffusion of protons and other cations. Therefore, it is necessary to measure the pH calibration curves under the real detection conditions.

We investigated the pH response of the *vCOO*$^-$ peak in different solutions including, intracellular mimic (IC), cell culture medium (CM), PBS, DI water and phosphate citrate buffer (PC). **Figure 3.4b** shows the relative intensities of the *vCOO*$^-$ mode to the benzene ring *v8a* mode as a function of pH in aforementioned solutions, and the error bars correspond to the standard deviation of five replicates. Notably, the calibration curves of different solutions are not identical. At the same pH, the relative intensities of the peaks of *vCOO*$^-$ over *v8a* from the intracellular mimic and cell culture medium are much higher than those from the other solutions because of the presence of divalent ions (5 mM Mg^{2+} and 0.15 mM Ca^{2+}) in intracellular mimic and the complexity of the cell culture medium. Clearly, errors would be introduced in the measurements of pH_i or pH_e if they are simply based on the calibration curve built from a buffer solution but in fact that 4-MBA modified SERS substrates are surrounded by complex biological media. Since we would culture the cells on the SERS substrates and map the pH_e *in situ* in the cell culture medium after incubation, we generated the pH calibration curve for the cell culture medium. Remarkably, the calibration curve of the cell culture medium shows

a steeper slope between pH 7.0 and 7.6, offering a resolution of about 0.1 pH units across this range, which is also the ideal range of pH_e, A similar pH sensitivity was reported with 4-MBA modified gold-nanoshells [63]. This pH sensitivity is essential in order to distinguish the pH differences of the microenvironment outside the living cell membranes.

3.3.4 Mapping extracellular pH of living normal and cancer cells in cell culture media

To demonstrate the capability of 4-MBA modified Q3D-PNA SERS substrates in the detection and mapping of the pH_e distribution of single living cells, NIH/3T3 and HepG2 cells were cultured directly on the SERS substrates that were placed in each of the two petri dishes in the cell culture medium for 24 h. A control set was run in parallel by just adding the cell culture medium. After incubation, the optical images and the pH_e SERS mapping of the cells were taken *in situ* using the Renishaw Raman microspectroscopy system. The first row of **Figure 3.5a** shows the 10X optical images of NIH/3T3, HepG2 and the control set on the SERS substrates in bright field. All the cells were well grown and attached to the SERS substrate. The dark squares in the middle are the Q3D-PNAs. The images in the second and third rows are the 50X optical images in bright field and dark field, respectively. The shapes of cell bodies are blurry in the bright field images due to the use of the reflective optical microscope mode, while they are clearer in the dark field images confirming the well attached cells on the Q3D-PNAs.

The pH_e distributions of living cells were mapped out by generating the 2D SERS images of local pH values, which were determined from the calibration curve of the cell culture medium in **Figure 3.4b**. The forth row in **Figure 3.5a** shows the SERS pH images of the Q3D-PNA area (50 μm x 50 μm) with the NIH/3T3 and HepG2 samples,

corresponding to the optical images shown in the second and the third rows. The control set of the cell culture medium was only measured in the center area of the Q3D-PNA, and a uniform pH distribution around 7.5-7.6 was observed. Clearly, the areas of no cells in the SERS pH images of the NIH/3T3 and HepG2 samples display the similar pH range (green color) as that in the control set. The areas where cells attached show lower pH than the area of the cell culture medium only. The pH_e distributions and microdomains at the plasma membrane of both NIH/3T3 and HepG2 cells are shown by color contrast in the pH_e SERS images. The different pH_e values of the cell membranes are believed to be related to the Na^+/H^+ exchangers such as NHE1 distributed in cell membranes that extrude the excess protons outside of the cell [74]. Increased expression and activity of these Na^+/H^+ exchangers are observed in tumor cells. And the more acidic microenvironment outside the tumor cells is also due to their more glycolytic phenotype. **Figure 3.5b** shows histograms of the pH_e of NIH/3T3 and HepG2. The averaged pH_e of the tumor cells HepG2 (pH 7.29 ± 0.06) is more acidic than that of the normal NIH/3T3 cells (pH 7.43 ± 0.10) shown in **Figure 3.5c**. This mapping technique can be used to study the cells adhesion and migration regulated by pH_e.

3.4 Conclusions

In summary, based on the excellent uniformity and reproducibility of Q3D-PNA SERS substrates and the pH calibration curve achieved in the cell culture medium, the pH_e distributions of living cells were mapped out by using 4-MBA modified SERS substrates. This technique can be used for the differentiation between normal and tumor cells. Moreover, it will benefit the study of metabolisms and functions of living cells as well as transmembrane drug delivery ruled by the extracellular acidity.

3.5 Tables

Table 3.1 The assignment of SERS vibrational frequencies for 4-MBA

4-MBA	
SERS (cm^{-1})	**Assignments[a]**
524	Si + ν_{CS}
696	β_{OCO} +ν_{CS}
722	ν_{4b}
850	β_{COO^-}
1014	ν_{13}
1074	ν_{1}
1141	ν_{15}
1181	ν_{9a}
1420	ν_{COO^-}
1482	ν_{19a}
1589	ν_{8a}
1690	$\nu_{C=O}$

[a] ν, stretching; β, in plane bending

3.6 Figures

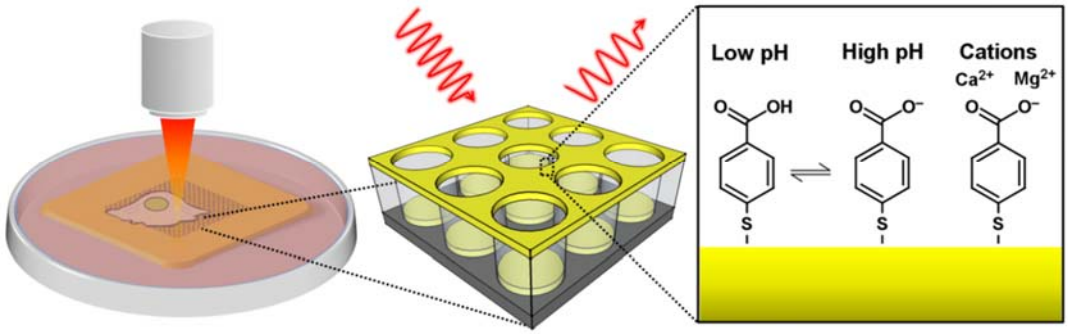

Figure 3.1 Schematic illustration of mapping pH_e of a single living cell cultured on a 4-MBA modified Q3D-PNA SERS substrate in the culture media.

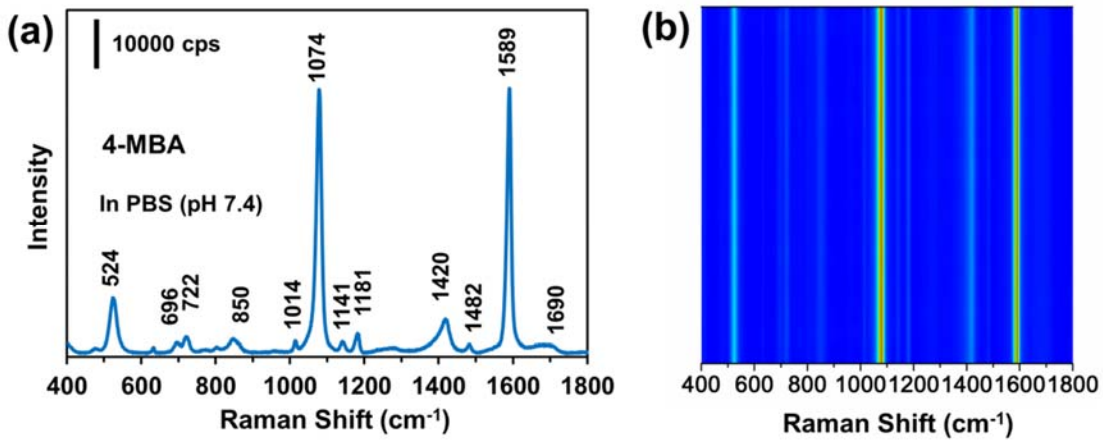

Figure 3.2 SERS spectrum of 4-MBA and reproducibility test

(a) SERS spectrum of 4-MBA in PBS (pH 7.4). The λ_{ex} = 785 nm, P_{laser} = 1 mW, and t = 10 s. (b) SERS contour of 32 spectra of 4-MBA collected from different spots on one Q3D-PNA SERS substrate.

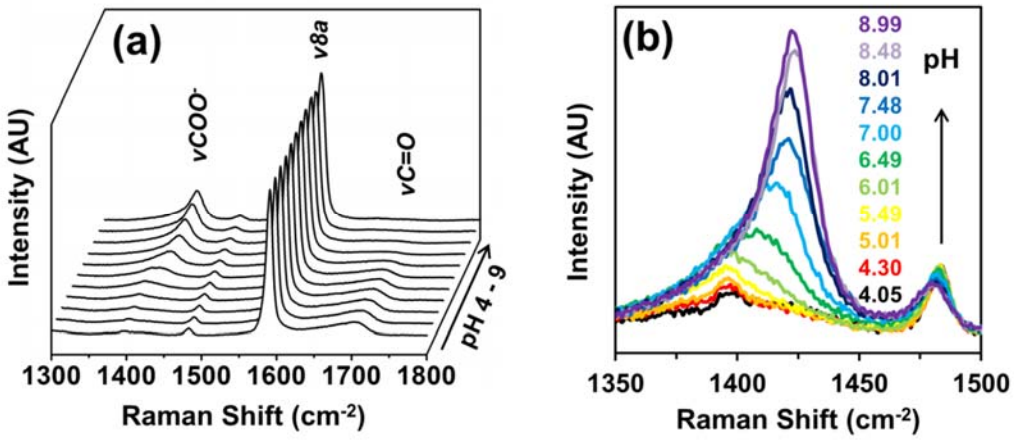

Figure 3.3 SERS spectra of 4-MBA responding to pH changes

(a) SERS spectra of 4-MBA modified Q3D-PNA substrates in PBS with pH from ~4.0 to ~9.0. (b) A close-look of the intensity of the *vCOO*$^-$ mode at ~1420 cm^{-1} varies with pH due to its degree of protonation/deprotonation.

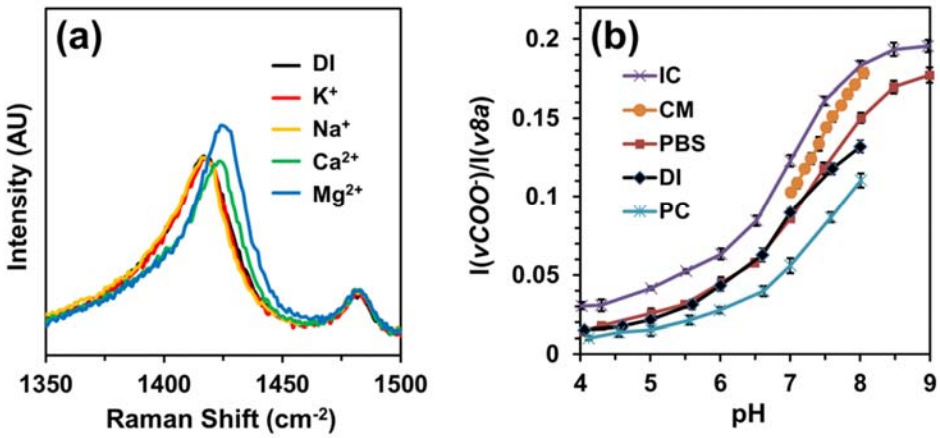

Figure 3.4 Influence of cations on pH detections

(a) The peak of the *vCOO*$^-$ mode at ~1420 cm^{-1} varies with the presence of 10 mM different cations in DI water at pH 7.0. (b) The pH calibration curves for different detection solutions made by plotting the relative intensities of the *vCOO*$^-$ to the benzene ring *v8a* mode as a function of pH.

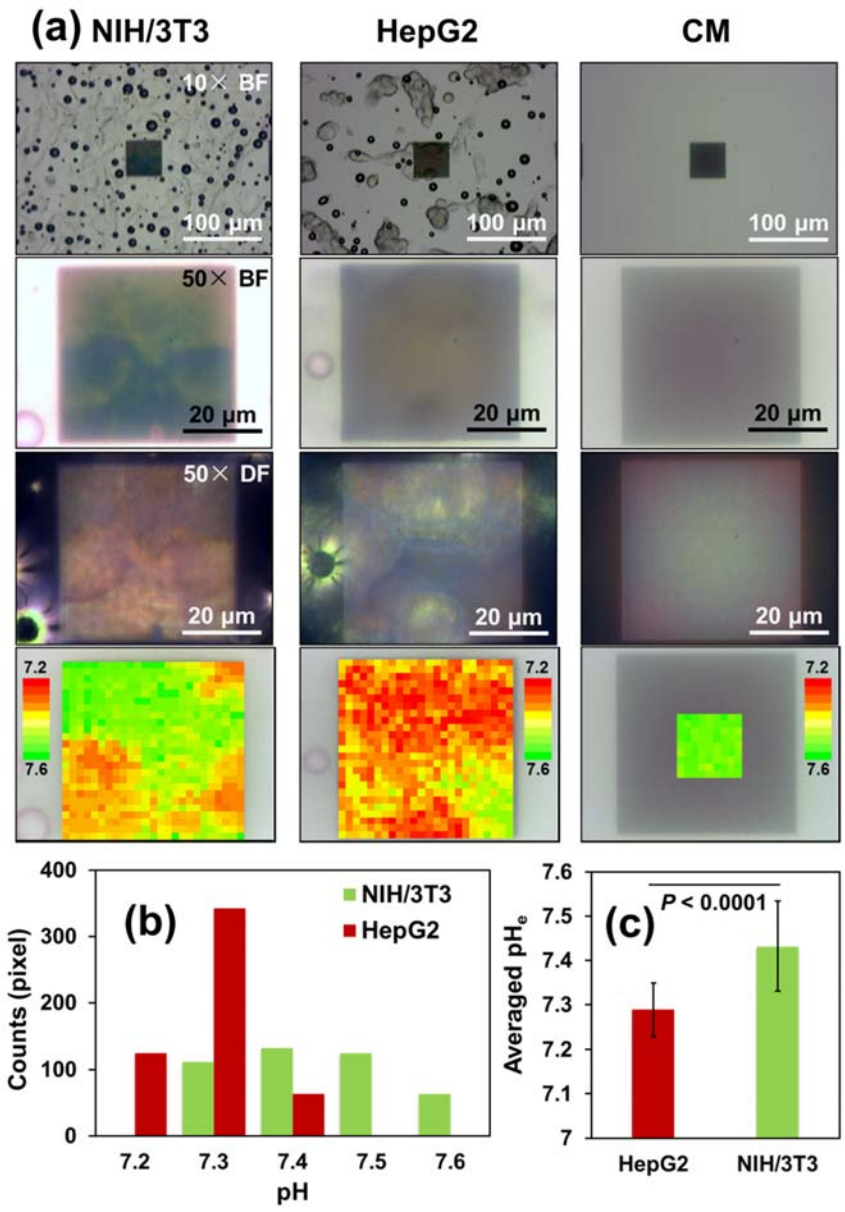

Figure 3.5 Optical images and pH_e SERS mapping of NIH/3T3 and HepG2 cells

(a) Optical images and pH_e SERS mapping of NIH/3T3 and HepG2 cells cultured on the 4-MBA modified Q3D-PNA SERS substrates in the CM. The control was the 4-MBA modified Q3D-PNA in the CM only. (b) Histogram of the pH_e of NIH/3T3 and HepG2 cells. (c) Averaged pH_e of NIH/3T3 and HepG2 cells (collected from 5 cells, independent t-test, $P < 0.0001$).

Chapter 4 Stealth Surface Modification of Surface-Enhanced Raman Scattering Substrates for Sensitive and Accurate Detection in Protein Solutions

Reliable surface-enhanced Raman scattering (SERS) based biosensing in complex media is impeded by nonspecific protein adsorptions. Because of the near-field effect of SERS, it is challenging to modify SERS-active substrates using conventional nonfouling materials without introducing interference from their SERS signals. Herein, we report a stealth surface modification strategy for sensitive, specific and accurate detection of fructose in protein solutions using SERS by forming a mixed self-assembled monolayer (SAM). The SAM consists of a short zwitterionic thiol, N,N-Dimethyl-cysteamine-carboxybetaine (CBT), and a fructose probe 4-mercaptophenylboronic acid (4-MPBA). The specifically designed and synthesized CBT not only resists protein fouling effectively, but also has very weak Raman activity compared to 4-MPBA. Thus, the CBT SAM provides a stealth surface modification to SERS-active substrates. The surface compositions of mixed SAMs were investigated using x-ray photoelectron spectroscopy (XPS) and SERS, and their nonfouling properties were studied with a surface plasmon resonance (SPR) biosensor. The mixed SAM with a surface composition of 94% CBT demonstrated a very low bovine serum albumin (BSA) adsorption (~3 ng/cm^2), and moreover, only the 4-MPBA signal appeared in the SERS spectrum. Using this surface-modified SERS-active substrate, quantification of fructose over clinically relevant concentrations (0.01-1 mM) was achieved. Partial least squares regression (PLS) analysis showed that the detection sensitivity and accuracy were maintained for the measurements in 1 mg/mL BSA solutions. This stealth surface modification strategy provides a novel

route to introduce nonfouling property to SERS-active substrates for SERS biosensing in complex media.

4.1 Introduction

Biosensing based on surface-enhanced Raman scattering (SERS) platforms has made tremendous progress due to the advances of controllable colloidal metallic nanoparticle synthesis, precise nanofabrication and surface modification techniques [75-77]. The extremely high sensitivity has been realized by well controlled metallic nanoparticle size, shape and distance, as well as different two-dimensional and three-dimensional plasmonic nanostructures [78]. The detection specificity can be obtained from the vibrational modes of the target molecule directly adsorbed on SERS-active substrate surfaces, or *via* Raman reporters and probes. The high sensitivity and molecular specificity of SERS have led to an enormous amount of biosensing applications, such as the detection of small biomolecules [16, 79], DNA strands [8, 80, 81], proteins [82], microorganisms [43, 83, 84], and cancer cells [85]. Nevertheless, reliable biosensing based on SERS platforms in complex biological media is still challenging due to interfering species and nonspecific adsorption of proteins [86]. Background noise from interfering species could mask the signals from target analytes because a bare SERS-active surface lacks of selectivity. Nonspecific adsorption of proteins could impede the adsorption of target analytes to SERS-active substrate surfaces.

In order to promote target analytes to SERS substrate surfaces and thus to reduce interferences, several surface modification methods have been developed. By forming mixed self-assembled monolayers (SAMs) of alkane or benzyl thiols on SERS-active substrates, small molecules such as glucose and 3,4-methylenedioxymethamphetamine

(MDMA) partition to the mixed SAM layer, and thus enabled the detections [25, 87]. Instead of physical attractions, thiolated aptamers have been used to modify SERS substrates to recognize and bind analytes [88, 89]. Then, the SERS detection was accomplished by measuring either the SERS signals of the Raman label conjugated to the analyte vasopressin [88] or the SERS signals of the analyte ricin [89]. Recognition between antibody-antigen has also been employed for SERS biosensing [90, 91]. In these studies, molecules with thiolated phenyl ring or dithiolated multiple phenyl rings were used as probes or reporters to detect the antigens. In fact, surface modifications based on molecules of benzenethiol with different functional groups, which serve as probe molecules, have attracted more attention recently [92-95]. They can form SAMs on SERS-active substrates, creating strong and reproducible SERS signals. Density functional theory (DFT) calculations showed that the probes with benzenethiol structure on SERS-active substrates exhibit a large intrinsic Raman activity due to the chemical enhancement mechanism [96]. This offers a great advantage since the detection of analytes is achieved by monitoring the SERS spectral changes of the probe molecules upon interactions with targeted analytes. The strong SERS signals of phenyl rings can amplify the detection signals over other interferences. For example, 4-mercaptobenzoic acid (4-MBA) was used to functionalize gold or silver nanoparticles for intracellular pH sensing because the SERS spectrum of 4-MBA changes in response to the interaction between the carboxyl group and protons [92, 93]. A specially designed peptide receptor conjugated with thiophenol group was modified on silver nanoparticles; quantitative detection of an oncogenic protein in cell extracts was accomplished by monitoring the SERS spectral changes due to the reorientation of the phenyl ring [94]. Our group

recently reported the using of 4-mercaptophenylboronic acid (4-MPBA) for quantitative and selective detection of fructose in artificial urine also based on observing the relative SERS intensity changes of the totally and nontotally symmetric ring vibrational modes due to the symmetry breaking upon fructose binding to the boronic acid group [95].

Despite the successful detections using these surface modifications, a suppression of sensitivity and accuracy in complex media was observed in comparison to the results obtained in simple buffer solutions [94, 95, 97]. It was found that nonspecific adsorbed proteins from the complex media formed a dense layer prohibiting the diffusion and recognition of target molecules. Thus, a nonfouling modification with high surface coverage is desired to resist the nonspecific protein adsorption in order to maintain the detecting sensitivity and accuracy, as well as to prolong the stability and lifetime of the SERS-active substrates. However, SERS is a near-field effect and is most sensitive to the first monolayer of molecules on the SERS-active substrate surfaces [98]. If the SERS-active substrate surface is occupied by the nonfouling modification, signals of the modification may dominate the spectrum as an overwhelming background that could cover or overlap with the signals from target molecules. Therefore, surface modification of SERS-active substrates pose a great challenge to produce the capabilities to resist fouling without introducing unwanted signals, and also can respond to the interactions of immobilized probe molecules to target molecules for sensitive, specific and accurate SERS detection in complex media.

To tackle this challenge, we developed a stealth surface modification approach by modifying SERS-active substrate surfaces with a mixed SAM, containing molecules with dramatically different intrinsic Raman activities. Selective detection and signal

amplification are achieved by the molecule with strong Raman activity, while nonfouling properties are achieved by the molecule with weak Raman activity. In this work, we designed and synthesized a short zwitterionic thiol, N,N-Dimethyl-cysteamine-carboxybetaine (CBT), and used it to modify SERS-active substrate surfaces. This modification provided the surface with nonfouling properties because the carboxybetaine head group can bind water strongly and resist protein adsorption [99, 100]. CBT is expected to have a remarkably small Raman cross-section as a small aliphatic molecule [101]. As a proof of concept, we formed 4-MPBA and CBT mixed SAMs on gold quasi-three-dimensional plasmonic nanostructure arrays (Q3D-PNAs) [43, 95] to detect fructose in protein solutions as illustrated in **Figure 4.1a**. The surface composition of two components is critical for maximizing the nonfouling properties without reducing the sensitivity, specificity and accuracy of SERS sensing. Therefore, the mixed SAMs with different compositions were studied using SERS and X-ray photoelectron spectroscopy (XPS). Their nonfouling performances were assessed by a surface plasmon resonance (SPR) biosensor. An optimized ratio of CBT to 4-MPBA was determined, and used to modify the Q3D-PNAs. Detections of fructose with the concentrations in the clinically relevant range were conducted in PBS buffers and BSA solutions. Partial least squares regression (PLS) analysis was applied and the results showed that the sensitivity and accuracy were maintained for the detections in BSA solutions. The resistance to protein adsorption and the invisibility of its own SERS signal make CBT a viable option for the stealth surface modification of SERS-active substrates.

4.2 Experimental Section

4.2.1 Materials

4-mercaptophenylboronic acid, D-(−)-fructose, phosphate buffered saline packet (PBS, pH 7.4 and ionic strength 150 mM) and albumin from bovine serum were purchased from Sigma-Aldrich (St. Louis, MO). Dithiothreitol, triethylamine, acrylic acid, and cysteamine dihydrochloride were purchased from TCI America (Portland, OR). Diethyl ether and anhydrous methanol were purchased from J. T. Baker (Center Valley, PA). High-purity deionized (DI) water was obtained with a Millipore water purifier system.

4.2.2 Synthesis of N,N-Dimethyl-cysteamine-carboxybetaine

***N*,*N*, *N*',*N*'-Tetramethyl-cystamine-di-carboxybetaine (CBT disulfide) (2).** Bis(2-dimethylaminoethyl) disulfide dihydrochloride **1** (10.1 g, 35.9 mmol) and triethylamine (10.0 mL, 71.7 mmol) were dissolved in anhydrous methanol (100 mL) and the solution was stirred at room temperature for 30 min. Acrylic acid (48.3 mL, 710 mmol) and hydroquinone (500 mg, 4.54 mmol) were then added to the mixture, which was stirred at 50 °C for 18 h. The solution was concentrated on the rotovap to a syrupy consistency. Diethyl ether (500 mL) was added to the viscous residue resulting in a suspension that was stirred at room temperature for 12 h. The precipitate was filtered on a Buchner funnel, washed with cold ether and dried under high vacuum to afford the pure product as a fine white powder (11.6 g, 32.9 mmol). Yield: 92%. ^{1}H NMR (300 MHz, D-$_{2}$O) δ (ppm): 3.60 (t, 4H, J = 7.6 Hz), 3.56 (t, 4H, J = 7.6 Hz), 3.07 (t, 4H, J = 4.7 Hz), 3.03 (s, 12H), 2.85 (t, 4H, J = 7.5 Hz).

***N*,*N*-Dimethyl-cysteamine-carboxybetaine (CBT) (3).** CB-thiol disulfide **3** (3.20 g, 9.08 mmol) was dissolved in anhydrous methanol (50.0 mL). Dithiothreitol (1. 47 g, 9.53 mmol) was added to the solution and the mixture was stirred at room temperature for 12 h. The solution was concentrated on the rotovap to remove about 90% of methanol and diethyl ether (150 mL) was added to the residue, resulting in a suspension. After stirring in ether for 12 h, the precipitate was filtered out on a Buchner funnel, washed with ether and dried under high vacuum to afford the pure product as a white powder (1.37 g, 7.72 mmol). Yield: 85%. ^{1}H NMR (300 MHz, D_2O) δ (ppm): 3.51 (t, 2H, J = 6.4 Hz), 3.49 (t, 2H, J = 6.4 Hz), 2.97 (s, 6H), 2.82 (m, 4H). ^{13}C NMR (75 MHz, D_2O) δ (ppm): 174.4, 67.3, 60.8, 51.9, 29.1, 17.8.

4.2.3 Fabrication and surface modification of gold Q3D-PNA SERS substrates

Gold Q3D-PNA SERS substrates are composed of physically separated gold thin films with subwavelength nanoholes on the top and gold nanodiscs at the bottom of the wells as illustrated in **Figure 4.1b**. They were fabricated *via* electron beam lithography (EBL) following the same method reported previously [95]. Ellipsometery (J.A. Woollam, α-SE) was used to measure the thickness of PMMA and gold coatings, and the dimensions of the Q3D-PNA were confirmed by scanning electron microscope (SEM, FEI Sirion) shown in **Figure 4.1c**. Pure CBT, pure 4-MPBA, and 4-MPBA/CBT mixed SAMs were formed on the surface of a gold Q3D-PNA SERS substrates by soaking UV ozone-cleaned substrates in a 1 mM pure CBT, 1 mM pure 4-MPBA or 1 mM 4-MPBA/CBT (molar ratio: 10/90 and 1/99) absolute ethanol solution for 12 h, followed by rinsing with ethanol and deionized (DI) water and blowing dry in a stream of nitrogen.

4.2.4 Analysis of SAMs using XPS

The pure CBT, pure 4-MPBA and 4-MPBA/CBT mixed SAMs were characterized using X-ray photoelectron spectroscopy (XPS) on a Kratos Axis Ultra XPS instrument using monochromated Al Kα radiation (1486.6 eV). Survey spectra and detail scans of C 1s, N 1s, B 1s, and S 2p were acquired using a pass energy of 150 eV. High-resolution spectra of C 1s and S 2p were acquired using a pass energy of 50 eV. Spectra were collected with the analyzer at 55° with respect to the surface normal of the sample. Typical pressure in the chamber during spectral acquisition was 10^{-9} Torr. Three spots on two or more replicates sample were analyzed. Computer aided surface analysis (CasaXPS) software was used to calculate compositions from the peak areas.

4.2.5 Nonfouling assessment using an SPR biosensor

A four-channel custom-built SPR sensor was used to measure the protein adsorptions on the surfaces of gold SPR chips modified with different SAMs. The pure CBT, pure 4-MPBA and 4-MPBA/CBT mixed SAMs were formed on UV ozone-cleaned gold SPR chips following the same aforementioned method. The modified SPR chips were rinsed with ethanol, DI water, dried by nitrogen, and then mounted on the SPR device. The temperature controller was set to 25 ± 0.01°C. Protein adsorption was measured by sequentially flowing PBS, 1 mg/mL BSA in PBS, and PBS over the SAM surface each for 10 min at 40 μL/min flow rate by a peristaltic pump. The wavelength shift between the baselines before protein injection and after rinsing with PBS was used to quantify the total amount of protein adsorbed. A reference channel containing a PBS flow was used for each chip to correct for baseline drift. A 1 nm wavelength shift from

the SPR at 750 nm represents a surface coverage of 17 ng/cm^2 adsorbed proteins. The detection limit for the SPR sensor is 0.3 ng/cm^2.

4.2.6 Detection of fructose in PBS and BSA solutions using SERS

A Renishaw InVia Raman spectroscope connected to a Leica DMLM upright microscope was used to collect SERS spectra. A 785 nm laser was used as an excitation laser, which was focused on a Q3D-PNA using a 50x (N.A. = 0.8) objective and the laser power of 1 mW. A spectral resolution of 1.1 cm^{-1} can be achieved, and spectra were collected in the range of 400 to 1700 cm^{-1}. The Q3D-PNA SERS substrates modified by pure CBT SAM, pure 4-MPBA SAM, or 4-MPBA/CBT mixed SAM were placed in a custom-made Teflon container, a volume of 150 μL PBS solution was added, and then a piece of microscope cover glass was placed on top of the container carefully to avoid forming bubbles. SERS spectra of 4-MPBA SAM and 4-MPBA/CBT mixed SAM were taken with CCD exposure time of 10 s and a single accumulation while those of CBT SAM with 10 accumulations to increase the signal/noise ratio. To detect fructose in PBS or proteins solutions, after placing a SERS substrate modified with 4-MPBA/CBT mixed SAM in the Teflon holder, a volume of 150 μL PBS solution or 1 mg/mL BSA solution spiked with concentrations of fructose (0.01, 0.05, 0.10, 0.16, 0.23, 0.29, 0.35, 0.41, 0.47, 0.54, 0.61, 0.68, 0.75, 0.83, 0.90, and 0.99 mM) was added on the surface carefully. Then the container was covered with a piece of microscope cover glass. The SERS spectra were collected after immersion in each concentration solution for 20 min with CCD exposure time of 10 s and a single accumulation. Three replicates were measured for each concentration.

4.2.7 Chemometrics method

All SERS spectral data processing was performed using the Unscrambler® X (CAMO Software, Oslo, Norway) software package [102]. Prior to analysis, all spectra were baseline corrected by fitting the raw spectrum to a fourth-order polynomial and then subtracted. The baseline corrected spectra were normalized with respect to the peak at 1075 cm^{-1} for 4-MPBA SAM and 4-MPBA/CBT SAM modified samples followed by taking the Savitzky–Golay 1st derivative (5 points, 2nd degree). Then data analysis was conducted using partial least squares (PLS) method with leave-one-out, cross validation for evaluating the effectiveness of SERS technique in predicting different fructose concentrations (0-1 mM) in PBS buffer [103]. This analysis used one sample as the validation set and the remaining samples as the training set. The process was repeated for all samples (*i.e.* 51 samples). The root mean squared error of prediction (RMSEP) was used to judge the accuracy of predictions. It was calculated from the cross validation data as RMSEP=$\sqrt{\frac{1}{51}\sum_{51}(prediction - reference)^2}$

For both of the pure 4-MPBA SAM and 4-MPBA/CBT mixed SAM modified SERS sensors, their PLS calibration models were built in PBS buffer. Then, the models were used for the prediction of different known concentrations of fructose in BSA solution after immersion of the modified sensors in BSA solution (1 mg/mL) for 4 h to evaluate the potential influence of protein fouling.

4.3 Results and Discussion

4.3.1 SERS spectra of pure and mixed SAMs

The short zwitterionic thiol, CBT, was designed to have a carboxybetaine head group, in which both cationic and anionic groups are on the same molecule. Due to the electrostatically induced hydration, it can be highly resistant to nonspecific protein adsorption. There is a short spacer between the thiol and carboxybetaine group so that CBT and 4-MPBA can form a mixed SAM with similar height. The reaction route for the synthesis of CBT is presented in **Figure 4.2**.

The pure CBT SAM was formed on the gold surface of a Q3D-PNA SERS substrate. The SERS spectrum of the CBT SAM in PBS is shown in **Figure 4.3** (bottom purple line). Because of the small Raman scattering cross-section, the measurement was achieved by collecting the spectrum with 10 accumulations to improve the signal-to-noise ratio. Characteristic peaks are observed from both the quaternary amine and carboxyl acid groups of CBT. The strong peaks at 756 and 1079 cm^{-1} are attributed to the symmetric and anti-symmetric stretching vibration of the quaternary amine group (C_4N^+), respectively [104, 105]. The stretching modes of the carboxyl acid group (COO^-) are illustrated at 1360 and 1585 cm^{-1} [104, 106]. In addition, the CS stretching mode at 672 cm^{-1} and the in-plane bending mode of CS-Au at 847 cm^{-1} indicate that CBT adsorbs dissociatively as thiolate and forms a gold-sulfur bond [44]. The assignments of each peak are given in **Table 4.1**.

Since CBT will serve as the nonfouling background while 4-MPBA will be used as a fructose reporter, the ratio of 4-MPBA to CBT of the mixed SAM is crucial in order to maximize the detection sensitivity while minimizing protein fouling. We modified the

Q3D-PNA SERS substrates with 4-MPBA/CBT mixed SAMs using the molar ratios of 10/90 and 1/99 for 4-MPBA/CBT in bulk solutions. **Figure 4.3** shows the SERS spectra of these two mixed 4-MPBA/CBT SAMs in PBS on Q3D-PNA SERS substrates. For comparison, the SERS spectra of the pure 4-MPBA SAM and pure CBT SAM are also shown in **Figure 4.3**. The SERS spectrum of pure 4-MPBA SAM is the same as we reported before [95]. The signal of a pure CBT SAM is about 170-fold lower than that of a pure 4-MPBA SAM. 4-MPBA has a larger Raman cross-section than CBT from the benzene ring. In addition, thiolated linkers with conjugated π-electrons such as 4-MPBA allow more efficient electron transfer and molecular orbital overlapping, inducing a higher chemical enhancement factor over alkanethiols such as CBT [51]. The sharp difference between their intrinsic SERS activity ensures the possibility to increase the ratio of CBT in the 4-MPBA/CBT mixed SAM to provide a nonfouling modification while the SERS signals of CBT are still invisible. Indeed, as can be seen in **Figure 4.3**, the enlarged spectra of two mixed SAMs are very similar to that of the pure 4-MPBA SAM. The absolute intensities of characteristic peaks of 4-MPBA are decreased with a decreasing molar ratio of 4-MPBA to CBT in the bulk solution. No peaks of CBT are observed even in the enlarged spectrum of the mixed 4-MPBA/CBT (1/99) SAM. We noticed that with an increase in the ratio of CBT to 4-MPBA, the relative intensity ratio of the shoulder at 1065 cm^{-1} and the peak at 1075 cm^{-1} is increased, while that of the shoulder at 1574 cm^{-1} and the peak at 1587 cm^{-1} is decreased. This indicates a possible ring reorientation of 4-MPBA with the incorporation of CBT.

It is known that the ratio of two components forming a SAM on a surface is different from that in the bulk solution. We estimated the surface ratio of 4-MPBA/CBT

by taking the ratio of the absolute intensity of the peak at 1075 cm^{-1}. We assumed that the surface coverage of pure 4-MPBA and 4-MPBA/CBT mixed SAMs is the same and that one CBT molecule replaces one 4-MPBA molecule on the SERS substrate surface. In this way, the decrease of the intensity of peak at 1075 cm^{-1} is directly due to the reducing number of 4-MPBA molecules on the surface. Based on this assumption, we obtained the surface ratios of 4-MPBA/CBT of mixed SAMs are 31/69 and 6/94 corresponding to the molar ratio of 10/90 and 1/99 in the bulk solutions, respectively. The higher fraction of 4-MPBA molecules in the SAMs may be attributed to the stronger π-π interactions between phenol rings which make 4-MPBA SAMs more stable than the SAMs formed by the short alkanethiol [45].

4.3.2 XPS investigation of pure and mixed SAMs

The pure CBT SAM, pure 4-MPBA SAM and 4-MPBA/CBT mixed SAMs were further characterized using the surface sensitive technique XPS. **Figure 4.4** shows the XPS high-resolution spectra of carbon (C 1s) and the detailed spectra of boron (B 1s) and nitrogen (N 1s) of the SAMs. The C 1s spectrum of the pure CBT SAM has two major peaks centered at 285.5 and 289.1 eV, corresponding to the carbon atom bonded to a nitrogen atom (C-N) or another carbon atom (C-C) and the carbon atom in the carboxylate group (O-C=O), respectively [107]. A small peak at 286.8 eV corresponding to the electron-deficient carbon atom bonded to a sulphur atom (C-S) was also fitted to the C 1s spectrum. The N 1s spectrum of the pure CBT SAM shows a peak at the binding energy of 402.3 eV [107]. The high-resolution spectrum of S 2p of the pure CBT SAM shown in **Figure 4.5** can be fitted to one state of sulphur species at the surface with an S $2p_{3/2}$ binding energy at 162.0 eV, indicating sulphur atoms are bound to the surface. The

C 1s, N 1s and S 2p spectra show that a well-packed monolayer of CBT is formed on the gold surface. The C 1s photoelectron peak of the pure 4-MPBA SAM is centred at 284.2 eV with a very small shoulder at 286.8 eV, corresponding to the carbon atoms of the aromatic ring (C=C) and the carbon atom bonded to sulphur atom (C-S), respectively, which are consistent with the spectrum reported before [108]. The B 1s spectrum of the pure 4-MPBA shows a peak at the binding energy of 191.2 eV. The high resolution C 1s spectra of the two 4-MPBA/CBT (10/90 and 1/99) mixed SAMs exhibit the characteristic peaks of both 4-MPBA and CBT but the intensities vary with the ratio of two components. The characteristic peak of the 4-MPBA SAM at ~284.2 eV decreases significantly to a tiny shoulder for the 4-MPBA/CBT (1/99) mixed SAM. The XPS detail spectra of B 1s and N 1s also show the same trend with the ratio of two components. There is almost no detectable B 1s peak but a strong N 1s peak for the 4-MPBA/CBT (1/99) mixed SAM. The XPS results clearly show that CBT occupies most of the surface for the 4-MPBA/CBT (1/99) mixed SAM. We calculated the ratio of the two components on the surface using the high resolution C 1s spectrum with the C=C peak for 4-MPBA and the /C-N and C-C peaks for CBT. The area ratio of the C=C peak to the he C-N and C-C peaks is 5/95, which is in a good agreement with the estimation from the SERS spectrum.

4.3.3 Nonfouling evaluation of mixed 4-MPBA/CBT SAMs

The nonspecific protein adsorption on different SAM modified gold surfaces were measured using an SPR biosensor. The pure CBT, pure 4-MPBA and 4-MPBA/CBT mixed SAMs were tested with a single protein – bovine serum albumin (BSA) solution (1 mg/mL) because BSA has been commonly used to block surfaces due to its high affinity

to many surfaces. The typical SPR sensorgrams are shown in **Figure 4.6**. The pure CBT SAM shows a nonfouling property with the BSA adsorption of 2.2 ± 0.8 ng/cm^2. In contrast, the pure 4-MPBA SAM exhibits a strong BSA adsorption of 148.4 ± 16.5 ng/cm^2. For the 4-MPBA/CBT mixed SAMs, **Figure 4.6** shows that the mixed SAM formed by the ratio of 4-MPBA/CBT of 10/90 in the bulk solution can significantly reduce the BSA adsorption to 27.1 ± 8.8 ng/cm^2. With further increasing CBT in 4-MPBA/CBT mixed SAM to 1/99, the BSA adsorption is reduced to 3.0 ± 0.6 ng/cm^2, which is similar to the amount on the surface of the pure CBT SAM. Therefore, the 4-MPBA/CBT (1/99) mixed SAM is sufficient enough to resist protein adsorption, which was selected for the investigation of detecting fructose in protein solutions.

4.3.4 4-MPBA/CBT mixed SAM modified SERS-active substrates for fructose detection

As shown in **Figure 4.3**, although the absolute SERS intensities of 4-MPBA in 4-MPBA/CBT mixed SAMs are decreased with the increasing of CBT ratio, the spectra are still dominated by the 4-MPBA signal. In our previous study, we demonstrated that the pure 4-MPBA SAM modified Q3D-PNA SERS substrate can sensitively and specifically detect fructose in artificial urine [95]. The symmetry breaking of 4-MPBA upon fructose binding leads to the change of area ratio between totally symmetric 8a ring mode (1574 cm^{-1}) and nontotally symmetric 8b ring mode (1587 cm^{-1}), which enables the detection. In this work, we first tested how the SERS signals of 4-MPBA change upon the binding of fructose to the 4-MPBA/CBT (1/99) mixed SAM modified Q3D-PNA SERS substrate. We immersed a 4-MPBA/CBT (1/99) mixed SAM modified Q3D-PNA SERS substrate in 1 mM fructose PBS solution for 1 h to ensure binding equilibrium and then took the

SERS spectrum. **Figure 4.7** shows the SERS spectrum of 4-MPBA/CBT (1/99) mixed SAM after fructose binding. For comparison, the SERS spectrum taken from the 4-MPBA/CBT (1/99) mixed SAM in PBS is also shown **Figure 4.7**. Several spectral changes are observed between the two spectra. The peak of 8a (1587 cm^{-1}), a totally symmetric mode, significantly decreased while the peak of 8b (1574 cm^{-1}), a nontotally symmetric mode increased. The peaks of the 19a (1487 cm^{-1}) and 19b (1472 cm^{-1}) modes varied in a similar trend. All these changes indicate that the symmetry of a 4-MPBA molecule is changed from nearly C_{2v} to C_s because of forming fructose-4-MPBA ester upon fructose binding [48]. The other changes of the peaks at 420, 1000, 1024, and 1065 cm^{-1} related to the 7a + ν_{CS}, 12, 18a, and ν_{CS} modes, respectively, suggesting the possible reorientation and charge redistribution of the benzene ring. The results show that even with a very small amount of 4-MPBA molecules (5-6%) on the Q3D-PNA SERS substrate for the 4-MPBA/CBT (1/99) mixed SAM, the variation of the SERS spectrum of 4-MPBA upon fructose binding is still very obvious. Therefore, the 4-MPBA/CBT (1/99) mixed SAM modified Q3D-PNA SERS substrate exhibits both excellent nonfouling properties and capability to detect fructose.

4.3.5 Quantitative detection of fructose in PBS

Figure 4.8a shows the SERS spectra of the 4-MPBA/CBT (1/99) mixed SAM modified Q3D-PNA SERS substrates immersed in a series of concentrations of fructose from 0.01 to 1 mM, which is in the clinically relevant range [28, 109]. The spectrum of each concentration was taken after immersion for 20 min to ensure quick yet quantitative measurement. Clearly, higher fructose concentration resulted in more obvious spectral changes. **Figure 4.8a** shows the Raman shift range of 950-1650 cm^{-1}, which contains the

most distinct spectral changes. To completely extract and quantify the spectral information related to fructose concentrations, multivariate data analysis of PLS regression was applied for the evaluation. The PLS calibration model for fructose detection using the 4-MPBA/CBT (1/99) mixed SAM modified surfaces in PBS was obtained using spectra of 51 samples ranging from 0 to 1 mM. Each spectrum was pre-processed by normalizing the intensity to the 1075 cm^{-1} peak and then taking the Savitzky–Golay 1st derivative (5 points, 2nd degree). The PLS factors were derived from the spectra from 950 to 1650 cm^{-1}. **Figure 4.8b** shows the first and second factors for PLS calibration. They are all related with the spectral changes of 4-MPBA upon fructose binding including the symmetry breaking and ring's reorientation. **Figure 4.8c** shows the root mean squared error of cross-validation (RMSECV) as a function of loading factors, which indicates 4 loading factors work well to minimize the RMSECV, and meanwhile, describe the accuracy of the model itself. A satisfactory calibration was achieved using just four factors to avoid over-modelling data. **Figure 4.8d** shows the PLS result that a linear plot of predicted concentration *versus* actual concentration with R^2 = 0.99 generated by applying a leave-one-out cross-validated calibration model. The formal root mean squared error of prediction (RMSEP) is 0.018 mM, representing the accuracy of predicted concentration.

4.3.6 Accurate fructose detection in BSA solution

In order to evaluate the accuracy of the fructose detection in BSA solution with the 4-MPBA/CBT (1/99) mixed SAM modified Q3D-PNA SERS substrates, we immersed the modified substrate in a 1 mg/mL BSA solution at 4°C for 4 h and then the substrate was immersed in a 1 mg/mL BSA solution spiked with a series concentrations

of fructose from 0.05 to 0.9 mM. The SERS spectra were taken after immersion for 20 min for each concentration and then to validate the predicted concentrations based on the PLS calibration model. The validation used 9 data points. The predicted concentrations were obtained from the PLS calibration model built upon the results in PBS. **Figure 4.9a** shows the plot of the predicted concentrations *versus* the actual concentrations for the fructose detection in BSA solution after BSA blocking using the 4-MPBA/CBT (1/99) mixed SAM modified SERS substrate. Almost all the data points lie near the prefect prediction diagonal and the RMSEP is 0.02 mM. This result indicates that the 4-MPBA/CBT (1/99) mixed SAM modified Q3D-PNA SERS substrates maintain the detection accuracy and sensitivity as in PBS even after the substrates are immersed in BSA solution and the measurements are carried out at the presence of BSA in solution. This is because a 4-MPBA/CBT (1/99) mixed SAM highly resists protein fouling as demonstrated by the SPR measurement. In contrast, the detection accuracy is lost if the SERS substrates are modified by a pure 4-MPBA SAM. To quantitatively demonstrate this, we first built the PLS model for the pure 4-MPBA SAM modified surface using the SERS spectra of different concentrations of fructose in PBS as we did for the 4-MPBA/CBT (1/99) mixed SAM. We then took the SERS spectra of different concentrations of fructose in 1 mg/mL BSA solution after the BSA blocking as aforementioned. **Figure 4.9b** shows that all the predicted concentrations are smaller than the actual ones, with a RMSEP = 0.23 mM. Apparently, a protein fouling layer was formed on the pure 4-MPBA SAM modified SERS substrate during the blocking step as well as the subsequent detection step. The protein fouling layer inhibits the diffusion of

fructose from the solution to the surface to bind with 4-MPBA and thereby suppresses the sensitivity and accuracy of the fructose detection.

4.4 Conclusions

In this work we demonstrated a stealth surface modification strategy for sensitive and accurate detection of fructose in protein solutions using SERS by modifying the SERS substrate with a mixed SAM of 4-MPBA and CBT. For the mixed SAM formed with a solution molar ratio of 1/99 of 4-MPBA and CBT, the surface exhibits excellent nonfouling properties with BSA adsorption around 3 ng/cm^2 measured by an SPR biosensor. Albeit the surface is occupied by approximately 94% of CBT for this mixed SAM, only 4-MPBA signals appear in the SERS spectrum because of the dramatic difference between their intrinsic Raman activities. The nonfouling property and invisibility in SERS spectra make CBT a stealth surface modification. The detections of fructose in protein solution over clinically relevant concentration range (0.01–1 mM) were carried out using the SERS substrates modified with this 4-MPBA/CBT (1/99) mixed SAM and a RMSEP of 0.018 mM was demonstrated by applying PLS regression analysis. The detection sensitivity and accuracy were maintained in compared to the detections conducted in PBS. The concept of the stealth surface modification of SERS substrates could be adopted as a general strategy to introduce new functionalities to SERS substrates, while avoiding competition between the SERS signals of the target analyte and the surface modification.

4.5 Tables

Table 4.1 SERS vibrational frequencies for 4-MPBA and CBT

4-MPBA		CBT	
SERS (cm^{-1})	**Assignments[a]**	**SERS (cm^{-1})**	**Assignments[a]**
420	7a; $\beta_{CCC} + \nu_{CS}$	455	γ_{NC}
473	16b; $\gamma_{CCC} + \beta_{OBO}$	520	Si
614	6b; $\beta_{CCC} + \beta_{OBO}$	672	ν_{CS}
694	6a; $\beta_{CCC} + \nu_{CS}$	756	ν_{C4N}^{+}
728	4b; γ_{CCC}	847	β_{CSAu}
754	11; γ_{CH}	891	$\nu_{CCOO}^{-} + \nu_{CC}$
1000	12; β_{CCC}	935	β_{HCH}
1024	18a; β_{CH}	1079	ν_{C4N}^{+}
1065	ν_{CS}	1132	β_{CH3}
1075	1; β_{CCC}	1246	γ_{CH2}
1187	9a; $\beta_{CH} + \beta_{BOH}$	1365	ν_{COO}^{-}
1283	3; $\beta_{CH} + \beta_{BOH}$	1448	γ_{CH3}
1472[b]	19b; ν_{CC}	1585	ν_{COO}^{-}
1487	19a; ν_{CC}		
1574[b]	8b; ν_{CC}		
1587	8a; ν_{CC}		

[a] ν; stretching, β; in plane bending, γ; out of plane bending

[b] 8b and 19b nontotally symmetric ring-stretching vibrational modes increase while 8a and 19a totally symmetric ring-stretching vibrational modes decrease in SERS spectra of 4-MPBA after fructose binding due to Herzberg-Teller contributions.

4.6 Figures

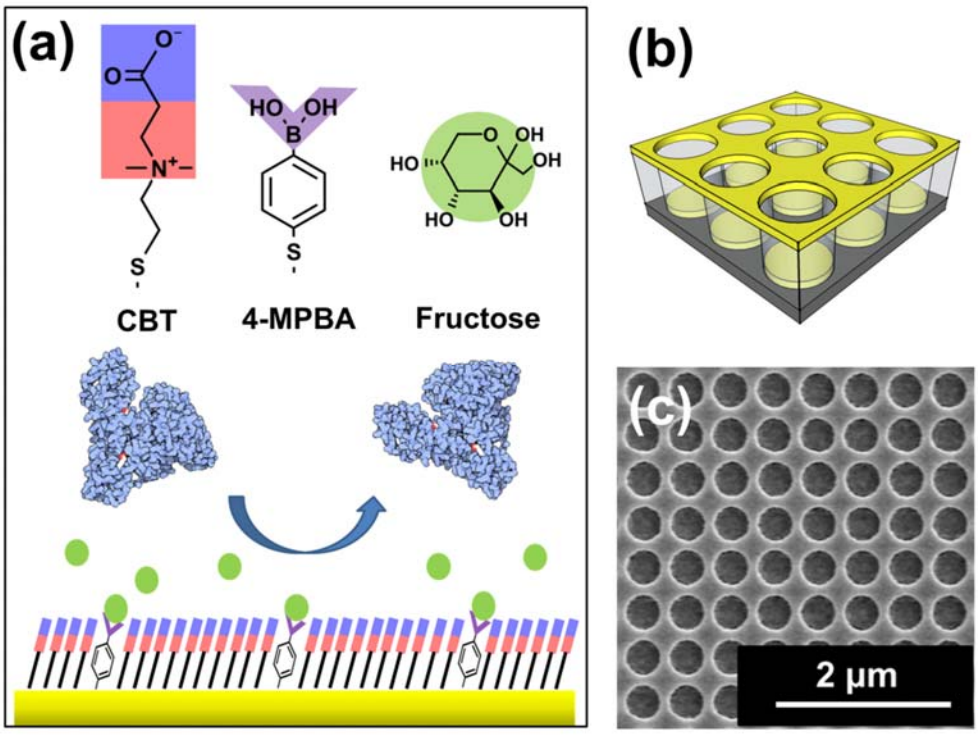

Figure 4.1 Schematic illustration of mixed SAM of 4-MPBA and CBT on a gold Q3D-PNA SERS-active surface for fructose detection

(a) Schematic illustration of mixed SAM of 4-MPBA and CBT on a gold Q3D-PNA SERS-active surface for fructose detection with the presence of proteins. (b) A 3D illustration of the Q3D-PNA composed of a separated gold thin film with nanoholes on top and gold nanodisks at the bottom of wells. (c) The top-view SEM image of a Q3D-PNA showing the diameter of ~400 nm.

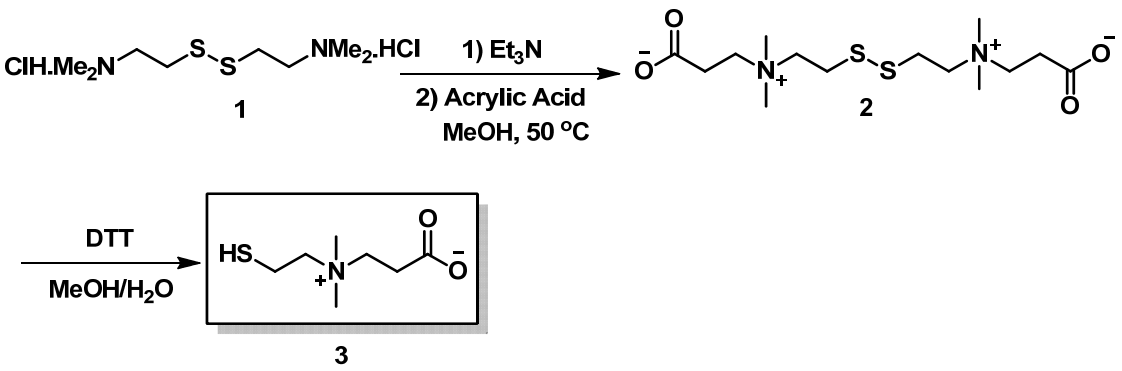

Figure 4.2 Scheme of the reaction route for the synthesis of CBT

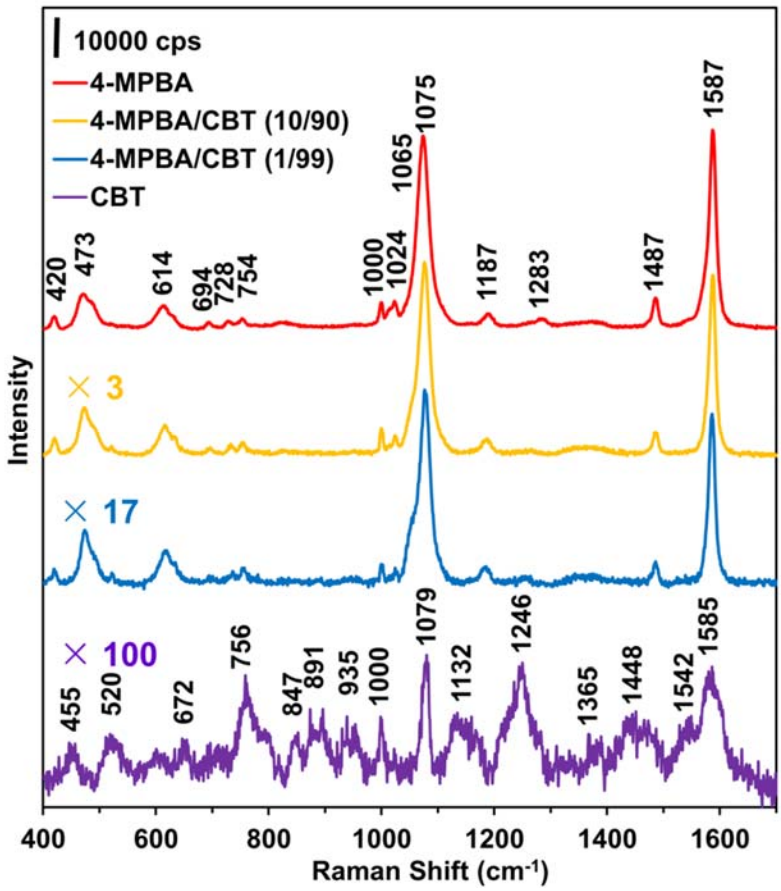

Figure 4.3 SERS spectra of pure 4-MPBA, 4-MPBA/CBT mixed SAMs and pure CBT on Q3D-PNAs in PBS

The mixed SAMs were formed with molar ratios 10/90 and 1/99 for 4-MPBA/CBT bulk solutions. The λ_{ex} = 785 nm, P_{laser} = 1 mW, and t = 10 s.

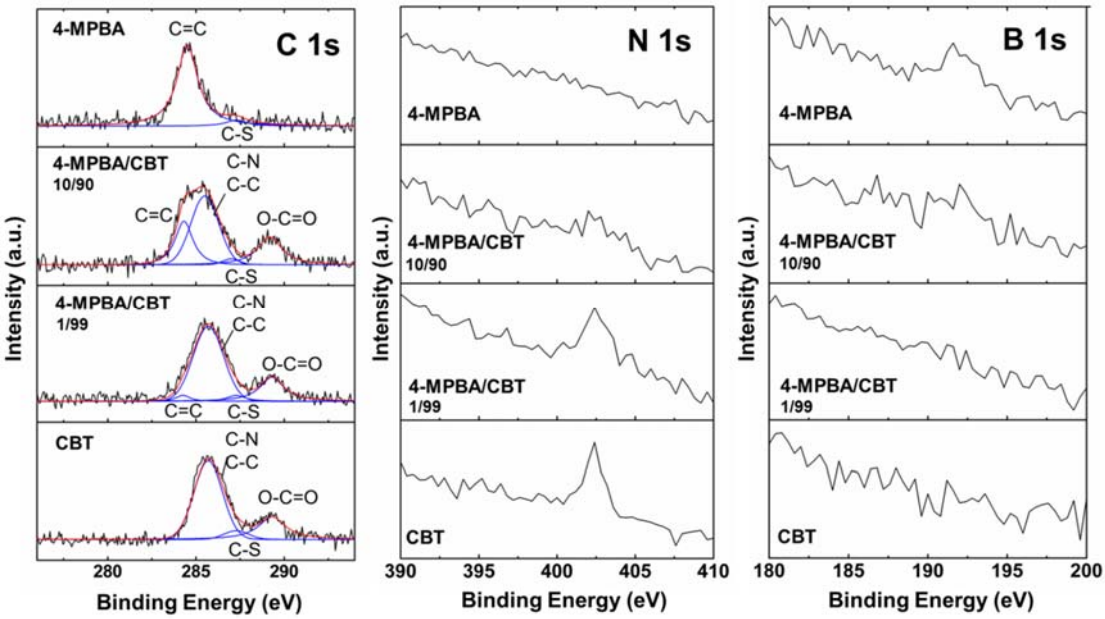

Figure 4.4 XPS studies

The XPS high-resolution C1s, detailed N 1s and B 1s spectra of pure 4-MPBA SAM, 4-MPBA/CBT (10/90 and 1/99) mixed SAMs and pure CBT SAM formed on gold surfaces.

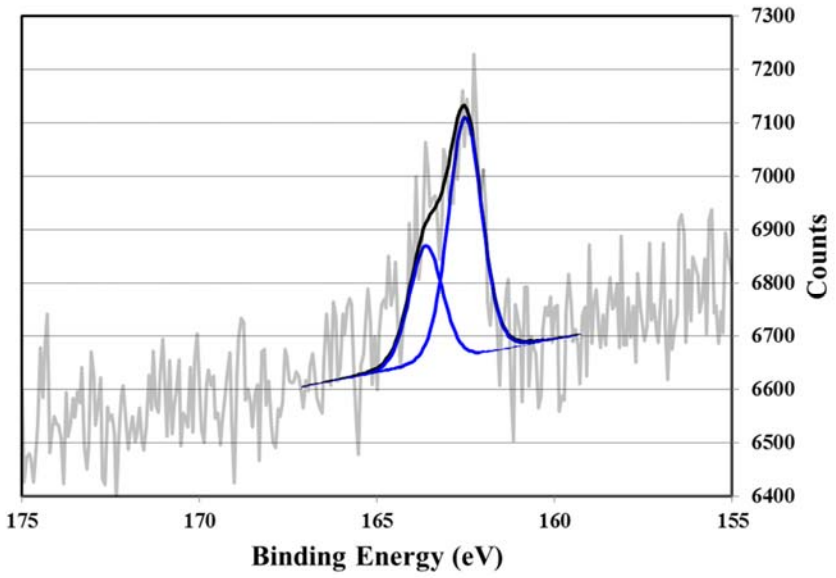

Figure 4.5 High-resolution XPS spectrum of the S 2p region of pure CBT SAM

The peaks were fit using S $2p_{3/2}$ and $2p_{1/2}$ with a 2:1 area ratio and a splitting of 1.2 eV. Only the binding energy of S $2p_{3/2}$ at 162.0 eV for the surface bounded sulfur was obtained, indicating that a good CBT SAM was formed.

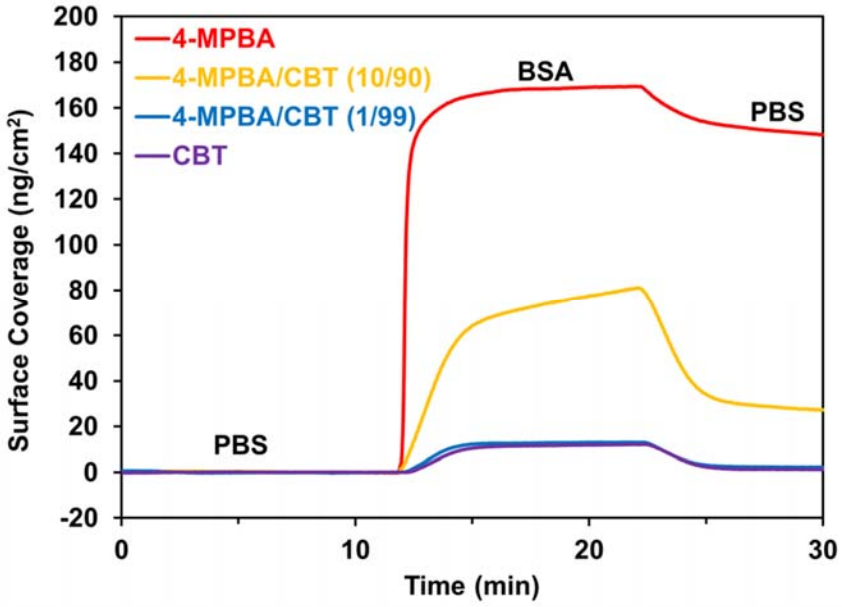

Figure 4.6 SPR tests of the mixed SAMs

Typical SPR sensorgram of pure 4-MPBA SAM, 4-MPBA/CBT (10/90 and 1/99) mixed SAMs and pure CBT SAM on gold surfaces when exposed to 1mg/mL bovine serum albumin (BSA) solution.

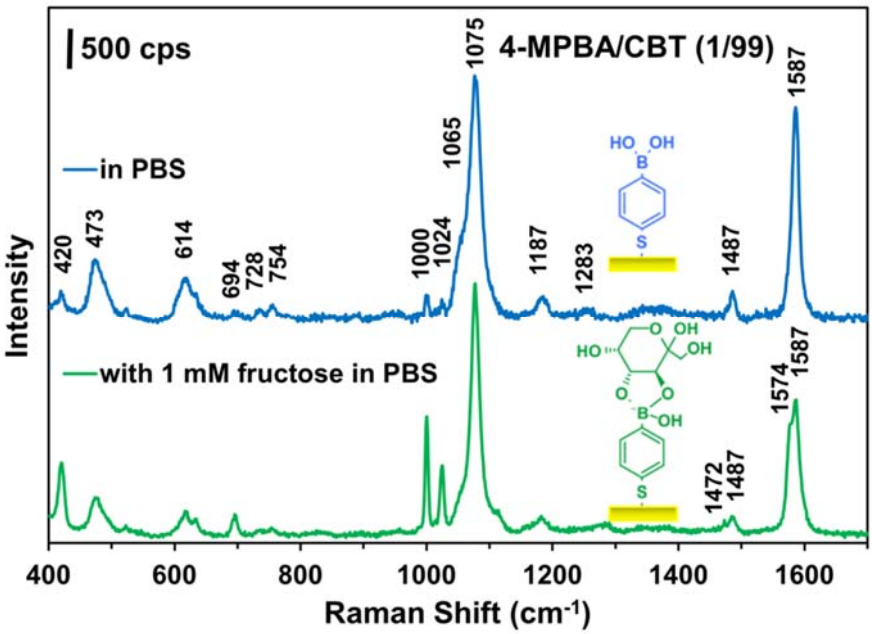

Figure 4.7 Fructose detection with the mixed SAM

SERS spectra of 4-MPBA/CBT (1/99) mixed SAM on a Q3D-PNA in PBS (blue) and in PBS with 1 mM of fructose taken after 1 h of immersion (green). The inset illustration shows the symmetry breaking of 4-MPBA upon fructose binding. The λ_{ex} = 785 nm, P_{laser} = 1 mW, and t = 10 s.

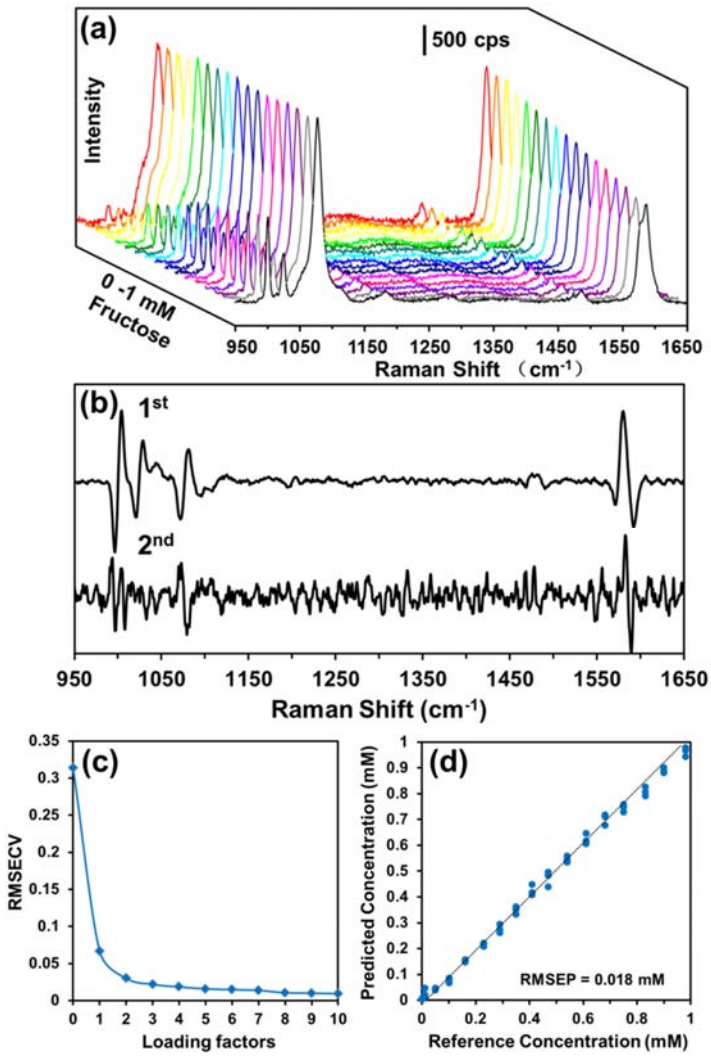

Figure 4.8 PLS analysis

(a) SERS spectra of 4-MPBA/CBT (1/99) mixed SAM in fructose PBS solutions with the fructose concentrations of 0.01-1 mM after immersion for 20 min. The λ_{ex} = 785 nm, P_{laser} = 1 mW, and t = 10 s. (b) First two calibration factors used to produce PLS predictions. (c) The root mean squared error of cross-validation (RMSECV) as a function of number of loading factors used in the PLS algorithm. (d) Plot of PLS predicted fructose concentrations *versus* reference fructose concentrations using 4 loading factors.

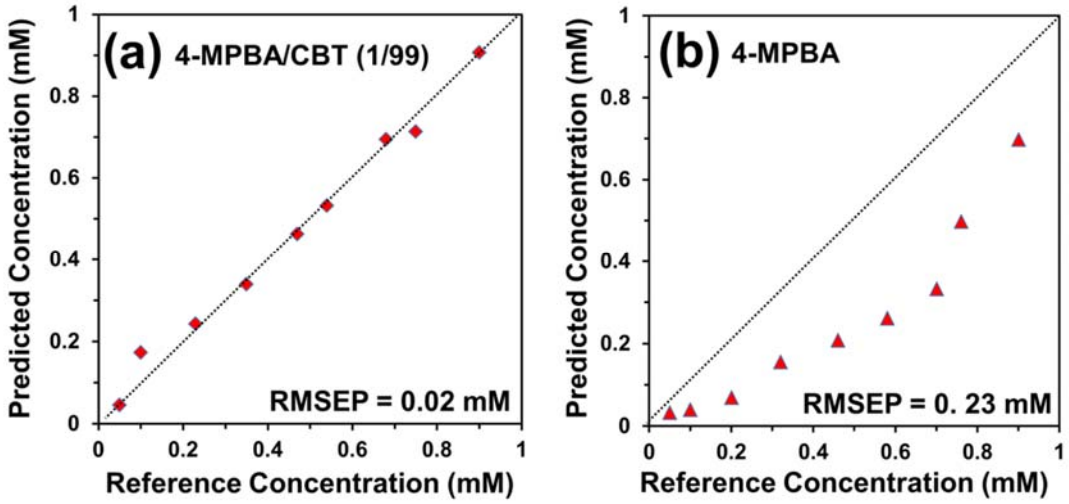

Figure 4.9 Detection in BSA solutions

(a) and (b) The plots of predicted fructose concentrations *versus* reference fructose concentrations on a 4-MPBA/CBT (1/99) mixed SAM and a pure 4-MPBA SAM modified SERS substrates, respectively, after immersed in the solution of 1 mg/mL BSA in PBS.

Chapter 5 Hierarchical Zwitterionic Modification of a SERS Substrate Enables Real-Time Drug Monitoring in Blood Plasma

In this chapter, we mainly discuss the surface enhanced Raman scattering (SERS) applications in real-world complex media such as undiluted human blood plasma. First, we reveal that the unmodified bare SERS sensors cannot survive in the blood plasma due to the nonspecific adsorption. To overcome this problem, we modify the SERS surface with zwitterionic polymer brush poly(carboxybetaine acrylamide) (pCBAA), a state-of-art nonfouling coating. The pCBAA is coated on the SERS-active surface via surface-initiated atom transfer radical polymerization (SI-ATRP), rendering the coating with high packing density showing undetected protein adsorption from the undiluted blood plasma thus protecting the SERS-active surface. Several drug molecules with strong Raman activity are directly detected by the pCBAA-coated SERS optofluidic system through the partitioning process demonstrating the potential of this technique to be used for real-time therapeutic drug monitoring.

5.1 Introduction

Blood plasma and serum hold the most valuable biochemical information for clinical diagnostics, but remain notoriously difficult to analyze without extensive processing. Rapid or real-time analyte detection in blood is particularly critical to therapeutic drug monitoring (TDM), which quantitatively measures the blood concentration of medications with a narrow therapeutic range [110]. TDM is currently a logistically complex and expensive process, and techniques to accurately monitor plasma drug concentrations in real time could dramatically simplify TDM and expand its reach.

Surface-enhanced Raman scattering (SERS) is one of the most sensitive spectroscopic techniques available, and this ultrasensitivity combined with its label-free molecular specificity promise to make SERS a prominent player in next-generation diagnostics [7, 86, 111]. SERS can be adapted to a wide range of detection targets, from small organic biomolecules and drugs to proteins, nucleic acids, cells and microorganisms [8, 11, 14]. Therapeutic drugs are typically excellent candidates for SERS detection, as ~95% of marketed drugs contain a conjugated ring system (such as a benzene ring)[112], which tend to produce the relatively large Raman scattering cross sections necessary for high sensitivity. To date, several drugs have been directly identified in saliva and urine using SERS, but blood samples require separation and chromatographic purification before SERS detection [113-116]. The Raman scattering enhancement seen in SERS decreases sharply when analytes are too far from a SERS-active surface [47, 75]. In blood, the wide assortment of small molecules (e.g. metabolites, carbohydrates, lipids and nucleotides) and plasma proteins compete with target analytes to bind the metallic SERS substrate [117, 118]. This competing adsorption, known as fouling, blocks analytes from reaching SERS-active substrate “hot spots” and generates substantial background noise, strongly reducing assay sensitivity and specificity. Analytes with weak affinity to SERS substrates or with small intrinsic Raman cross sections present further difficulties. To solve the apparently contradictory challenges of resisting nonspecific fouling while permitting or even promoting the diffusion of target analytes to SERS-active substrates, creative new surface chemistry modification approaches are necessary.

Here, we present such an approach by functionalizing the SERS optofluidic system (shown in **Figure 5.1a**) with a hierarchical zwitterionic modification. This modification contains two layers: a self-assembled monolayer (SAM) of "attracting" or "probing" functional thiols closest to the SERS-active substrate to physically attract analytes with weak surface affinity or chemically amplify the signals of analytes with small Raman activity, and a second layer of nonfouling zwitterionic poly(carboxybetaine acrylamide) (pCBAA) grafted via surface-initiated atom transfer radical polymerization (SI-ATRP) to protect the "hot spots" from the barrage of proteins in whole blood plasma that would typically limit detection sensitivity (**Figure 5.1b**). We used this system to quantify the dynamic concentration of anticancer drug doxorubicin (DOX) in undiluted human blood plasma, and demonstrated continuous real-time monitoring of the free DOX concentration with high sensitivity and accuracy alongside a rapid response time. The hierarchical modification also enabled detection of several TDM-requiring drugs as well as blood fructose and pH. As this surface chemistry is widely applicable to many analytes, this strategy provides a generalized platform for real-world SERS-based biosensing directly and continuously in complex media.

5.2 Experimental Section

5.2.1 Materials

Rhodamine 6G (R6G, 99%), doxorubicin hydrochloride (DOX, 98.0-102.0%), amitriptyline hydrochloride (AH, pharmaceutical secondary standard), carbamazepine (CARB, pharmaceutical secondary standard), phenytoin (PHEN, pharmaceutical secondary standard), 3-mercaptopropionic acid (3MA, ≥99%), 1-propanethiol (C3, 99%), 1-undecanethiol (C11, 98%), 4-mercaptobenzoic acid (4-MBA, 99%), 4-

mercaptophenylboronic acid (4-MPBA, 90%), D-(−)-fructose (≥99%), phosphate buffered saline packet (PBS, pH 7.4 and ionic strength 150 mM), copper(I) bromide (CuBr, 99.999%), copper(II) bromide ($CuBr_2$, 99.999%), 1,1,4,7,10,10-hexamethyltriethylenetetramine (HMTETA, 97%) were purchased from Sigma-Aldrich (St. Louis, MO). The OEG-terminated thiol ($HS(CH_2)_{11}(OCH_2)_4OH$) was purchased from ProChimia (Poland). The doxorubicinol hydrochloride (DOXol, ≥90%) was purchased from Toronto Research Chemicals (Canada). Ethanol (200 Proof) was purchased from Decon Laboratories (King of Prussia, PA). Pooled human plasma (in sodium heparin, mixed gender) was purchased from Biochemed Services (Winchester, VA). High-purity deionized (DI) water was obtained with a Millipore water purification system with a minimum resistivity of 18.2 MΩ cm.

5.2.2 Fabrication of SERS substrates and integration of the optofluidic system

Quasi-3D gold plasmonic nanostructure arrays (Q3D-PNAs) SERS substrates [41] with high sensitivity and reproducibility were used in this work. The SERS substrates are composed of physically separated gold thin films with subwavelength nanoholes on the top and gold nanodiscs at the bottom as illustrated in **Figure 5.1a**. They were fabricated via electron beam lithography (EBL) following the same procedure reported previously [95]. On a 4-inch wafer, 70 pieces of SERS substrates, each with 4 of 50 μm x 50 μm Q3D-PNAs, were made to ensure high reproducibility from pattern to pattern and substrate to substrate. Ellipsometery (J.A. Woollam, α-SE) was used to measure the thickness of poly(methyl methacrylate) (PMMA) and gold coatings. The dimensions of the Q3D-PNA were characterized using scanning electron microscopy (SEM, FEI Sirion).

The substrate was attached to a custom-made Teflon flow cell (1.2 cm × 1.2 cm × 1.5 mm) sealed with a glass cover. A peristaltic pump was used to deliver liquid samples.

5.2.3 Preparation of hierarchical pCBAA films on SERS substrates or SPR chips

The SI-ATRP initiator, mercaptoundecyl bromoisobutyrate and carboxybetaine acrylamide (CBAA) monomer were synthesized as described previously [119]. SAMs of the ATRP initiator on UV-ozone cleaned SERS substrates and SPR chips were formed by soaking bare substrates or chips overnight in 1 mM initiator solution in pure ethanol. Upon removal, the chips were rinsed with ethanol, DI water, ethanol, and then dried and placed in a custom glass tube reactor under nitrogen atmosphere. CuBr (7.17 mg) and $CuBr_2$ (2.79 mg) along with a stir bar were placed in separate small test tubes, and 182.64 mg of CBAA monomer and a stir bar were placed in a large test tube. All three test tubes were sealed with a rubber septum and deoxygenated by eight repetitions of a strong vacuum followed by nitrogen back fill. Afterward, 4 mL and 2 mL of deoxygenated water was added to the CBAA monomer and copper catalyst tubes, respectively. While stirring, 30 μL of HMTETA was added to the copper catalyst solution and stirred for 30 min for ligand complexation. Then, 160 μL of the copper catalyst solution was transferred to the 4 mL CBAA monomer solution. After stirring for five minutes, the entire CBAA monomer solution was transferred to the SERS or SPR chips contained in a tube reactor to initiate polymerization. Reaction time was 30 min, and a ~50 nm film (measured by ellipsometry) was successfully grown on SERS and SPR chips. The modified chips were rinsed with DI water and stored in PBS before SERS or SPR testing. The mixed SAMs were formed on the gold surface of SERS and SPR chips by immersing the chips in different compositions of 1 mM mixed thiols stock solutions in ethanol.

5.2.4 Measurement of protein adsorption using SPR sensor

A four-channel SPR sensor was applied to measure the nonspecific protein adsorption from human plasma on the surfaces of SPR chips modified with hierarchical pCBAA films. The temperature controller was set to 25 ± 0.01°C. Protein adsorption was measured by sequentially flowing PBS, 100% human plasma, and PBS over the modified surface each for 10 min at 40 μL/min flow rate by a peristaltic pump. The wavelength shift between the baselines before protein injection and after rinsing with PBS was used to quantify the total amount of protein adsorbed. A reference channel containing a PBS flow was used for each chip to correct for baseline drift. A 1 nm wavelength shift from the SPR at 750 nm represents a surface coverage of 17 ng/cm^2 adsorbed proteins.

5.2.5 Detection of drugs and small molecules using SERS optofluidic system

Raman spectroscopy was carried out on a Renishaw InVia Raman spectroscope connected to a Leica DMLM upright microscope. A 50×/N.A. = 0.8 objective was used to focus a 785 nm laser on Q3D-PNAs, and to collect the 180° scattered light from the sample surface. The laser power was set at 1 mW. A spectral resolution of 1.1 cm^{-1} was achieved and spectra ranging from 400 to 1800 cm^{-1} were collected with an exposure time of 10 or 30 s and one or three accumulations. The flow rate was 40 μL/min.

5.2.6 Study of OEG and C11 SAM modified SERS optofluidic systems

The OEG thiol ($HS(CH_2)_{11}(OCH_2)_4OH$) and 1-Undecanethiol ($HS(CH_2)_{10}CH_3$ C11 thiol) SAMs were formed on UV-ozone cleaned SERS substrates and SPR chips by soaking bare substrates or chips overnight in a 1 mM solution containing the corresponding thiol in pure ethanol. Using the same SERS optofluidic system used in other tests, four solutions were pumped over the OEG SAM or C11 SAM-modified SERS

substrates in succession: 1) saline buffer (PBS); 2) plasma; 3) PBS again; and 4) plasma spiked with 1 μM R6G. Each solution was circulated for 10 min, and SERS spectra were continuously collected. The nonspecific protein adsorption from undiluted plasma onto OEG and C11 SAMs were measured by an SPR sensor.

5.2.7 Determination of free DOX in plasma using ultrafiltration

A range of DOX concentrations (0.5, 1, 2, 4 and 8 μM) were investigated to determine the plasma binding parameters. Experiments for each concentration were run in triplicate and results were expressed as the mean ± standard deviation. To establish a standard curve, plasma ultrafiltrate (UF) control matrix was prepared from human plasma using an Amicon ultra-centrifugal filter device (10 kDa) centrifuged at 2000× g RCF for 30 min. UF calibration standards were prepared by adding 30 μL of working standards into 270 μL of control UF to provide final DOX concentrations in UF ranging from 0.2 to 4 μM; then, 90 μL of 1 ng/mL DOX was added as an internal standard (IS) to a 30 μL aliquot of each UF standard for analysis. Sciex 400Qtrap LC-MS/MS system with Turbo IonSpray (Applied Biosystems) operating in positive ion mode was adopted for compound detection. DOX working solution was mixed with human plasma for final concentrations from 0.5 to 8 μM (the same samples as those used for SERS detection). After 1 h incubation, 1 mL portions of human plasma solutions supplemented with various concentrations of DOX were placed in ultra-centrifugal filter, and ultrafiltrate containing free DOX was obtained by subjecting the system to centrifugation at 2000 × g RCF for 30 min. Analytical recovery of DOX in this system was about 95%. A 100 μL aliquot of the ultrafiltrate containing free DOX was subjected to LC-MS analysis and the concentration of free drug was determined based on the standard curve. The percentage

of free DOX in plasma was determined as follows: F/T × 100, where F denotes the free-drug concentration determined in the ultrafiltration and T is the total drug concentration.

5.2.8 Estimation of surface composition of mixed SAMs based on SERS spectral intensities

It is known that the final surface composition ratio of two components forming a SAM differs from their ratio in the SAM-forming bulk solution. We first estimated the surface ratio of initiator:3MA by taking the ratio of the absolute intensities of the 935 cm^{-1} peak, which is attributed solely to 3MA. We assumed equivalent total surface coverage of pure 3MA and initiator/3MA mixed SAMs, and that one initiator molecule provides surface coverage equivalent to one 3MA molecule on the SERS substrate. In this way, a change in the peak intensity at 935 cm^{-1} is directly attributed to a change in the number of 3MA molecules on the surface. On the basis of this assumption, we deduced that the initiator:3MA surface ratio in mixed SAMs was 92:8, corresponding to a molar ratio of 80:20 in the bulk solution. The higher fraction of initiator molecules in the SAMs may be due to stronger interactions between their longer alkane chains, which make initiator SAMs more stable than those formed from the short alkanethiol. Similarly, the surface ratio of initiator:C3 in mixed SAMs was 95:5, corresponding to a molar ratio of 90:10 in bulk solutions, based on the peak intensities at 892 cm^{-1}.

5.2.9 Estimation of surface composition of mixed SAMs based on ellipsometry film thicknesses

Surface compositions of mixed SAMs were also estimated from the film thicknesses measured by ellipsometry. The thicknesses of the single-component initiator SAM, 3MA SAM, and C3 SAM as well as the mixed initiator/3MA and initiator/C3

SAMs were determined using ellipsometry, (Model alpha-SE, J.A. Woollam, Lincoln, NE) in a 380–900 nm wavelength range at an incidence angle of 70°. The results were fitted to Cauchy model. Three locations on each sample were analyzed. To determine the molar ratio of initiator/short thiol (3MA or C3) on the surface, we assumed that the measured ellipsometric thickness of a mixed SAM, d_{mixed}, is directly related to the surface composition through the equation: $d_{\text{mixed}} = \chi_{\text{intiator}}\, d_{\text{initator}} + \chi_{\text{short thiol}}\, d_{\text{short thiol}}$, where χ_{intiator} and $\chi_{\text{short thiol}}$ are the mole fractions of initiator and short thiol in the mixed SAM, respectively, and $\chi_{\text{intiator}} + \chi_{\text{short thiol}} = 1$; d_{initator} and $d_{\text{short thiol}}$ are the thicknesses of single-component initiator SAM and short thiol SAM measured by ellipsometry, respectively. This assumption requires the refraction indices of pure and mixed SAMs to be the same.

5.2.10 Estimation of surface composition of mixed SAMs based on XPS analysis

The initiator/3MA and initiator/C3 mixed SAMs were additionally characterized using X-ray photoelectron spectroscopy (XPS) on an Axis Ultra XPS instrument (Kratos) using monochromated Al Kα radiation (1486.6 eV). Survey spectra and detail scans of Br 3p, S 2p, C 1s, O 1s and Au 4f were acquired using a pass energy of 150 eV. Spectra were collected with the analyzer at 55° with respect to the surface normal to the sample. Typical pressure in the chamber during spectral acquisition was 10^{-9} Torr. Three spots on two or more replicate samples were analyzed. Computer aided surface analysis (CasaXPS) software was used to calculate compositions from the peak areas. To determine the molar ratio of initiator/short thiol in the mixed SAM, we used the Br/S elemental ratio. In a single-component initiator SAM, the ideal Br/S elemental ratio is 1. In the mixed SAM, the Br/S ratio is diluted after mixing with the short thiol, which only contains elemental S

but no Br. The C/S ratio was also used to calculate the surface composition of initiator/short thiol in the mixed SAM.

5.3 Results and Discussion

5.3.1 The necessity of zwitterionic modification

Zwitterionic materials such as poly(carboxybetaine) (pCB) have been used for a wide range of medical and engineering applications [120-123]. These superhydrophilic polymers demonstrate exceptionally low fouling and high long-term stability in complex physiological fluids. To demonstrate the necessity of zwitterionic modification on a SERS substrate encountering complex media, we selected rhodamine 6G (R6G) as a model analyte; R6G is a widely-used dye with a large Raman cross section [52]. In this and all other experiments presented here, we used whole, undiluted human blood plasma. Using a SERS optofluidic system, four solutions were pumped over bare gold and pCBAA-modified SERS substrates in succession: 1) saline buffer (PBS); 2) plasma; 3) PBS again; and 4) plasma spiked with 1 μM R6G. Each solution was circulated for 10 min, and SERS spectra were continuously acquired. On the bare gold surface, spectra remained constant after 8 min of plasma exposure, and a representative spectrum is shown in **Figure 5.2a**. The SERS spectrum of plasma is complex and displayed several characteristic peaks similar to those found in previous reports [117, 124]; detailed assignments are summarized in **Table 5.1**. Notably, the spectrum remained unchanged when PBS was subsequently delivered (step 3) in an attempt to rinse the substrate (**Figure 5.2a**), suggesting that plasma proteins had fouled the bare gold surface and were difficult to remove. When we finally flowed R6G-spiked plasma over the substrate, the same spectrum still remained—despite the dye's large Raman scattering cross-section,

the previous fouling completely blocked its signals (**Figure 5.2a**). Comparatively, R6G at the same concentration exhibited extremely strong SERS signals on a clean, un-fouled SERS substrate.

The blue spectrum shown in **Figure 5.2b** is the baseline SERS signal of the pCBAA-modified surface in PBS. The spectrum is very similar to that of a 1-undecanethiol SAM, as most of the peaks come from the alkane-based ATRP initiators [24]. The signal from pCBAA itself is minimal, since pCBAA is an aliphatic polymer and is separated from the gold surface by about 2.2 nm. Peak assignments are listed in **Table 5.2**. In contrast to the rapid and irreversible spectral changes seen when an unmodified gold surface was exposed to plasma, SERS signals from the pCBAA-modified surface remained constant when switching from PBS to plasma (red spectrum in **Figure 5.2b**). This suggested that nonspecific adsorption was reduced to an undetectable level. Strong new signals appeared when we flowed R6G-spiked plasma over the surface (**Figure 5.2b**, green). When baseline peaks were subtracted, the final spectrum (**Figure 5.2b**, purple) clearly showed the characteristic R6G peaks.

The optofluidic system allowed us to monitor molecular adsorption onto the SERS-active surface in real time. We used the amide I vibrational band at 1649 cm^{-1} to track protein adsorption from plasma [125], and the C-C stretching band at 1508 cm^{-1} to monitor R6G. **Figure 5.2c** shows the intensity change of these peaks over time from alternating buffer and plasma solutions. To further quantify protein adsorption on bare and pCBAA-modified surfaces, we used an SPR biosensor. SPR sensorgrams revealed dense protein coverage on the bare surface (452 ng/cm^2) while only 0.3 ng/cm^2 was seen on the pCBAA-modified surface (**Figure 5.2d**). The heavy protein fouling from plasma

ruined the unmodified SERS sensor, while pCBAA modification effectively protected the SERS sensor.

Gold surfaces are often modified with oligo(ethylene glycol) (OEG)-based SAMs, which can effectively resist fouling from single protein solutions [126]. To compare the zwitterionic modification strategy reported here with OEG modification, we modified a SERS sensor with an OEG thiol ($HS(CH_2)_{11}(OCH_2)_4OH$) SAM and challenged it with human blood plasma. The OEG-modified sensor failed to detect the spiked R6G after flowing undiluted plasma (**Figure 5.3a**), and 111 ng/cm^2 of protein fouling was confirmed using an SPR sensor (**Figure 5.3c**). Both SERS and SPR results indicate that this short OEG SAM was insufficient to protect the SERS sensor from complex media. We conducted another comparison experiment by modifying the SERS substrate with a more hydrophobic SAM, 1-Undecanethiol ($HS(CH_2)_{10}CH_3$, C11 thiol). Again, no R6G could be detected after flowing plasma (**Figure 5.3b**), and even more protein fouling (263 ng/cm^2) was found on this C11 SAM-modified surface (**Figure 5.3c**).

5.3.2 Real-time quantitative monitoring of doxorubicin in undiluted human plasma

Continuous TDM can afford clinicians the opportunity to tailor therapeutic windows to individual patients, optimizing a drug's beneficial effects while minimizing side effects. Ferguson et al. developed a real-time drug tracking system based on unique aptamers that must be designed for each drug [127]. In comparison, SERS-based biosensing is label-free; if sensor fouling is mitigated, a SERS optofluidic system could be directly used for real-time TDM. We next aimed to use our pCBAA-modified SERS optofluidic platform to detect the popular chemotherapeutic agent doxorubicin (DOX) in plasma, as it exhibits significant pharmacokinetic variability [128]. DOX binds to plasma

proteins in the bloodstream, rendering the protein-bound DOX inactive. When this DOX-containing plasma is analyzed with a pCBAA-modified SERS sensor, we hypothesize that the polymer brush prevents these inactive DOX-protein complexes from reaching the SERS-active substrate—this enables measurement of only the active DOX concentration, which is of the most interest [129].

We added 20 μM DOX to plasma and flowed it through our pCBAA-modified detection system. The steady-state SERS spectrum was recorded (**Figure 5.4a**, purple), and the baseline plasma spectrum (**Figure 5.4a**, red) subtracted to derive the pure DOX spectrum (**Figure 5.4a**, blue), which matches those reported by other researchers [130]. Next, we recorded the SERS spectra of protein-free human plasma ultrafiltrate (UF) spiked with DOX over the clinically relevant concentration range of 0.05 – 10 μM; these subtracted DOX spectra are displayed in **Figure 5.4b**. As expected, the intensities of characteristic DOX peaks increased with concentration. The DOX peak at 442 cm^{-1} in the subtracted spectrum is attributed to C-C-O and C=O in-plane deformation. The 520 cm^{-1} peak in the raw spectrum arises from Si in the SERS substrate, and was used as an internal standard **Figure 5.5**. The relative magnitudes of peaks at 442 cm^{-1} (in the subtracted spectra) to 520 cm^{-1} (in the raw spectra) were selected to generate a detection curve illustrated in **Figure 5.4c**, with a linear dynamic range between 0.05 to 2 μM shown inset.

Reversibility is an important characteristic for a viable sensor, and determines the sensor response time to changes in analyte concentration. To test the reversibility of our pCBAA-modified SERS sensor, we injected DOX-spiked plasma (20 μM) at t = 0 and switched to pure plasma at t = 250 s. SERS spectra were continuously collected with a 30

s integration time, and the relative intensity of I_{442}/I_{520} over time was plotted (**Figure 5.4d**). Clearly, DOX detection is reversible with exponential response constants of 43 and 95 s for partitioning and departitioning, respectively. With requisite parameters in hand, we conducted a model TDM experiment. SERS spectra were collected over 3 hours as plasma flowed over the pCBAA-modified sensor; every 30 min, we alternated the inlet stream between pure and DOX-spiked plasma, the latter with DOX concentrations of 0.5, 1, 2, 4, and 8 μM. Based on the calibration curve generated in plasma UF, we plotted the DOX concentration detected in plasma (red points in **Figure 5.4e**) compared with each spiked concentration. Of particular interest, all measured concentrations were less than spiked concentrations, indicating only free DOX was detected while protein-DOX complexes were blocked by the pCBAA brush as hypothesized. This is an important advantage of this platform, and reinforces the importance of TDM to personalized dosing. Our results indicate that about 23-33% of DOX molecules added to plasma remain unbound to proteins (**Figure 5.6**) and thereby pharmacologically active. To corroborate this drug-protein binding ratio, we also ultrafiltered the plasma samples immediately after SERS detection and quantified the free DOX with liquid chromatography–mass spectrometry (LC-MS) (see Supporting Methods). Using this method, 34-37% of DOX was calculated to be unbound (**Figure 5.6**), and the LC-MS-quantified concentrations are also plotted in **Figure 5.4e** (purple dashed line). Results from both analytical methods are similar to those reported in medical literature (about 29%)[131]. In addition, we found our system able to distinguish DOX from its metabolite doxorubicinol (DOXol), which shows a new characteristic peak at 1340 cm^{-1} (**Figure 5.4f**). In these experiments, we flowed varying molar ratios of DOXol/DOX with a combined concentration of 2 μM and

collected SERS spectra (**Figure 5.4f**). The relative intensities of the 1340 cm^{-1} and 1407 cm^{-1} peaks illustrate a linear relationship as a function of DOXol/DOX ratio (**Figure 5.4g**), indicating a multiplex detection capacity. Overall, we demonstrated the TDM capability of a pCBAA-modified SERS-active substrate when combined with a microfluidic system, and successfully monitored the active level of DOX in plasma quantitatively and in real time.

5.3.3 Hierarchical zwitterionic modification incorporating "attracting" thiols

Both R6G and DOX were able to diffuse through the nonfouling pCBAA brush and penetrate or partition into the initiator SAM [132, 133]. However, some analytes are unable to partition into this SAM due to polar functional groups or low surface affinity, and thus are undetectable by a system simply modified with a pCBAA brush. We selected three drugs that match this description and are prime candidates for TDM—tricyclic antidepressant amitriptyline hydrochloride (AH) and anti-seizure medications carbamazepine (CARB), and phenytoin (PHEN) [134, 135].

To attract and concentrate these analytes closer to the SERS-active surface, we introduced shorter thiols with a functional terminal group mixed with the initiator forming the first layer. PCBAA brushes were then grafted from the initiator to form the second nonfouling layer. We selected 3-mercaptopropionic acid (3MA) and 1-propanethiol (C3) to form mixed SAMs with the initiator, to enable electrostatic and hydrophobic interactions with drug molecules, respectively. An optimized ratio of attracting (3MA or C3) to initiator thiols in the SAM was critical to maximize sensitivity while maintaining a sufficient initiator (and thus pCBAA) density to strongly repel proteins. We generated a library of SAM-coated gold chips with varied ratios, targeting

0%, 5%, 10%, 20%, 40%, or 100% of 3MA or C3 with the balance initiators. Then, we polymerized pCBAA brushes from each chip and evaluated fouling from undiluted plasma using an SPR sensor. Excellent nonfouling behavior (< 5 ng/cm^2 adsorbed proteins) was maintained when up to 20% of 3MA or 10% of C3 attracting thiols were incorporated (**Figure 5.7a, c**). The SERS spectrum resulting from the optimized mixed 3MA SAM (after pCBAA polymerization) is shown in **Figure 5.7b** (purple). As expected, it contains peaks similar to those observed from each modification alone (also shown in **Figure 5.7b**, with 3MA in red and initiator/pCBAA in blue). As 3MA has a larger Raman cross section than the ATRP initiator, it produces stronger SERS peaks. By comparing the absolute intensities of the 3MA peaks in mixed and pure SAMs, we determined the final incorporated surface content of 3MA was 8%, with 92% initiator. We repeated this process for the optimized C3-containing mixed SAM and found the final C3 content to be 5% with the balance initiator; relevant SERS spectra are shown in **Figure 5.7d**. X-ray photoelectron spectroscopy (XPS) and ellipsometry were further used to analyze the mixed SAMs, and both confirmed similar surface compositions as summarized in **Tables 5.3 and 5.4**.

After optimizing the hierarchical mixed SAM chemistries incorporating "attracting" molecules, we used these modified SERS substrates to analyze plasma spiked with 20 μM of one of the three selected drugs (AH, CARB, or PHEN) to evaluate their TDM potential. The hierarchical nonfouling surface containing 3MA (which is negatively charged) was applied to attract and detect positively charged AH and CARB, and the resulting SERS spectra are shown in **Figure 5.8a and b**, respectively. Owing to the combined benefits of nonfouling pCBAA and electrostatic attraction from the mixed

SAM, each of these drugs was clearly detected in undiluted plasma. Accordingly, **Figure 5.8c** shows the SERS spectrum of PHEN detected with the hierarchical surface containing C3. The hydrophobic pockets created by C3 in the mixed SAM base layer may enhance PHEN detection by promoting surface partitioning. We also explored the limits of detection (LOD) achieved by our system for each of these three drugs in PBS. As shown in **Figure 5.9a and b**, the LOD was found to be 0.5 μM for CARB and 1 μM for PHEN, far below their clinically relevant ranges (20 – 50 μM for CARB and 40 – 80 μM for PHEN) [136]. The LOD for AH was 0.05 μM (**Figure 5.9c**), which is at the high end of its typical therapeutic window (0.04 – 0.05 μM) [136]. This suggests our SERS system could be useful for monitoring AH toxicity and overdose. In general, by mixing different "attracting" molecules, this platform can be tailored to analytes with a broad range of physical and chemical properties.

5.3.4 Hierarchical zwitterionic modification incorporating "probing" reporters

Some analytes in blood have relatively small intrinsic Raman cross sections, making them difficult to detect with SERS directly. These include monosaccharides such as glucose and fructose, while protons or metal cations lack Raman activity completely [95, 137]. To detect these analytes indirectly, probe molecules or Raman reporters have been developed. These probes are immobilized on SERS-active substrates to produce a specific response upon interaction with corresponding analytes, and they can even amplify detection signals. Detecting small fluctuations in blood pH is one important application of SERS probes, as these changes can influence how drugs bind to plasma proteins and thus impact their pharmacologically active concentration [138]. Likewise, the detection of monosaccharides in undiluted plasma is important for metabolic studies

and diabetes treatment. Similar to our hierarchical chemistries incorporating “attracting” thiols into the SAM, we designed mixed SAMs containing “probing” thiols for these diagnostic applications.

We chose probe molecules 4-mercaptobenzoic acid (4MBA) and 4-mercaptophenylboronic acid (4MPBA) for these surface modifications to detect blood pH and fructose in plasma, respectively. As with the other hierarchical chemistries, we optimized the SAM ratios of each probe and initiators and found that 5% of 4MBA or 4MPBA along with 95% initiator produced the best combination of signal strength and nonfouling after pCBAA was grafted. **Figure 5.10a** shows the SERS spectra observed in response to plasma pH changes (from 6.8 to 7.4), using the hierarchically modified sensor incorporating 4MBA. Due to its extremely large Raman cross section, 4MBA was responsible for all SERS signals, even though it comprised only 5% of the mixed SAM. All spectra were normalized to the peak at 1080 cm^{-1} (ν1 mode of benzene ring). The peak at 1420 cm^{-1}, attributed to the symmetric COO^{-1} stretching mode (νCOO^{-1}), increased concurrently with pH due to the deprotonation of 4MBA carboxyl groups [139]. By tracking the intensity change of the 1420 cm^{-1} peak, we were able to achieve pH detection in plasma with 0.1 pH unit resolution. Diminished pH sensitivity has been previously reported for SERS sensors modified solely with 4MBA, even in simple protein solutions [97]—the nonfouling pCBAA hierarchical modification we demonstrate here comparatively achieves robust and reliable pH detection in undiluted plasma with the same Raman reporter.

In a similar fashion, we detected fructose in plasma using a hierarchical modification incorporating 4MPBA. The boronic acid head groups in 4MPBA can

specifically bind to fructose, which breaks the symmetry of the probe molecule and induces ring reorientation and corresponding spectral changes. Our group has previously investigated fructose detection with 4MPBA-modified SERS sensors, in which we used mixed SAMs containing 4MPBA and short zwitterionic thiols to monitor fructose in single protein solutions [140]. Presently, we demonstrate that fructose detection directly in plasma is possible using a hierarchical surface chemistry—the zwitterionic pCBAA brush is key to this advance, as it provides the best available protection from protein fouling. **Figure 5.10b** clearly shows the relative intensity change of the peaks at 1574 and 1586 cm^{-1} (attributed to the 8a and 8b modes of the 4MPBA benzene ring) as fructose binds to the boronic acid moiety and breaks the probe's symmetry. Plasma was supplemented with 5 mM fructose for this detection experiment.

5.4 Conclusions

In complex, real-world media like undiluted blood plasma, bare gold SERS sensors cannot survive. Nonspecific protein fouling rapidly and irreversibly blocks "hot spots" on SERS-active substrates, nullifying the label-free sensitivity. To overcome this problem, we have introduced a novel modification to SERS-active substrate surfaces: a zwitterionic pCBAA brush coating grafted via SI-ATRP and designed to resist blood protein adsorption and protect the SERS sensor. Using this pCBAA-modified SERS substrate and an integrated optofluidic system, we demonstrated rapid, reliable, and continuous doxorubicin monitoring in undiluted human plasma. We further tailored the surface chemistry of the first layer by forming mixed SAMs containing functional thiols alongside the initiators required for polymer grafting. The additional electrostatic or hydrophobic interactions provided by these functional thiols allowed the attraction and

detection of a typical antidepressant and two anticonvulsant drugs in undiluted plasma. Similarly, we used mixed SAMs featuring Raman reporter probes to further extend the detection applications of this nonfouling hierarchical platform. The incorporation of these probe molecules enables SERS detection of more challenging analytes in undiluted plasma—whether they have weak SERS activity such as fructose or even no Raman activity at all such as the protons defining blood pH. Altogether, these hierarchical chemistries unified by nonfouling pCBAA have the potential to establish SERS optofluidic systems for real-time therapeutic drug monitoring in undiluted blood. While the complexity and the cost of SERS sensor fabrication and surface modification need to be considered, we believe more simple and cost-effective processes will be developed with advances in nanotechnology and polymer chemistry. This hierarchical modification approach allows the first-layer functionality to be tuned for the best selectivity, while preserving the second zwitterionic polymer brush layer to effectively circumvent protein adsorption from complex media. This strategy could be widely adopted for a variety of biosensing applications.

5.5 Tables

Table 5.1 SERS vibrational frequencies for 100% human blood plasma

Peak position (cm^{-1})	Vibrational mode [a]	Assignments
482	ν(S-S)	L-Arginine
578		Ascorbic acid or cholesterol
631	β (C-C)	Uric acid
724	β(C-H)	Hypoxanthine or adenine
754	β(C-H)	Adenine
838	ν(C-C-O)	L-Serine
881	ν(C-C)	Uric acid
955	ν(C-C)	Hypoxanthine or adenine
1036	ν(C-N)	Uric acid
1138	ν(C-N)	Uric acid
1325	ν(C-H)	Nucleic acid bases
1360	β(CH_3)	Adenine
1445	β(CH_2)	Collagen, phospholipids
1580	β(C=C)	Phenylalanine
1649	ν(C=O)	Amide I

[a] ν; stretching, β; bending

Table 5.2 SERS vibrational frequencies for pCBAA modification

Peak position (cm^{-1})	Vibrational mode [a]
520	Si
638	$\nu(C\text{-}S)_G$
710	$\nu(C\text{-}S)_T$
764	$\beta(C\text{-}H)$
864	CH_2 rock
881	CH_3 rock
1066	$\nu(C\text{-}C)_T$
1112	$\nu(C\text{-}C)_T$
1244	$\nu(C\text{-}C)_t$
1441	$\beta(CH_2)$
1649	Amide I

[a] ν; stretching, β; bending

Table 5.3 Film thickness of pure and mixed SAMs measured by ellipsometry and the molar ratio of mixed SAMs estimated from the film thicknesses.

	Initiator (I)	3MA	C3	I/3MA (90/10)[a]	I/3MA (80/20)[a]	I/C3 (90/10)[a]	I/C3 (80/20)[a]
Thickness (Å)	22.4 ± 0.7	10.4 ± 0.5	9.3 ± 0.3	21.4 ± 0.3	21.0 ± 0.4	21.5 ± 0.2	20.4 ± 0.5
Surface Ratio[b]				92/8	89/11	93/7	85/15

[a]The molar ratio of initiator/short thiol in bulk solutions prepared to form mixed SAMs.
[b]The molar ratio of initiator/short thiol in mixed SAMs, calculated from the ellipsometric thicknesses.

Table 5.4 Elemental composition and surface ratio of mixed SAMs analyzed by XPS.

	Elemental Composition (%)					Surface Ratio	
	Br 3p	S 2p	C 1s	O 1s	Au 4f	Method [b]	Method [c]
I/3MA (80/20) [a]	2.4 ± 0.3	2.7 ± 0.2	38.4 ± 1.4	5.6 ± 0.3	50.9 ± 2.1	90/10	93/7
I/C3 (90/10) [a]	2.5 ± 0.2	2.7 ± 0.3	39.0 ± 2.2	5.1 ± 0.5	50.6 ± 1.7	93/7	95/5

[a]The molar ratio of initiator/short thiol in bulk solutions prepared for forming mixed SAMs.

[b]The ratio of initiator/short thiol in mixed SAMs, calculated based on the Br/S elemental ratio.

[c]The ratio of initiator/short thiol in mixed SAMs, calculated based on the C/S elemental ratio.

5.6 Figures

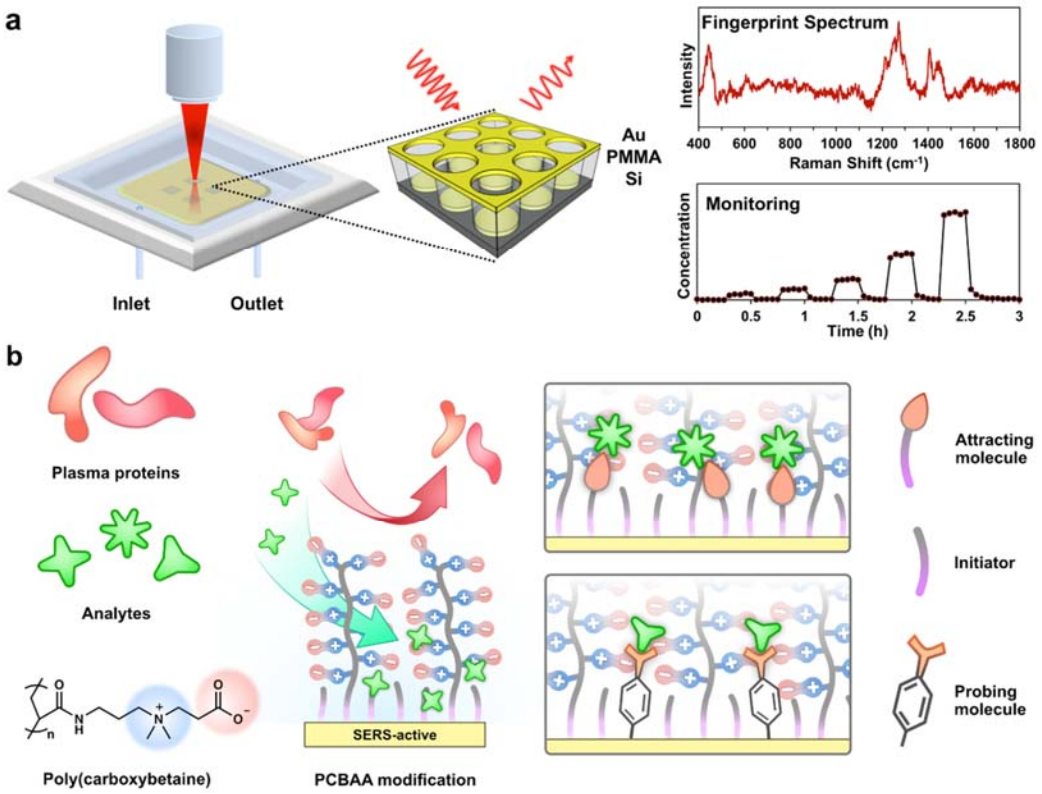

Figure 5.1 Schematic of Q3D-PNAs SERS optofluidic system and hierarchical zwitterionic surface modifications

a, Schematic of SERS optofluidic system incorporating a Q3D-PNAs SERS substrate to provide fingerprint spectra of analytes and quantitative, real-time monitoring. **b,** Schematic of hierarchical pCBAA-based zwitterionic nonfouling modification on the SERS-active surface. Top: Mixed SAM containing initiators and "attracting" molecules, which have terminal functional groups that physically attract analytes to the surface for direct SERS detection. Bottom: Mixed SAM containing initiators and "probing" molecules (Raman reporters), which have functional groups that chemically interact with analytes to facilitate indirect analyte detection by monitoring changes in the SERS spectra of the probes.

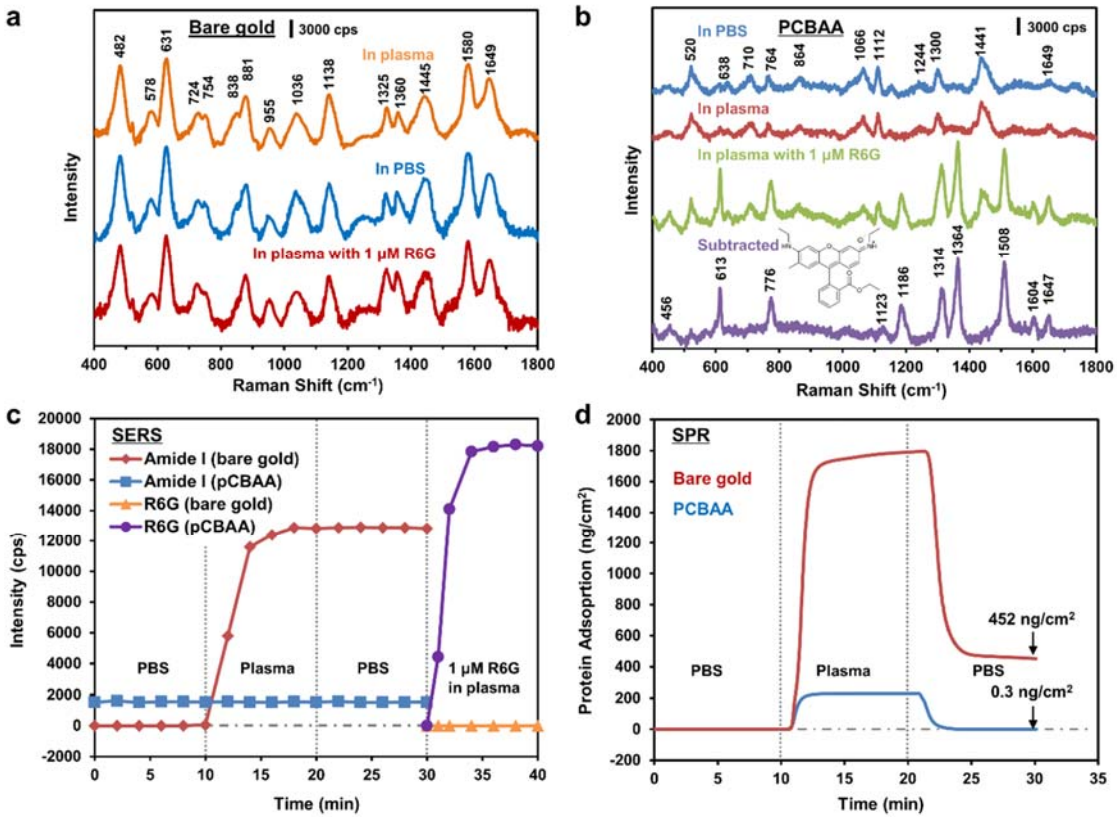

Figure 5.2 PCBAA surface modification enabling SERS detection in undiluted human blood plasma.

a, SERS spectra acquired with the unmodified SERS optofluidic system. From top to bottom, spectra shown were recorded after flowing undiluted plasma, PBS, and plasma spiked with 1 μM R6G each for 10 min. **b**, SERS spectra acquired with the pCBAA-modified SERS optofluidic system. From top to bottom, spectra shown were recorded after flowing PBS, undiluted plasma, and plasma containing 1 μM R6G each for 10 min, along with the subtracted spectrum from the last two. λ_{ex} = 785 nm, P_{laser} = 1 mW, and t = 30 s with 3 accumulations. **c**, Monitoring plasma protein adsorption and detecting R6G in plasma with the unmodified and pCBAA-modified SERS optofluidic system. Peak intensity of the amide I at 1649 cm^{-1} for protein and the C-C stretching at 1508 cm^{-1} for R6G were recorded as a function of time as PBS, plasma, PBS, and R6G-spiked plasma

were flowed sequentially. **d**, Typical SPR sensorgram of protein adsorption from undiluted plasma on a bare gold and pCBAA-modified gold surface, showing protein adsorption of 452 and 0.3 ng/cm^2, respectively.

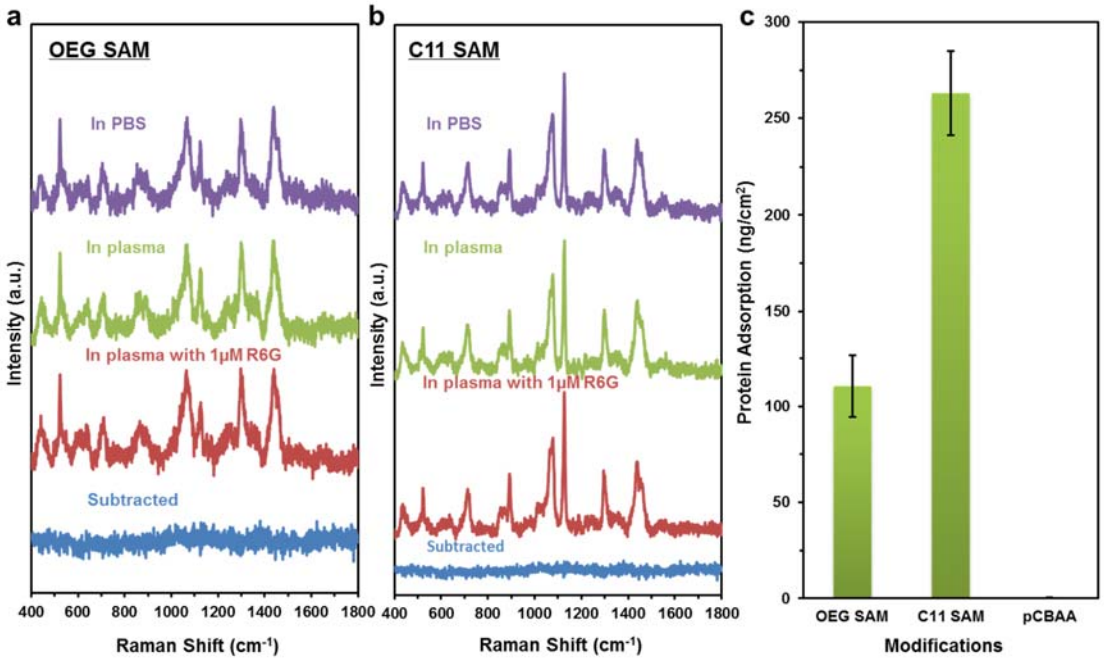

Figure 5.3 OEG SAM and C11 SAM modified SERS sensors challenged with undiluted human blood plasma

a,b, SERS spectra acquired with the OEG SAM-modified and C11 SAM-modified SERS optofluidic systems. From top to bottom, spectra shown were recorded after flowing PBS, undiluted plasma, and plasma containing 1 μM R6G each for 10 min, along with the subtracted spectrum from the last two. λ_{ex} = 785 nm, P_{laser} = 1 mW, and t = 30 s with 3 accumulations. **c**, Protein adsorption from undiluted plasma on OEG SAM and C11 SAM-modified gold surfaces, measured by an SPR biosensor. The error bar represent the standard deviation of three replicates.

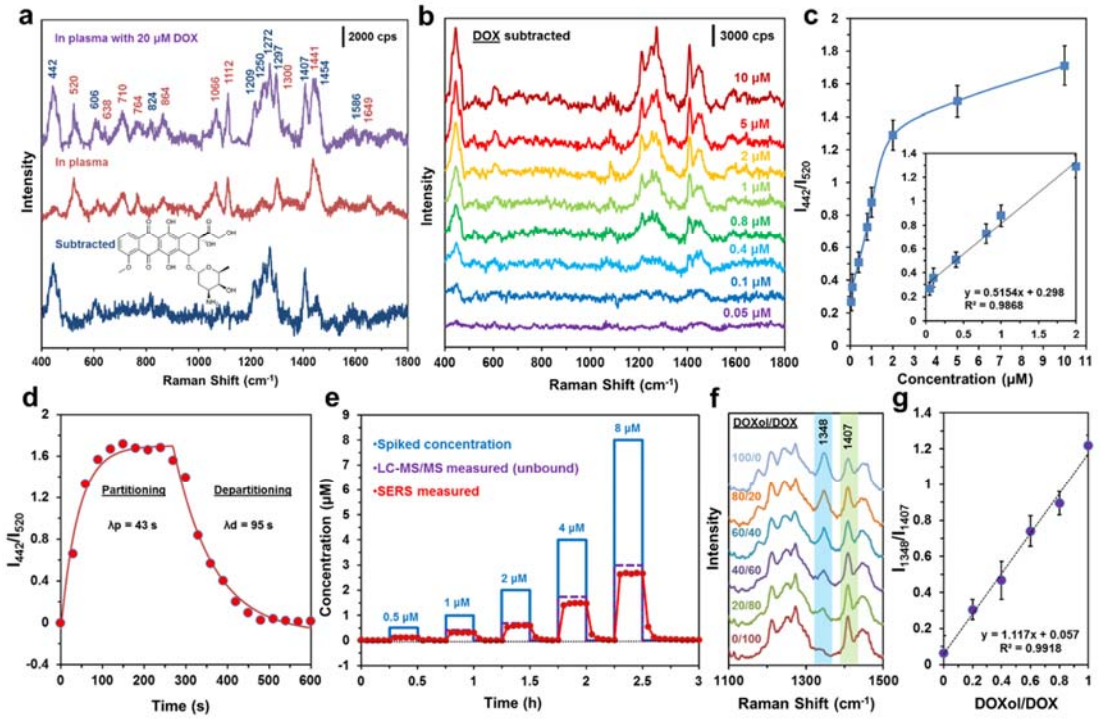

Figure 5.4 Real-time quantitative monitoring of doxorubicin in undiluted human plasma using the pCBAA-modified SERS optofluidic system

a, SERS spectra of undiluted plasma spiked with 20 μM DOX, plasma, and the subtracted spectrum . λ_{ex} = 785 nm, P_{laser} = 1 mW, and t = 30 s with 3 accumulations. **b,** Subtracted SERS spectra of DOX in plasma UF control at concentrations ranging from 0.05 to 10 μM. **c,** DOX detection curve generated by plotting the average intensity ratio of the peaks at 442 and 520 cm^{-1} as a function of the DOX concentration. Inset: a linear relationship was found for the physiologically relevant concentrations. The error bar stands for standard deviation of three replicates. **d,** Partitioning and departitioning of 20 μM DOX in plasma on a pCBAA-modified SERS-active surface. λ_{ex} = 785 nm, P_{laser} = 1 mW, and t = 10 s with 1 accumulation. The 1/e time constants were calculated to be 43 s for partitioning and 95 s for departitioning. **e,** *In vitro* real-time monitoring of DOX in undiluted human plasma (red) relative to spiked concentrations (blue) over the course of

3 h. The free DOX concentrations in plasma (red dots) were determined from the calibration curve in (c). The free DOX concentrations in ultrafiltrated plasma (purple dashed line) were measured using LC-MS. **f,** SERS spectra of pure DOXol and DOX and DOXol/DOX mixtures. **g,** Average intensity ratios of the peaks at 1349 and 1407 cm^{-1} as a function of the DOXol/DOX ratios. The error bar stands for standard deviation of three replicates.

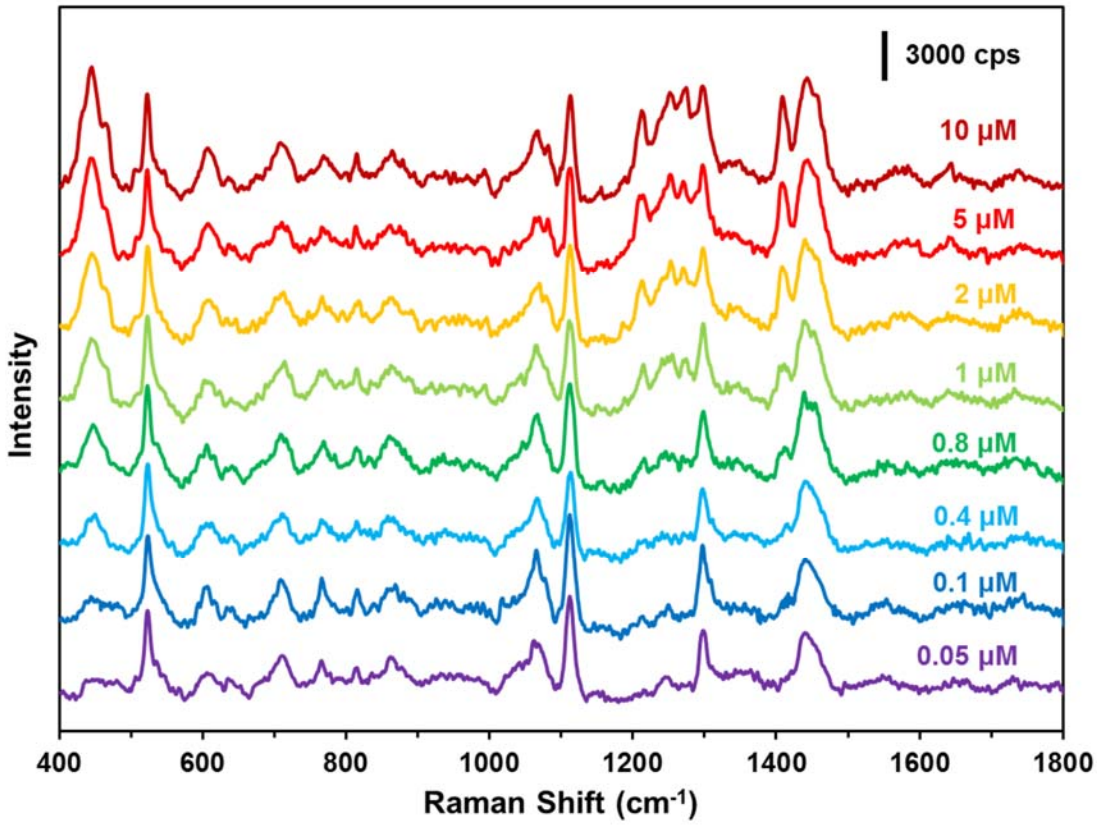

Figure 5.5 SERS spectra of DOX in plasma with different concentrations

SERS spectra of DOX in plasma UF control at concentrations ranging from 0.05 to 10 µM. λ_{ex} = 785 nm, P_{laser} = 1 mW, and t = 30 s with 3 accumulations.

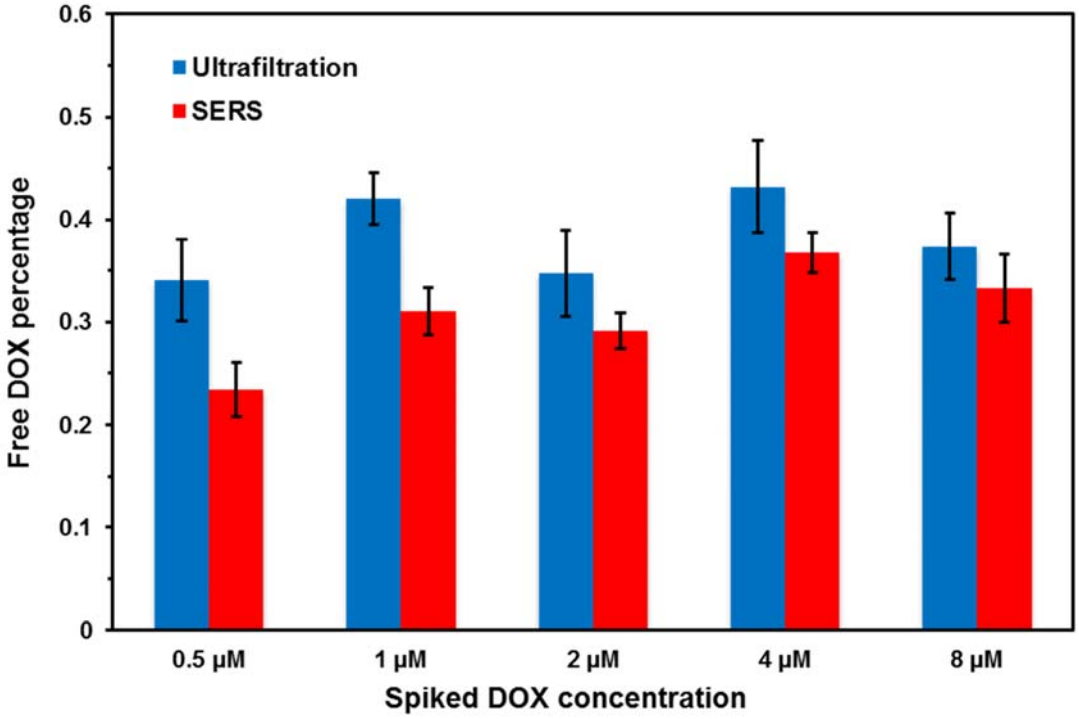

Figure 5.6 Free DOX percentages in plasma measured by ultrafiltration and SERS methods

Error bars represent the standard deviation of three replicates.

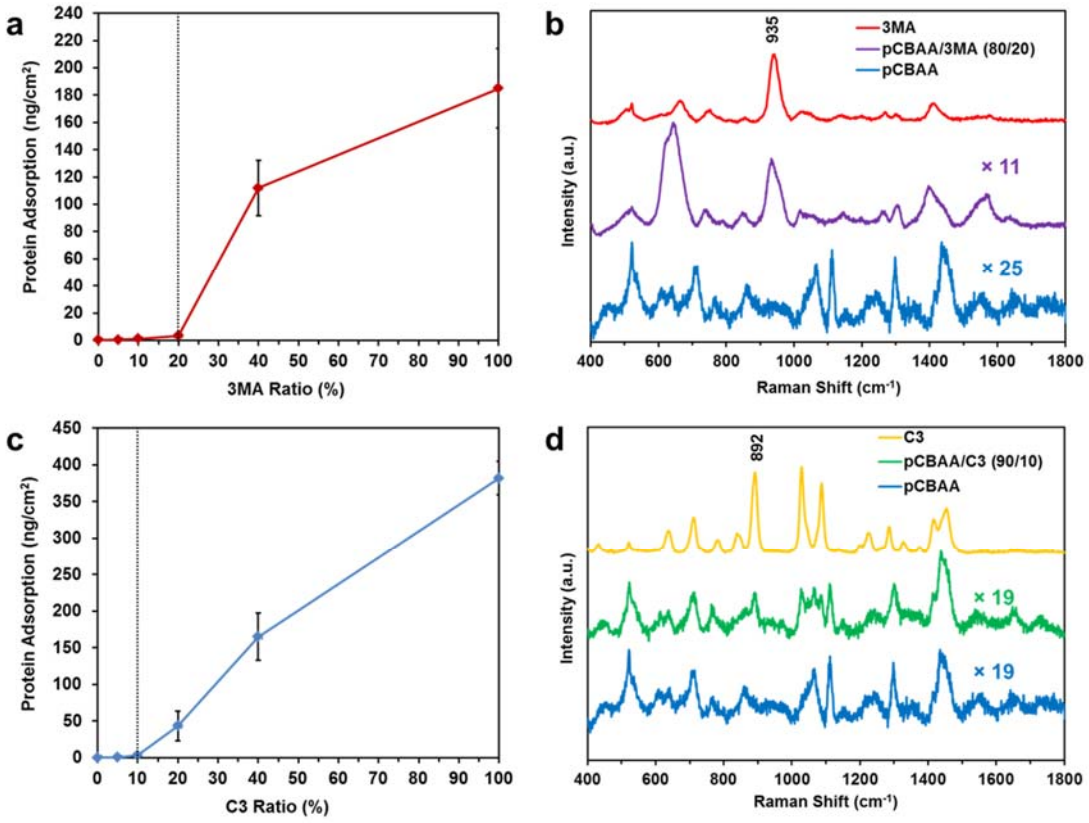

Figure 5.7 Optimizations of mixed SAM compositions

a, Protein adsorption from human blood plasma on hierarchical pCBAA modified gold surfaces as a function of 3MA ratio (in stock solution) measured by SPR, showing that the excellent nonfouling property (< 5 ng/cm^2) can be maintained down to an 80/20 initiator/3MA ratio in stock solution. **b,** SERS spectra of a pure 3MA SAM, a hierarchical pCBAA film with the SAM layer of initiator/3MA (80/20, in stock solution) and a pCBAA film grafted from a pure initiator SAM. Based on the absolute intensities of the peak at 935 cm^{-1} from the pure 3MA SAM (red line) and initiator/3MA mixed SAM (purple line), the ratio of initiator/3MA mixed SAM is 92/8 on the SERS surface. **c,** Protein adsorption from human blood plasma on hierarchical pCBAA modified gold surfaces as a function of C3 ratio (in stock solution) measured by SPR, showing that the

excellent nonfouling property (< 5 ng/cm^2) can be maintained down to a 90/10 initiator/C3 ratio in stock solution. **d,** SERS spectra of a pure C3 SAM, a hierarchical pCBAA film with an initiator/C3 SAM layer (90/10, in stock solution) and a pCBAA film grafted from a pure initiator SAM. Based on the absolute peak intensities at 892 cm^{-1} from the pure C3 SAM (yellow line) and initiator/C3 mixed SAM (green line), the ratio of initiator:C3 in the mixed SAM is 95/5 on the SERS surface. The error bars in a and c represent standard deviations of three replicates.

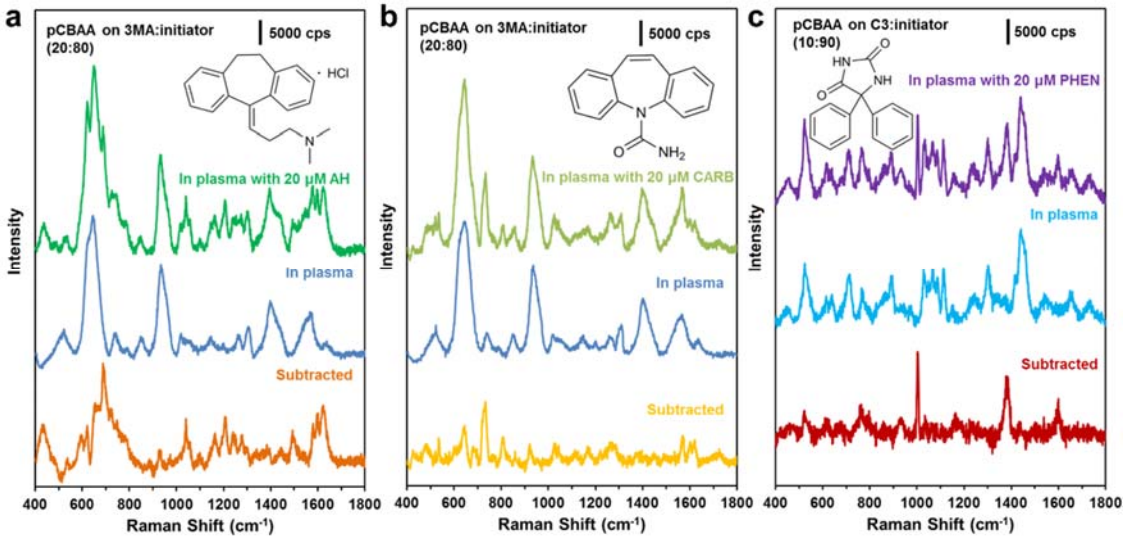

Figure 5.8 Hierarchical pCBAA surface modification to attract analytes and enable drug detection in undiluted human plasma

a, **b**, SERS spectra of 20 μM AH and 20 μM CARB spiked in undiluted plasma (green and olive), plasma (blue), and subtracted spectra (orange and yellow) acquired with the SERS optofluidic system hierarchically modified with pCBAA brushes grafted on the mixed SAM of 3MA and initiator (20:80). **c**, SERS spectra of 20 μM PHEN spiked in undiluted plasma, plasma, and subtracted spectrum acquired with the SERS optofluidic system hierarchically modified with pCBAA brushes grafted on the mixed SAM of C3 and initiator (10:90). λ_{ex} = 785 nm, P_{laser} = 1 mW, and t = 30 s with 3 accumulations.

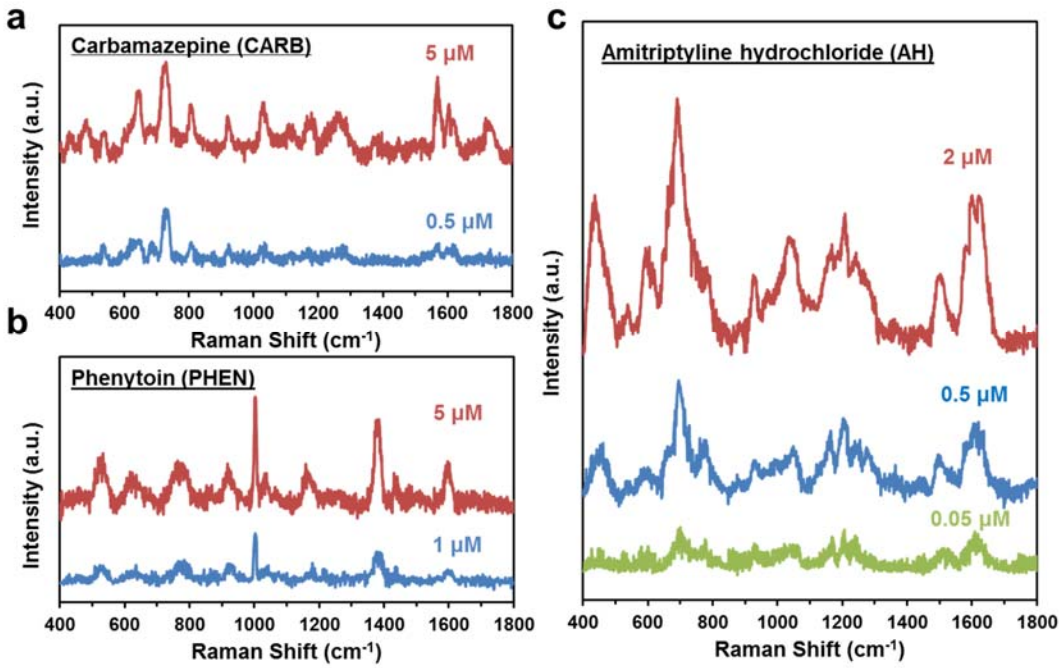

Figure 5.9 Limit of detection (LOD) experiments for CARB (a), PHEN (b) and AH (c), using the hierarchical pCBAA-modified SERS optofluidic system

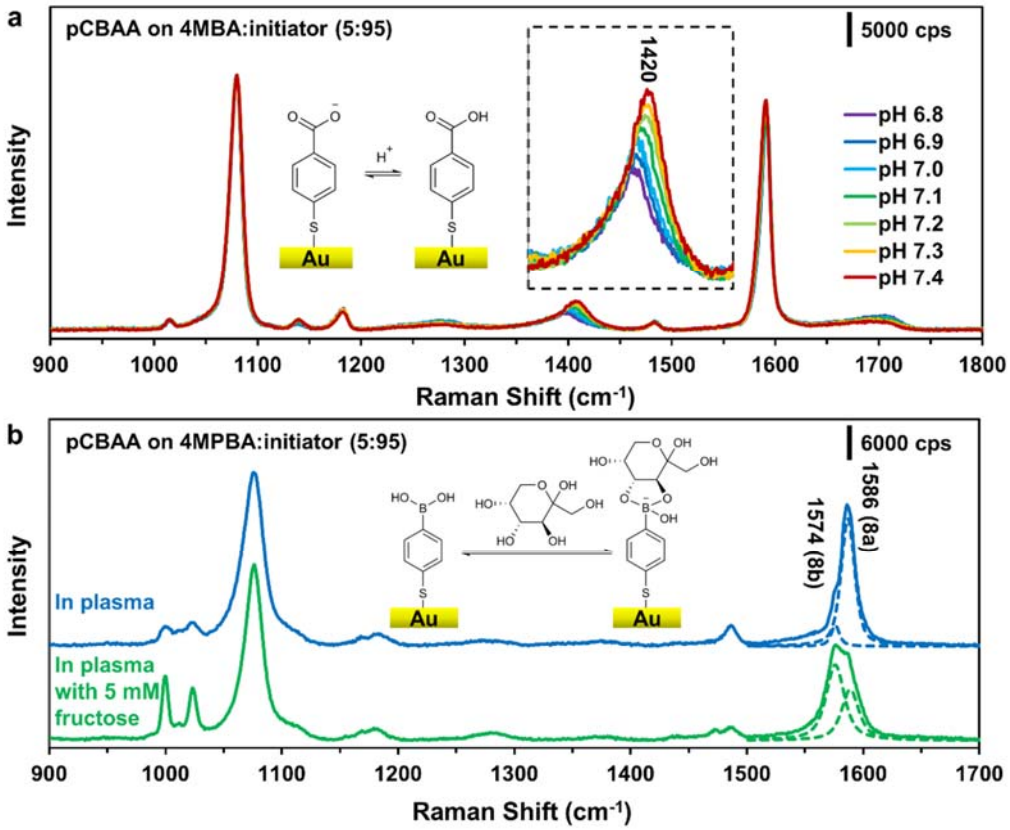

Figure 5.10 Hierarchical pCBAA surface modification with probing molecules to enable pH and fructose detection in undiluted human plasma

a, SERS spectra of 4MBA responding to pH-adjusted undiluted human plasma flowed over the hierarchically modified substrate with pCBAA grafted on the mixed SAM of 4MBA and initiator (5:95). **b**, SERS spectra of 4MPBA responding to undiluted human plasma and plasma spiked with 5 mM fructose, flowed over the hierarchically modified substrate with pCBAA grafted on the mixed SAM of 4MPBA and initiator (5:95). λ_{ex} = 785 nm, P_{laser} = 1 mW, and t = 30 s with a single accumulation.

Chapter 6 Ultra-Low Fouling and High Antibody Loading Zwitterionic Hydrogel Coatings for Sensing and Detection in Complex Media

For surface-based diagnostic devices to achieve reliable biomarker detection in complex media such as blood, preventing nonspecific protein adsorption and incorporating high loading of biorecognition elements are paramount. In this work, a novel method to produce nonfouling zwitterionic hydrogel coatings was developed to achieve these goals. Poly(carboxybetaine acrylamide) (pCBAA) hydrogel thin films (CBHTFs) prepared with a carboxybetaine diacrylamide crosslinker (CBAAX) were coated on gold and silicon dioxide surfaces via a simple spin coating process. The thickness of CBHTFs could be precisely controlled between 15 and 150 nm by varying the crosslinker concentration, and the films demonstrated excellent long-term stability. Protein adsorption from undiluted human blood serum onto the CBHTFs was measured with surface plasmon resonance (SPR). Hydrogel thin films greater than 20 nm exhibited ultra-low fouling (<5 ng/cm^2). In addition, the CBHTFs were capable of high antibody functionalization for specific biomarker detection without compromising their nonfouling performance. This strategy provides a facile method to modify SPR biosensor chips with an advanced nonfouling material, and can be potentially expanded to a variety of implantable medical devices and diagnostic biosensors.

6.1 Introduction

Avoiding nonspecific protein adsorption is critical in numerous fields. Biosensors, implanted medical devices, drug delivery systems and ship hulls all benefit tremendously from nonfouling surface chemistries [141-144]. Many materials have been reported to

reduce protein fouling, but key challenges remain. Although poly(ethylene glycol) (PEG) and its derivatives are the most widely used nonfouling materials, they are susceptible to oxidative damage over long-term use, difficult to directly functionalize with biomolecules for biosensing applications, and have limited nonfouling capabilities in complex, real-world media such as undiluted blood plasma and serum [145, 146]. Zwitterionic materials such as phosphorylcholine (PC), sulfobetaine (SB) and carboxybetaine (CB) are attractive alternatives and have seen increasing investigation [120, 140, 147-149]. Poly(carboxybetaine) materials, including poly(carboxybetaine methacrylate) (pCBMA) and poly(carboxybetaine acrylamide) (pCBAA), are particularly interesting. They exhibit ultra-low fouling properties (i.e., <5 ng/cm^2 of nonspecific protein binding) in 100% blood plasma and serum [150, 151]. In addition, abundant carboxylic acid groups make antibody functionalization to pCB straightforward via amino coupling chemistries [152]. These materials have proven useful for cancer diagnosis in whole blood [152, 153].

Typical methods of coating pCB on surfaces can be classified into two categories: “graft-from” and “graft-to”. In the “graft-from” approach, initiators are first immobilized on a substrate and a polymerization method such as atom transfer radical polymerization (ATRP) is used to grow polymer chains from the surface-bound initiators [120]. The “graft-to” method involves direct attachment of zwitterionic polymers—containing adhesive groups such as DOPA or thiols—onto the target surface [154, 155]. While the “graft-from” technique is an excellent strategy to achieve a high packing density and controlled film thickness, “graft-to” is a more convenient coating process. However, the “graft-from” ATRP often requires oxygen-free conditions while the “graft-to” surface-

adhesive polymers require extensive coating optimization. In addition, these quasi-2D coatings with high surface packing densities have limited space for subsequent protein immobilization [156]. Thus, new facile strategies to achieve nonfouling coatings with high protein loadings are highly desirable.

Hydrogel coatings are simple and convenient to attain, and several studies have examined their usage for protein resistance and biosensor functionalization [157-163]. The aforementioned PEG is regularly used to generate hydrogels for biomedical applications via photo-initiated crosslinking. Although PEG hydrogels resist protein adsorption, they fall short of achieving ultra-low protein adsorption from undiluted blood plasma or serum [164-166]. Polysaccharide-based materials such as dextran have also been reported to form hydrogel coatings on biosensors through a number of different methods, but these coatings could not stand with undiluted blood plasma or serum [167, 168]. A zwitterionic hydrogel film containing phosphorylcholine (PC) groups has been investigated for its swelling properties, but its tolerance to complex media has not been reported [169-171]. Fully zwitterionic hydrogels assembled from a CB monomer and a CB-based crosslinker exhibit many unique qualities—they have been demonstrated to resist nonspecific protein adsorption in undiluted whole blood [172], to prevent the foreign-body reaction to implanted materials [173], and to restrain the differentiation of mesenchymal stem cells [121]. In addition, the three-dimensional (3D) structure of the gel matrix provides many sites amenable to ligand immobilization for the specific detection of biomolecules. These virtues suggest that a pCB-based hydrogel coating may be up to the challenge of resisting protein fouling from complex, real-world media and providing abundant functional groups for the subsequent immobilization of molecular

bio-recognition elements while maintaining coating stability and simplicity. To the best of our knowledge, a simple hydrogel coating resisting nonspecific protein adsorption from undiluted blood serum has not been reported.

In this work, we develop a nonfouling, wholly zwitterionic coating based on a pCBAA hydrogel thin film (CBHTF). As shown in **Scheme 6.1**, a new zwitterionic CB-based diacrylamide crosslinker (CBAAX) was synthesized for this work. The hydrogel thin films were formed by spin-coating a stock solution containing monomer, crosslinker, and photoinitiator onto a hydrophilic, self-assembled monolayer (SAM)-modified gold surface, followed by ultraviolet (UV) light irradiation. The thicknesses of CBHTFs could be controlled by varying the crosslinker concentration, and the coatings displayed great stability. Optimized formulations of CBHTFs demonstrate ultra-low fouling (<5 ng/cm^2) from 100% human blood serum as measured by surface plasmon resonance (SPR), which has not been previously reported for a hydrogel coating. The CBHTF coating also performed well on a SiO_2-modified SPR sensor, indicating its capability for general use. CBHTF-coated SPR sensor chips could further be functionalized with antibodies for specific biomarker detection via the simple 1-ethyl-3-(3-dimethylaminopropyl)-carbodiimide/N-hydroxysuccinimide (EDC/NHS) coupling chemistry, which benefits from abundant carboxylic acid groups in the 3D CBHTF matrix. Antibody immobilization and biomarker detection levels were also optimized by controlling the crosslinking density.

6.2 Experimental Section

6.2.1 Materials

CBAA monomers were synthesized following a previously published method [123]. Acryloyl chloride, acetonitrile, tert-Butyl bromoacetate, dichloromethane (DCM), 2-Hydroxy-2-methylpropiophenone (HMPP), 11-Mercapto-1-undecanol ($C_{11}OH$), 1-Decanethiol (C_{11}), 12-Mercaptododecanoic acid ($C_{11}COOH$) and phosphate-buffered saline (PBS) were purchased from Sigma Aldrich (St. Louis, MO). 2,2'-Diamino-N-methyldiethylamine and N,N-Diisopropylethylamine (DIPEA), and trifluoroacetic acid (TFA) were purchased from TCI (Portland, OR). Ethanol was purchased from Decon Labs (King of Prussia, PA). Sodium acetate anhydrous was purchased from Fluka (subsidiary of Sigma Aldrich, St. Louis, MO). EDC and NHS were purchased from Acros Organics (Geel, Belgium). Pooled human serum was purchased from Biochemed Services (Winchester, VA). Human thyroid stimulating hormone (TSH) antibody and antigen were from Thermo Scientific (Waltham, MA). The buffers including 150 mM phosphate buffered saline (PBS) at pH 7.4, 10 mM sodium acetate buffer (SA) at pH 5, 10 mM boric acid (BA) with 300 mM NaCl at pH 9, 10 mM glycine (GLY) at pH 4 and 10 mM HEPES at pH 7.5 were prepared for biomolecular conjugation and bioassay. The pH values were adjusted with HCl or NaOH, and buffers were degassed prior to use. All water used was purified to 18.2 MΩ with a Millipore water purification system (Billerica, MA).

6.2.2 Synthesis of carboxybetaine diacrylamide crosslinker

A synthesis schematic of the CBAAX is shown in **Scheme 6.2**. A solution of acryloyl chloride (5.3 mL, 65.1 mmol) in 20 mL DCM was added dropwise to a solution

of 2,2'-Diamino-N-methyldiethylamine (4 mL, 31.0 mmol) and DIPEA (11,9 mL, 68.3 mmol) in 50 mL DCM at 0℃ over a 30 min period. The reaction mixture was allowed to warm to room temperature and stirred for two hours. The reaction was then washed with (2 x 25 mL) water. The aqueous layer was re-extracted with DCM (3 x 75 mL). The combined organic layers were dried using sodium sulfate, filtered, and concentrated in vacuo to leave a residue which was further purified by column chromatography to give compound **2** (5.2 gm) in 75.3% yield. ^{1}H NMR (300 MHz, D_2O) δ 6.02 – 5.97 (m, 4H), 5.56 – 5.51 (m, 2H), 3.14 (t, J = 6.7 Hz, 4H), 2.37 (t, J = 6.7 Hz, 4H), 2.07 (s, 3H).

Compound **2** (3.2 gm, 10.5 mmol) was dissolved in 20 mL acetonitrile and tert-butylbromoacetate (4.2 mL, 31.6 mmol) was added to it. The reaction contents were stirred for 18 hours at 65ºC until TLC showed complete consumption of the starting material. The reaction mixture was concentrated to dryness in vacuo and further purified by column chromatography to give compound **3** (4.3 gm) in 72.6% yield. ^{1}H NMR (300 MHz, DMSO-d_6) δ 6.31 – 6.08 (m, 4H), 5.67 (dd, J_1 = J_2 = 2.4 Hz, 2H), 4.48 (s, 2H), 3.75 – 3.54 (m, 8H), 3.29 (s, 3H), 1.45 (s, 9H).

Compound **3** (2.0 gm, 4.7 mmol) was dissolved in 15 mL DCM and 15 mL TFA was added. The reaction contents were stirred overnight at room temperature. After complete hydrolysis, the reaction mixture was concentrated in vacuo and co-evaporated with DCM (3 x 15 mL). The resulting residual mixture was further dissolved in 15 mL methanol and 4 mg IRN-78 resin was added to it for complete neutralization. The residue was dissolved in water and lyophilized to give compound **4** in 84.1% yield. ^{1}H NMR (300 MHz, DMSO-d_6) δ 6.31 – 6.05 (m, 4H), 5.63 (dd, J_1 = J_2 = 2.4 Hz, 2H), 3.70 (s, 2H), 3.69 – 3.50 (m, 8H), 3.21 (s, 3H).

6.2.3 Preparation of CB hydrogel solution and coating on SPR sensor chips

Monomer solutions were prepared in DI water, at a concentration of 9% by weight. The crosslinker CBAAX was added to these solutions in quantities ranging from 0.5 to 20% (molar percent of monomer). A 2.5% (molar percent of monomer) solution of photoinitiator HMPP was then added, and complete solutions were sonicated before spin-coating. The SPR sensor chips were produced by coating a glass slide with a 2 nm titanium film followed by a 50 nm gold film using an electron beam evaporator. The gold SPR chips were cleaned and modified with different SAMs by soaking the chips in ethanol solutions containing specified thiols (1 mM) overnight. The chips were then rinsed with DI water and ethanol and dried in a stream of filtered air. The prepared monomer solutions were spin-coated on the cleaned chips at 3000 rpm for 50 s. The spin-coated film was dried with filtered air and the chips were exposed to UV light (6 W; 302 nm with 280 nm cutoff filter) for 120 min to commence polymerization. After UV crosslinking, the hydrogel-coated substrates were immersed in PBS solution for 3 days to allow the hydrogel films to fully swell and remove unreacted reagents. The same CBHTF coating process was conducted on the SiO_2-modified SPR chips. Before spin-coating, the SiO_2 surface was washed by immersion in piranha solution for 15 mins followed by ammonium hydroxide solution for 15 mins to generate hydroxyl groups. The chips were then washed with DI water and dried with filtered air. The CBHTF was directly coated on the SiO_2 surface without SAM modification.

6.2.4 Film thickness and film stability analysis

The thickness of CBHTFs were determined using an ellipsometer, (Model alpha-SE, J.A. Woollam, Lincoln, NE) using a 380–900 nm wavelength range at an incidence

angle of 70°. The results were fitted to a Cauchy model. Four locations on each sample were analyzed to ensure uniformity of the hydrogel films. The stability of CBHTFs was studied by monitoring changes in thickness after immersion in PBS solution and shaking for 12 hrs, 24 hrs, 3 days and 30 days. Before each thickness measurement, CBHTF-modified chips were rinsed with DI water and dried with filtered air. All the thicknesses were measured under dry condition unless otherwise specified.

6.2.5 Nonspecific protein adsorption, antibody immobilization, and antigen detection

Nonspecific protein adsorption, antibody immobilization, and antigen detection were monitored using a custom-built four-channel SPR sensor as described previously [174]. To measure protein adsorption, undiluted human serum was injected (10 min, 40 μL/min) and the wavelength shift between PBS baselines was converted to a surface coverage. Anti-TSH was immobilized by first injecting 10 mM SA (pH 5), followed by EDC/NHS (0.2 M/0.05 M in water) for 7 min at 30 μL/min. Then, anti-TSH (50 μg/mL in 10 mM HEPES pH 7.5) was injected (20 min, 20 μL/min) followed by deactivation with 10 mM BA (pH 9) for 10 min, then 10 mM GLY (pH 4) and SA for 10 min, all at 30 μL/min. Immobilization was calculated as the difference between SA baselines before Anti-TSH injection and after deactivation. TSH antigen binding was then monitored by first injecting PBS and then antigen (1 μg/mL in PBS at 40 μL/min) following by PBS.

6.2.6 Statistical methods

Statistical analysis was performed using Excel. Mean values with standard deviation are reported and all experiments were performed in triplicate. The error bars correspond to the standard deviation

6.3 Results and Discussion

6.3.1 Synthesis of CBAAX and selection of SAM modification on gold chips

Crosslinker selection plays an important role in the nonfouling performance of zwitterionic hydrogels [175]. Zwitterionic materials repel nonspecific protein adsorption through strong binding to water via electrostatically induced hydration. However, traditional crosslinkers such as widely-used N,N'-methylenebis(acrylamide) (MBAA) are only moderately water soluble (not more than 10%). They can degrade the nonfouling performance and mechanical strength of the hydrogel system. To overcome this problem, we have synthesized a CBAAX (**Scheme 6.2**) for improved solubility, homogeneity, mechanical properties and compatibility with CBAA monomer to form CBAA-based zwitterionic hydrogel coatings.

CBHTF coatings were deposited by spin-coating aqueous hydrogel solutions onto gold chips, followed by photoinitiated polymerization. Notably, we found CBHTF uniformity to be related to the hydrophilicity of a chip surface. Grains and particles were observed in the CBHTF after initial coating on a cleaned bare gold SPR chip. Therefore, further chips were modified with one of several SAMs, including $C_{11}COOH$, $C_{11}OH$, and C_{11}, to alter surface hydrophilicity and form a smoother film. CBHTFs could be successfully coated on $C_{11}COOH$ and $C_{11}OH$ SAM-modified gold chips with relatively good uniformity, while they could not be formed on the C_{11} SAM-modified chip used as a negative control. **Table 6.1** shows the water surface contact angles of different SAM-modified gold chips for their hydrophilicities. The hydrophobic C_{11} SAM-modified substrate presented a 78.3º contact angle, and strongly repelled the attachment of the aqueous hydrogel solution as expected. The carboxyl tail groups present in the $C_{11}COOH$

SAM resulted in a very low contact angle (~5º), even compared with that of the $C_{11}OH$ SAM (~16º). On this $C_{11}COOH$ SAM, the CBHTF demonstrated the best uniformity, greatest film thickness and best nonfouling performance. We hypothesize that the fouling resistance of CBHTFs is highly dependent on their surface uniformity, and thus hydrophilic pre-modification of gold chips is necessary for optimal performance. Due to the excellent uniformity of films grown on $C_{11}COOH$ SAM-modified chips, we selected this SAM for subsequent experiments to optimize nonfouling and test antibody immobilization.

6.3.2 Control of CBHTF thickness and stability test

The thickness of CBHTFs could be precisely controlled by varying the CBAAX concentration in the stock hydrogel solution. The CBAA monomer concentration was fixed at 9 wt%, and the CBAAX crosslinker was added in ratios from 0 to 20 mol% of the CBAA monomer. As shown in **Figure 6.1a**, CBHTF thickness increases with an increased crosslinker ratio because of enhanced accumulation of the 3D polymer network. The film thickness in the absence of crosslinker was only 12 nm. In the presence of CBAAX, well-controlled film thicknesses ranging from ~15 to ~40 nm could be attained with CBAAX ratios ranging from 0.5% to 6%, and ~90 to ~150 nm thicker films were achieved with higher CBAAX ratios between 10 and 20%. Film thicknesses showed higher variations when 20% CBAAX was used, as the reaction was more difficult to control under this high crosslinker ratio. These two film thickness regions are both desirable for different coating applications.

Figure 6.1b shows the stability of CBHTFs immersed in PBS for different periods of time. The thickness of CBHTFs containing 20% CBAAX only decreased

slightly after immersion for 30 days, from 145 nm to 142 nm. Meanwhile, CBHTFs formulated with 3% and 6% CBAAX showed even better stability, with no obvious change in film thickness. However, the thickness of the CBAA polymer brush film grafted without CBAAX crosslinker decreased from 12 nm to 1 nm over one month. These results emphasize how important crosslinker selection is to achieve stable films. With CBAAX incorporation, robust and well-controlled CBHTF coatings were achieved using this simple coating method.

6.3.3 Protein resistance test in human blood serum

To challenge CBHTFs with complex media, we used an SPR sensor to measure protein adsorption from undiluted human blood serum onto CBHTFs of varying thicknesses coated on C_{11}COOH-modified gold chips. **Figure 6.2** shows this protein adsorption from 100% serum as a function of CBHTF thickness. High fouling (~40-70 ng/cm^2) was seen at a CBHTF thickness of less than 20 nm. However, when the CBHTF thickness was over 25 nm, protein adsorption dropped to an ultra-low fouling level (<10 ng/cm^2). The lowest fouling observed was less than 5 ng/cm^2 at a film thickness of 29.7 nm. The maximum film thickness tested was around 45 nm since the SPR detection sensitivity drops exponentially when away from the surface. The higher level of protein adsorption seen onto 45-nm-thick CBHTFs was attributed to a reduced film uniformity compared with those of lower thicknesses. For pCB brush coatings, a high packing density of zwitterionic moieties is the key to achieving strong hydration and effective nonfouling performance. For CBHTFs, the crosslinking density plays an important role in surface nonfouling properties. Utilizing higher concentrations of CBAAX (> 2%) allowed us to increase both the film thickness and the degree of crosslinking in a

controlled fashion. To test CBHTF performance on a different hydrophilic surface other than COOH SAM, we modified chips with SiO_2 before hydrogel coating and serum challenge. **Figure 6.3** shows a typical SPR sensorgram of protein adsorption from undiluted blood serum on these SiO_2-modifed chips coated with a 27.2 nm-thick CBHTF. Less than 5 ng/cm^2 of protein adsorption was seen for these chips as well, validating the broad applicability of this coating method. For both types of modified chips, optimizing the crosslinking density is a key to achieving ultra-low fouling.

6.3.4 Surface functionalization and detection

It has been demonstrated previously that zwitterionic pCB-based coatings possess abundant functionalizable groups that enable antibody immobilization via NHS/EDC amino-coupling chemistries, and that these coated surfaces can maintain an ultra-low fouling background before and after antibody functionalization [27]. However, these pCB coatings are typically grafted via ATRP, and are quasi-two-dimensional (2D) films intrinsically limited to a maximum ligand immobilization capacity of a monomer (~250 ng/cm^2). In contrast, the CBHTFs developed in this work comprise a 3D matrix with CB moieties on each monomer *and* crosslinker unit, enhancing the functionalization capacity well beyond that of 2D films.

To study the antibody immobilization capacity of CBHTFs, we functionalized the films with antibodies against human thyroid stimulating hormone (anti-TSH). Antigen binding and nonspecific protein from undiluted human serum were investigated using SPR. **Figure 6.4** shows a typical SPR sensorgram of the overall process, i.e., surface activation, antibody immobilization, surface deactivation and antigen detection as conducted on a CBHTF with 4% CBAAX content as described in the experimental

section. Using SPR, we systematically investigated the influence of crosslinking density (i.e., the CBAAX ratio) on antibody loading capacity and antigen detection. As shown in **Figure 6.5**, the optimal antibody loading was around 693 ng/cm^2 at a CBHTF thickness of ~28 nm containing 3% CBAAX, a threefold higher loading capacity than that of 2D pCB films previously reported [156]. We also measured the wet thickness of the optimal CBHTF; it had swelled from ~28 nm to ~63 nm, indicating its 3D structure. Notably, the loading capacity decreased to 411 ng/cm^2 in a thicker ~40 nm film. The higher crosslinker content rendered the gel network denser, inhibiting the diffusion of antibodies to binding sites. The antigen (i.e., TSH) binding capacity in the optimized ~28 nm film was 68.5 ng/cm^2, corresponding to a calculated bioactivity ratio of 0.71. We also tested the nonspecific fouling resistance of the optimized CBHTF after antibody immobilization, and found it to remain under 5 ng/cm^2 from undiluted serum.

In this work, the most important factor to achieve ultra-low fouling and high antibody loading was the crosslinker ratio. Once the crosslinker ratio was above 2%, the CBHTFs demonstrated good stability and showed relatively low protein adsorption due to the higher crosslinking density. However, the optimized crosslinker ratio for maximum antibody loading was in the middle of the range, as higher crosslinker content could make the CBHTF too dense and inhibit antibodies from diffusing in. These results indicate that control over the architecture of zwitterionic hydrogel thin films is the key to their unique capacity for ultra-low nonspecific protein adsorption with high ligand loading.

6.4 Conclusions

In summary, we have developed a facile approach to realize ultra-low fouling and high ligand loading with a highly-crosslinked, purely zwitterionic, carboxybetaine thin

film hydrogel (CBHTF) coating platform. The CBHTF on a hydrophilic surface demonstrated long-term stability. By varying the crosslinker content in the spin-coated hydrogel solution, the thickness of CBHTFs could be precisely controlled from 15~150 nm. Optimized CBHTFs exhibited ultra-low nonspecific protein adsorption below 5 ng/cm^2, and their 3D architecture allowed antibody loading to reach 693 ng/cm^2. This facile coating technique was also demonstrated to be directly applicable to an alternative hydrophilic substrate modified with SiO_2, indicating that its potentials for broad diagnostic applications.

6.5 Tables

Table 6.1 The selection of hydrophilic SAM modification on the gold SPR chips

		SAM on gold chip		
	Bare gold	$C_{11}OH$	$C_{11}COOH$	C_{11}
Contact Angle (°)	25.6 ± 2.2	15.7 ± 1.3	5.2 ± 1.9	78.3 ± 3.6
Thickness (nm)	22.3 ± 3.5	26.1 ± 2.2	29.7 ± 1.7	1.2 ± 0.8
Serum Fouling (ng/cm^2)	17.8 ± 4.3	9.4 ± 3.7	3.5 ± 1.3	–

6.5 Schemes

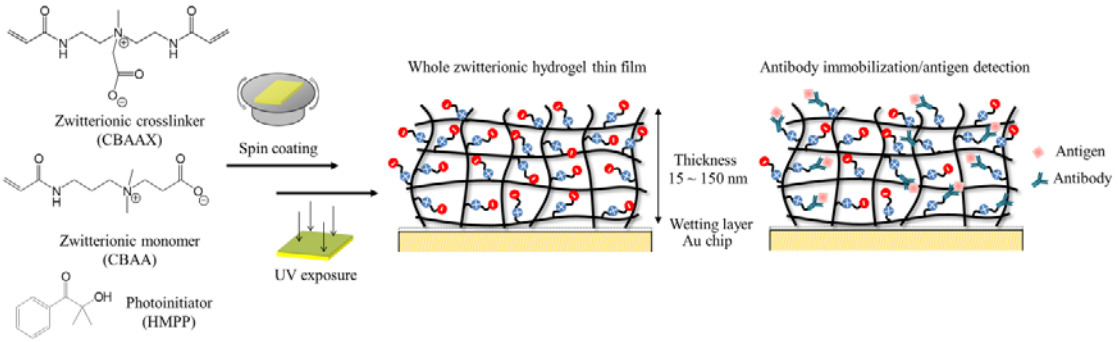

Scheme 6.1 Overview of the coating process to generate CBHTFs on the surface of SPR chips

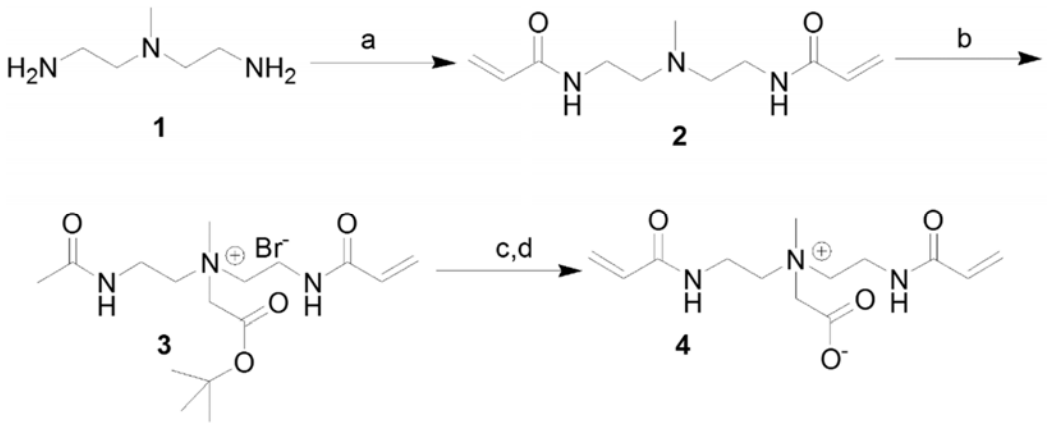

Scheme 6.2 Chemical synthesis of carboxybetaine diacrylamide (CBAAX)

(a) DIEA, Acryloyl chloride, DCM, 75% (b) $BrCH_2CO_2tBu$, CH_3CN, 60°C, 73% (c) TFA:DCM 1:1, (d) MeOH, IRN-78 resin hydrolysis 84%

6.6 Figures

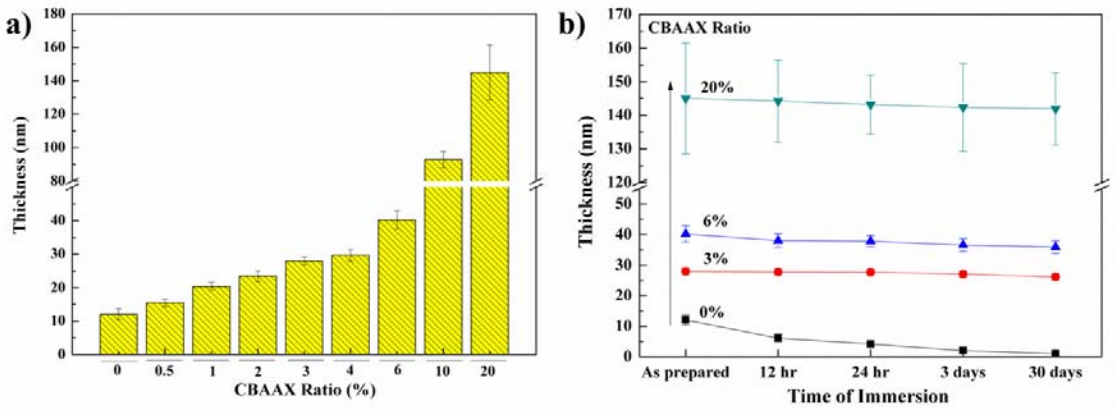

Figure 6.1 Thickness control and stability test

(a) Thickness control of the CBHTFs by tuning the concentration of CBAAX crosslinker. The content of CBAAX is presented in a relative percentage to monomer. (b) Film stability of the CBHTFs in the PBS solution for over 30 days. The error bars correspond to the standard deviation of three replicates.

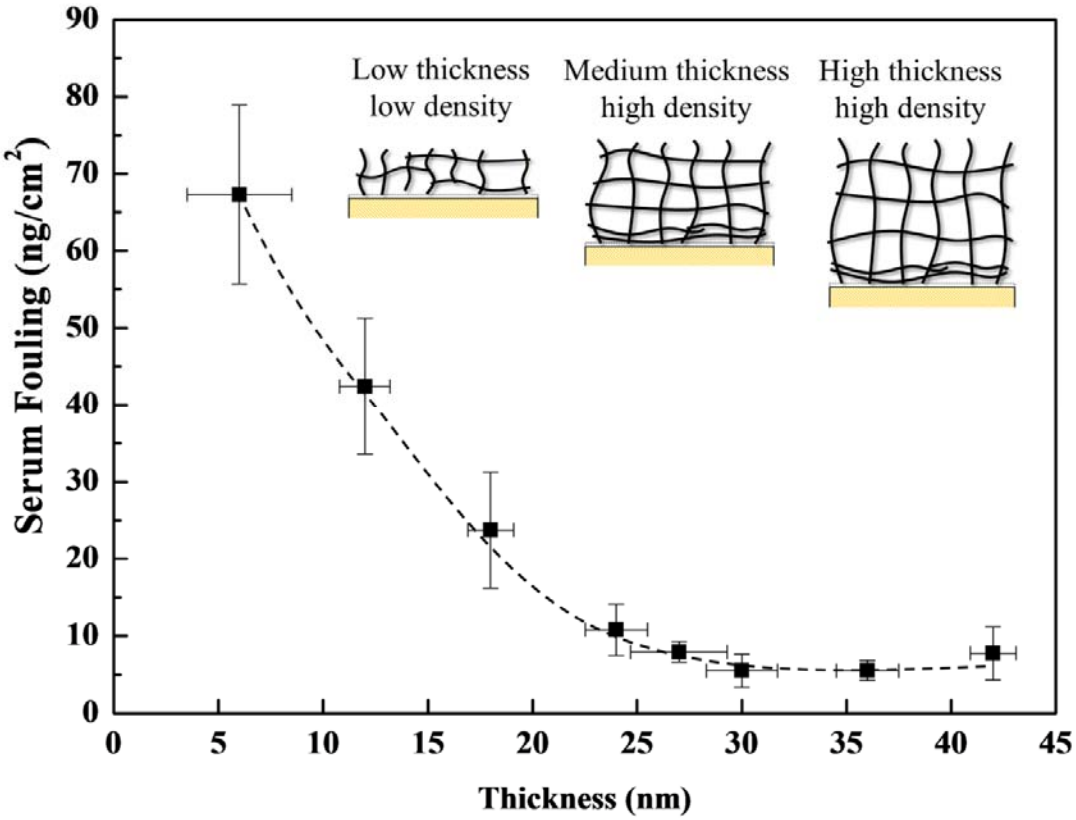

Figure 6.2 Optimization of nonfouling performance

Protein adsorption on CBTHFs from 100% human blood serum as the function of CBAAX ratio measured by SPR sensor. The error bars correspond to the standard deviation of three replicates.

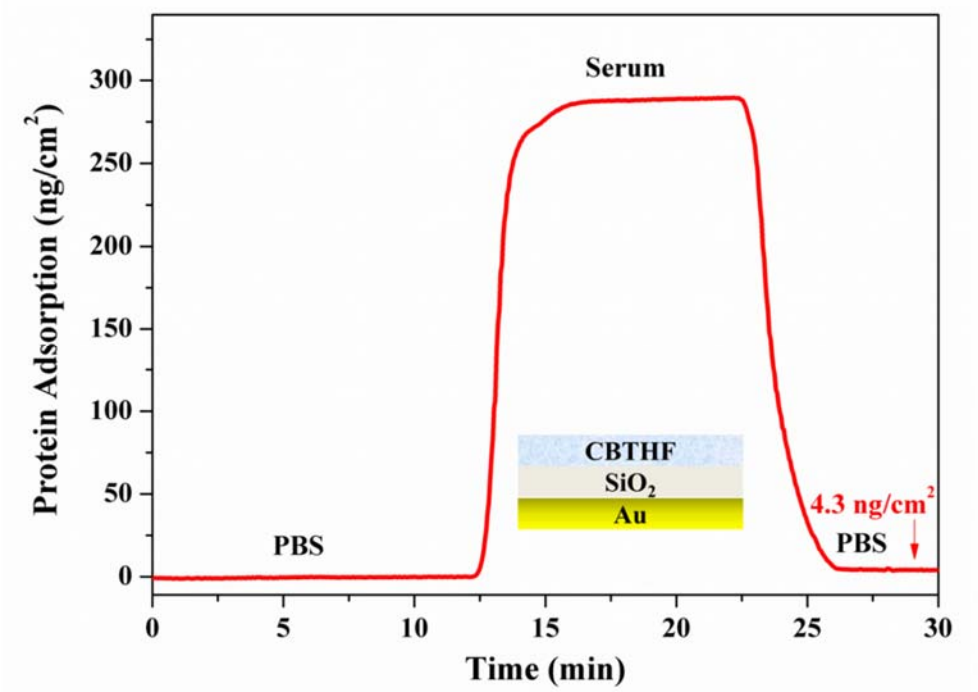

Figure 6.3 CBHTF coated on SiO_2

Typical SPR sensorgram for the fouling test on the CBHTF (thickness = 27.2 nm) modified SiO_2 surface in contact with undiluted human serum.

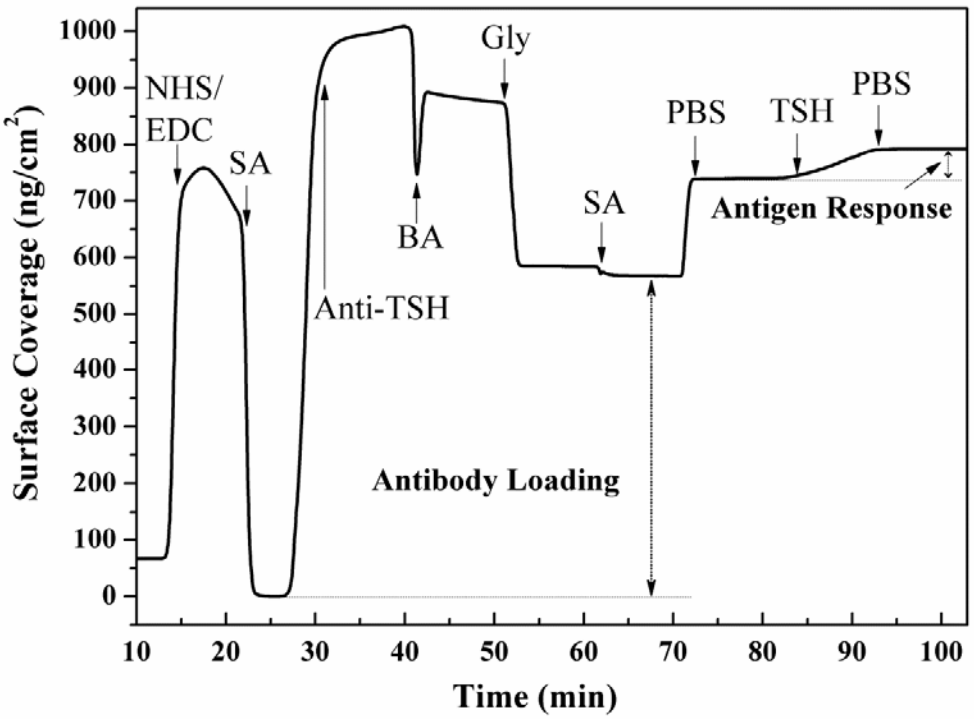

Figure 6.4 Typical SPR sensorgram for anti-TSH immobilization on CBTHF and followed with TSH antigen detection

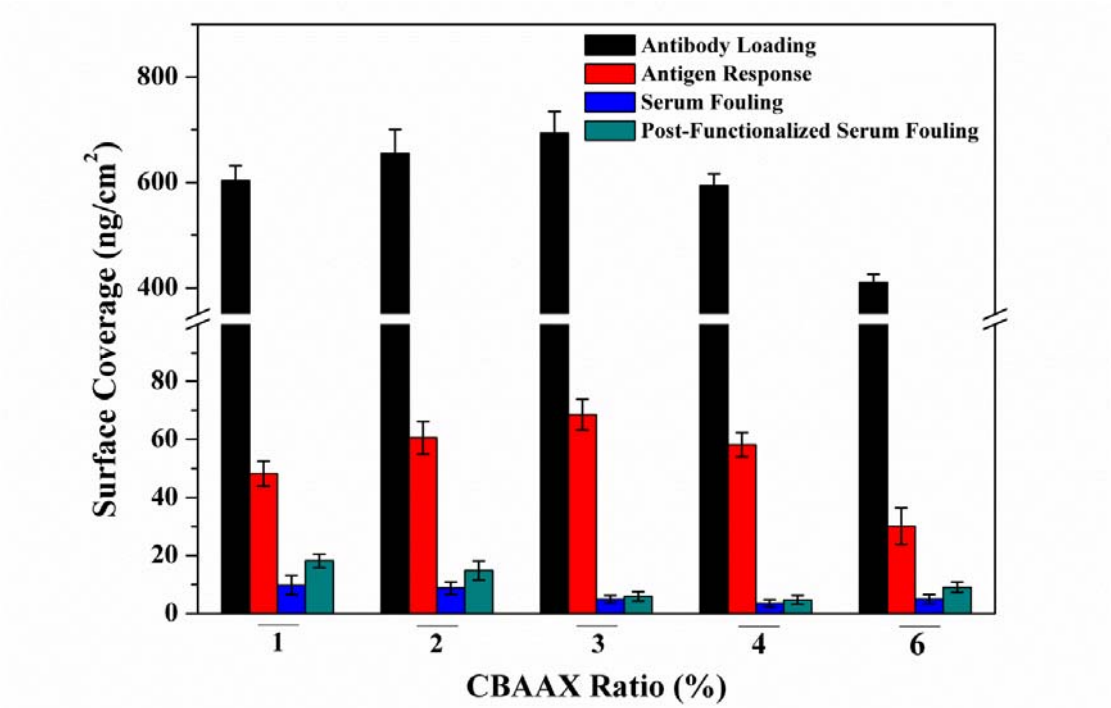

Figure 6.5 Antibody loading, antigen response, and nonfouling properties of CBTHFs as the function of CBAAX crosslinker ratio

The error bars correspond to the standard deviation of three replicates.

Chapter 7 Rapid and Sensitive Detection of Anti-PEG in Blood Serum Based on SPR Sensor

On the on the contrary to a generally accepted assumption that PEG is non-immunogenic and non-antigenic, large numbers of studies report that uricase, ovalbumin, and some other PEGylated agents can elicit antibody against PEG (anti-PEG). The generation of anti-PEG has been shown to be related to the limitation of efficacy and reduction of tolerance of several therapeutic agents. Of major importance is the recent finding of a 22 - 25% occurrence of anti-PEG in general population. Thus a facile, rapid, sensitive and reliable technique to detect the anti-PEG is highly desired. In this work, we have developed a PEG modified surface plasmon resonance (SPR) biosensors for the anti-PEG detection. By optimization of the surface chemistry, we can achieve the anti-PEG quantitative sensing directly from diluted blood serum within 40 min showing better sensitivity compared with traditional ELISA method. The limit of detection can be down to 10 ng/mL and both IgM and IgG isotypes can be differentiated by this method. The development of this technology will lead the successful study of pre-existing anti-PEG generated in healthy individuals, and can also be used to pre-screen and monitor the anti-PEG level in the patients who receive the treatment with PEGylated compound.

7.1 Introduction

Polyethylene glycol (PEG) is the most widely used conjugated polymer in the pharmaceutical industry to manipulate the pharmacokinetics of therapeutic and diagnostic agents [176, 177]. The attachment of conjugated PEG (PEGylation) to biomedicines such as recombinant proteins and peptides, extends theirs circulation time, reduces the toxicity,

immunogenicity and antigenicity while improving the therapeutic efficacy. PEG has also been covalently attached to other therapeutic agents including oligonucleotides, small organic molecules as well as phospholipids. As reviewed by Garay [178], at least 12 therapeutic PEGylated agents have been approved by FDA, such as PEG-asparaginase for leukemia and lymphoma, PEG-interferon for chronic hepatitis C virus, PEG-uricase for chronic gout and PEG-adenosine deaminase for immunodeficiency syndrome.

Nevertheless, in contrast to the accepted general assumption that PEG is non-immunogenic and non-antigenic, an emerging number of studies demonstrate that the immune system can elicit antibody formation specifically against PEG (anti-PEG) both in animals or humans [179]. The generation of anti-PEG can accelerate the clearance of PEGylated therapeutics thus reducing the therapeutic efficacy. For instance, the rapid clearance of PEG-asparaginase has been observed for a subgroup of the pediatric patient treated for acute lymphoblastic leukemia, associated with the presence of anti-PEG [180]. Recent clinical investigations of PEG-uricase in refractory chronic gout patients unequivocally showed that anti-PEG antibodies correlate with a reduction in drug effectiveness [181]. Moreover, a recent finding has demonstrated that a 22%-25% occurrence of anti-PEG with both IgG and IgM in healthy blood donors [178]. It might due to the humans' greater exposure to PEG or PEG containing compounds in cosmetics, processed foods, pharmaceuticals, and industrial manufacturing. Thus to study the ratio and distribution of pre-existing anti-PEG generated in healthy individuals, and also to pre-screen and monitor the anti-PEG level in the patients who will receive the treatment with PEGylated compound, a facile, rapid, sensitive and reliable technique to detect the anti-PEG is highly desired.

There are a variety of methods have been reported for anti-PEG detection such as serology, flow cytometry, Western blotting and enzyme-linked immunosorbent assays (ELISA) [182-184]. However, most of them have complicated process requiring skilled labor and are time-consuming. For example, the serology method is based on the passive agglutination of PEG-coated red blood cells. The cytometry requires the using of PEG-modified pellet and florescent-labeled immunoglobulins. The ELISA method can provide better sensitivity but contains multiple steps. And for quantification, a calibration standard is needed for each time.

To overcome these shortcomings, we propose a novel method simultaneously with high sensitivity, simple operation process, rapid detection time and capability for antibody isotype/subclass differentiation by using a surface plasmon resonance (SPR) sensor. SPR is a powerful technique to monitor label-free biomolecular interactions and biomolecule/surface interactions in liquids with detection limits as low as nanogram levels. In this work, we modified PEG based materials on the SPR sensor chips. The PEG modification is originally nonfouling, which can resist the nonspecific adsorption from diluted blood serum thus diminishing the background noise. If there are anti-PEGs existing in the blood sample, when they are flowed through the surface of PEG modified SPR chip, they can specifically bind to the PEG moieties illustrating strong signal in the SPR sensorgram. We studied the performances of different PEG based modifications, including grafted polymer brush (poly(ethylene glycol) methyl ether methacrylate, PEGMA), linear polymer (methoxyl PEG thiol, mPEG) and short hydrocarbon thiol(2-(2-{2-[2-(1-mercaptoundec-11-yloxy)-ethoxy]-ethoxy}-ethoxy)-ethanol, EG4). The mPEG, which can readily be coated on the SPR gold chips, demonstrated best sensitivity. The

quantitative anti-PEG detection could be achieved within 40 mins with simple steps. The limit of detection could be as low as 10 ng/mL. By using secondary antibody, we could also distinguish the IgG and IgM generation in the whole anti-PEGs.

7.2 Experimental Section

7.2.1 Materials

Recombinant uricase from Candida sp. and all chemicals were purchased from Sigma-Aldrich unless otherwise noted and were used as received. Methoxy polyethylene glycol succinimidyl carbonate (mPEG-NHS, 10kDa, 95%), and mPEG (5kDa, 95%) were obtained from Nanocs. EG4 was purchased from ProChimia.

7.2.2 Protein conjugation

Uricase-PEG conjugates were prepared in 50 mM HEPES buffer (pH 8.5), with uricase concentration at 1 mg/mL and mPEG-NHS concentration at 10 mg/mL. The reaction was stirred at 4 °C overnight. Then the conjugates were concentrated and washed extensively with PBS, pH 7.4, using a 300-kDa molecular weight cutoff centrifugal filter. The protein residue activity was measured by a commercially available uricase activity kit (Life Technologies).

7.2.3 In vivo anti-PEG generation and sample preparation

To generate the anti-PEG and collect the blood sample. The PEGylated uricase was injected in Spraque–Dawley rats (male, body weight 74–100 g). Each sample has three duplicates to generate statistical significance. All animal experiments adhered to federal guidelines and were approved by the University of Washington Institutional Animal Care and Use Committee. For the intravenous (IV) immunization, the PEGylated uricase was administered into the rat via tail vein injection at the dose of 25 U/kg body

weight. Blood samples were collected from the tail vein 5 weeks after the injection. For the subcutaneous (SC) immunization, the rats were injected subcutaneously on the back with the immunogens on days 0, 14, and 21. The first immunization was in Freund's complete adjuvant. Subsequent immunizations were in Freund's incomplete adjuvant. Blood was collected prior to immunization (prebleed) and 5 weeks after the first immunization. All the sera were prepared from each bleed by centrifugation and were kept frozen at until use.

7.2.4 ELISA

The antigens used in direct ELISAs consisted of BSA-PEG conjugates (for detection of anti-PEG antibody). BSA-PEG conjugates were made following the same procedure as uricase-PEG samples. For ELISA experiments, 100 μL antigen solution (10 μg/mL of protein concentration) prepared in 0.1 M sodium carbonate buffer, pH 10.5, was used to coat each well of the 96-well plates. During coating procedure, plates were incubated at 4 °C overnight. After removing antigen solutions, the plates were washed five times using PBS (PBS 7.4) and then filled with blocking buffer (1% BSA solution in 0.1 M Tris buffer, pH 8.0). It is important to avoid using any buffer that contains PEG-like detergents, e.g., Tween 20 and Tween 80. After incubation at room temperature for 1 h, blocking buffer was removed, and all wells were washed with PBS for another five times. Serial dilutions of rat sera in PBS containing 1% BSA were added to the plates (100 μL/well), which were incubated for 1 h at 37 °C. The plates were then washed five times with PBS. Goat anti-rat IgM or IgG conjugated to HRP (Bethyl Laboratories) was used as the secondary antibody for detection of IgM and IgG. After adding the secondary antibody, plates were incubated at room temperature for 1 h and then washed five times

using PBS before the addition of 100 μL/well HRP substrate 3,3′,5,5′-tetramethylbenzidine (TMB; Bethyl Laboratories). The plates were shaken for 15 min, and 100 μL stop solution (0.2 M H_2SO_4) was added to each well. Absorbance at 450 (signal) and 570 nm (background) was recorded by a microplate reader. Prebleeding sera were used as negative control for all ELISA detections. Commercially available rat anti-PEG antibodies were used as positive control for anti-PEG detections. The positive signal was defined as absorbance significantly larger than corresponding negative control.

7.2.5 SPR detection of anti-PEG

PEGMA polymer brushes were grafted onto gold SPR sensor chips following previously published methods [185]. Brush thickness was measured by a spectroscopic ellipsometry (Sentech SE-850). The mPEG and EG4 were modified on the gold SPR chips by immersing the UV-ozone cleaned chips in the corresponding thiol ethanol solution (1 mg/mL for mPEG, and 1 mM). A custom-built SPR sensor was used in this study. All experiments were done following the sequence of flowing PBS for 10 min, 1:20 diluted serum in PBS for 15 min, and PBS for 15 min at flow rate of 30 μL/min. For the experiment of IgG and IgM differentiation, goat anti-rat IgM or IgG (10 μg/mL) was injected continuously after anti-PEG detection for 15 min, followed by PBS for 15 min. For the SPR sensor used in the study, a 1 nm SPR wavelength shift represents a surface coverage of ~17 ng/cm^2 for proteins. Detection limit for the SPR sensor used in this work is 0.3 ng/cm^2.

7.3 Results and Discussion

7.3.1 Antibody production

In this work, we directly conducted the anti-PEG detection from the blood samples collected from in vivo animal studies to prove that our technology can be directly applied for the real-world application. We selected the Spraque–Dawley rat as the animal model and immunized anti-PEG by injecting the PEG-Uricase intravenously and subcutaneously (**Figure 7.1a**). We investigated both of the IV and SC immunizations because they can induce different amounts and compositions of anti-PEG (IgG or IgM). After the generation of anti-PEG and the collection of the blood serum which contains the anti-PEG. We used the SPR sensor coated with different PEG modifications to achieve the detection (**Figure 7.1b**).

7.3.2 Selection of surface chemistry

PEG based materials are most widely used nonfouling or stealth materials which can resist the nonspecific protein adsorptions. Herein, the PEG would be coated on the SPR sensors not only as the antigen for the specific anti-PEG binding but also as the nonfouling modification to reduce the background noise from the blood serum sample. Thereby, as shown in **Figure 7.2a,b,c**, we studies three different types of PEG modification on the SPR sensors include PEGMA polymer brush, mPEG linear polymer, and EG4 short thiol forming self-assembled monolayers (SAM). A sample IV immunized blood serum sample was diluted for 20 times by PBS and injected through the SPR sensors coated with these three modifications. And we also flowed a control serum which was collected before the IV injection**. Figure 7.2c,d,e** show the SPR sensorgrams of with the three modifications respectively. On the PEGMA modified sensor, the anti-PEG

adsorption is around 40 ng/cm^2 and there is no adsorption from the control sample. On the mPEG coated sensor, it shows ~ 98 ng/cm^2 anti-PEG adsorption from the immunized sample and only 0.3 ng/cm^2 from the control. While the EG4 SAM cannot effectively resist the nonspecific protein adsorption from the serum, showing similar results from both the immunized serum and control serum. Based on these results, mPEG was the best modification demonstrating highest sensitivity while eliminating the background noise and it is selected for the further detections and studies.

7.3.3 Determination of anti-PEG titer

An antibody titer is a measurement of how much antibody in the sample that recognizes a particular epitope, expressed as the inverse of the greatest dilution that still gives a positive result. ELISA is a common means of determining antibody titers. In this study, for the IV immunized samples, the ELISA anti-PEG titers was measured as 3200 (result is not shown here). To compare with ELISA, the same IV serum containing anti-PEG was diluted for 20, 200, 1000 and 5000 times with PBS and the diluted samples were detected with mPEG modified SPR sensors. **Figure 7.3a** demonstrates the SPR sensorgrams, and the anti-PEG was detected in all these samples which indicate that the anti-PEG titles for SPR is 5000. **Figure 7.3b** summarizes the antibody adsorptions with different dilution factors. In addition, we also conducted the detections by pausing method, which means to stop the blood serum sample for 1hr inside the SPR detection chambers to increase the binding time. It mimics the ELISA method to increase the reaction time to get better sensitivity. However, we didn't observe any significant improvement comparing with the dynamic flowing method and the results are also summarized in **Figure 7.3b**.

7.3.4 Differentiation of IgG and IgM

We successfully achieved the sensitive and rapid anti-PEG detection from blood serum by using mPEG modified SPR sensor. But the results shown before are the total amounts of the anti-PEGs and they are composed of different isotypes (mostly IgG and IgM). To further differentiate the IgG and IgM levels in the whole anti-PEGs, we continued flow the anti-IgG and anti-IgM after the binding of anti-PEGs. **Figure 7.4a,b** illustrates the SPR sensorgrams of anti-PEG detections and followed IgG and IgM classifications for both the IV and SC samples. For the IV samples, most of the antibodies are composed of IgM and IgG only shows very small response. While the SC samples shows huge amount of total anti-PEGs and the amount of IgG and IgM are all higher than the IV samples. The exact amounts of adsorption are listed in the **Figure 7.4c**. These experiments demonstrate that our method can effectively classify the isotype of the detected antibodies, which provides essential information for a lot of clinical studies and applications.

7.3.5 Calibration for quantitative detection

By using our method, we measure the total mass amount of anti-PEG binding to the PEG polymers coated on SPR surface. If we want to the exact concentration of the anti-PEG in the blood samples, we also need to do a simple calibration for the SRP sensor, which is to determine the relationship between the anti-PEG concentrations to the SPR wavelength shifts. To do the calibration, we detected the solutions spiked with different concentrations of anti-PEG IgM ranging from 1 ng/mL to 100 μg/mL. As shown in **Figure 7.5a**, the SPR illustrates different response to different concentrations of anti-PEG. When the concentration is higher than 20 μg/mL, a saturation of adsorption is

observed. **Figure 7.5b** demonstrates the sensorgrams detecting the concentrations from 1ng/mL to 100 ng/mL. Obvious responses are shown for both 10 and 100 ng/mL while there is no detection of 1 ng/mL. Thus the limit of detection of the mPEG coated SPR method is 10 ng/mL, which is 10 times lower than the reported ELISA method. The calibration curve is shown in **Figure 7.5c** by plotting the wavelength shift as a function of anti-PEG concentration. A linear dynamic range is achieved between 0 to 10 μg/mL as illustrated in **Figure 7.5d**. Based on the generated calibration curve, we can calculate the real anti-PEG concentrations of IV and SC samples. The anti-PEG concentration is about 113 μg/mL for IV immunized blood serum, and 226 μg/mL for SC injection.

7.4 Conclusions

In conclusion, we have developed a simple, rapid, sensitive and reliable technique of direct anti-PEG detection in blood samples. To proof the capability of our method, we produced anti-PEG antibodies by injecting PEG-uricase in animal model and we collected the blood serum samples for detection. By coating the mPEG on the SPR sensor, we could reach 5000 as the antibody titer (3200 for ELISA method). The total antibodies could also be classified as IgG and IgM separately and quantitatively. The limit of detection of this technique is 10 ng/mL, which is suitable for the clinical relevant using.

7.5 Figures

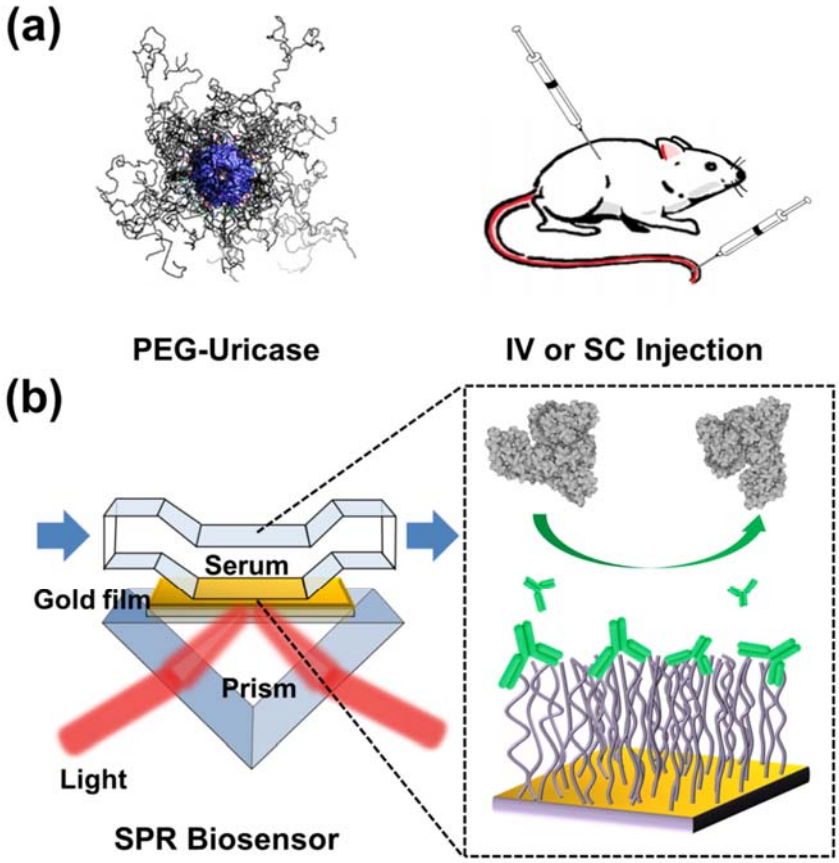

Figure 7.1 Anti-PEG detection by using the PEG coated SPR biosensor

(a) Schematic illustration of PEG-Uricase and the immunization study by IV and SC injection. (b) Schematic illustration of anti-PEG detection by using the PEG coated SPR biosensor.

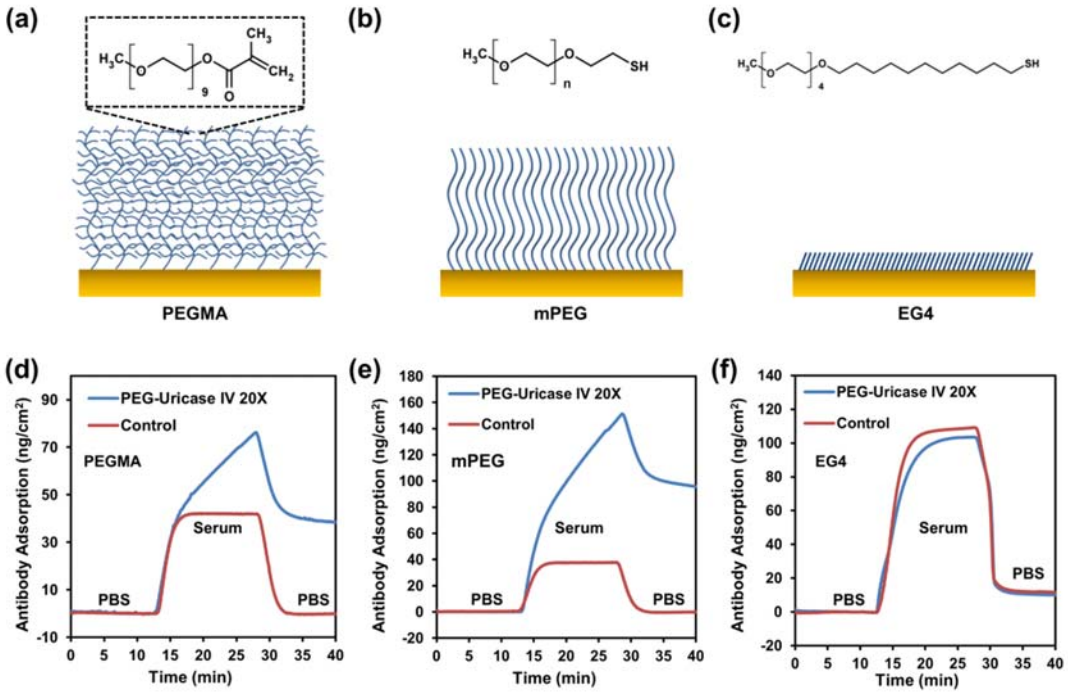

Figure 7.2 Selection of surface chemistry

(a) (b) (c) Schematic illustration PEG based surface modification on the gold SPR sensor including PEGMA polymer brush, mPEG thiol linear polymer and EG4 SAM, respectively. (e) (f) (g) Typical SPR sensorgrams of anti-PEG binding to the three different PEG based modification on SPR chips.

(a)

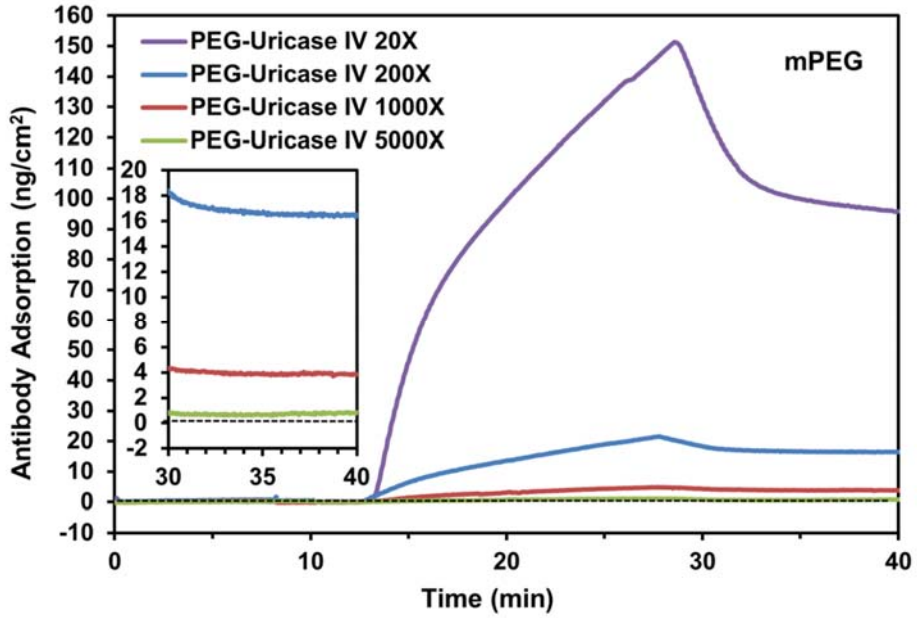

(b)

Dilution Factor	Antibody Adsorption (without pause) (ng/cm²)	Antibody Adsorption (with pause) (ng/cm²)
20	98.15 ± 7.28	95.66 ± 9.34
200	16.45 ± 1.42	15.01 ± 3.35
1000	3.81 ± 0.25	4.06 ± 1.15
5000	0.86 ± 0.11	0.91 ± 0.32

Figure 7.3 SPR detection of anti-PEG with different dilution factors

(a) SPR sensorgrams of anti-PEG adsorption of the IV blood serum with different dilution factors. (b) Summary of the antibody adsorption with and without pause process.

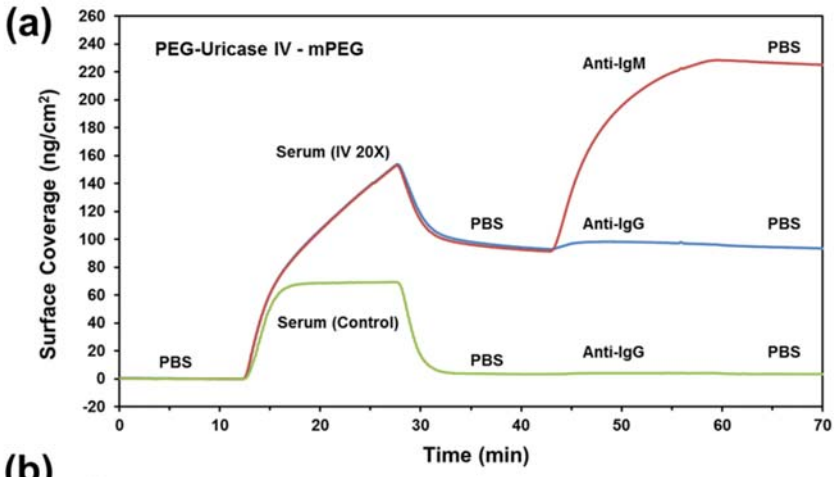

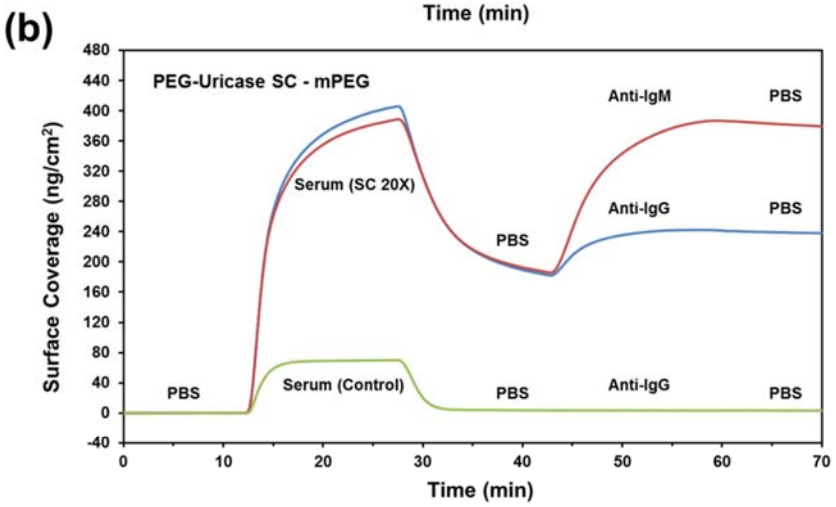

(c)

Injection Type	Total Antibody Adsorption (ng/cm²)	Anti-IgM Adsorption (ng/cm²)	Anti-IgG Adsorption (ng/cm²)
IV	98.15 ± 7.28	128.52 ± 21.25	3.06 ± 0.85
SC	189.98 ± 7.28	187.34 ± 43.01	56.44 ± 7.31

Figure 7.4 IgG/IgM differentiation

(a) SPR sensorgram of anti-PEG detection and IgG/IgM differentiation of blood serum for IV injection. (b) SPR sensorgram of anti-PEG detection and IgG/IgM differentiation of blood serum for SC injection. (c) Summary of IgG and IgM generations in the IV and SC immunization study.

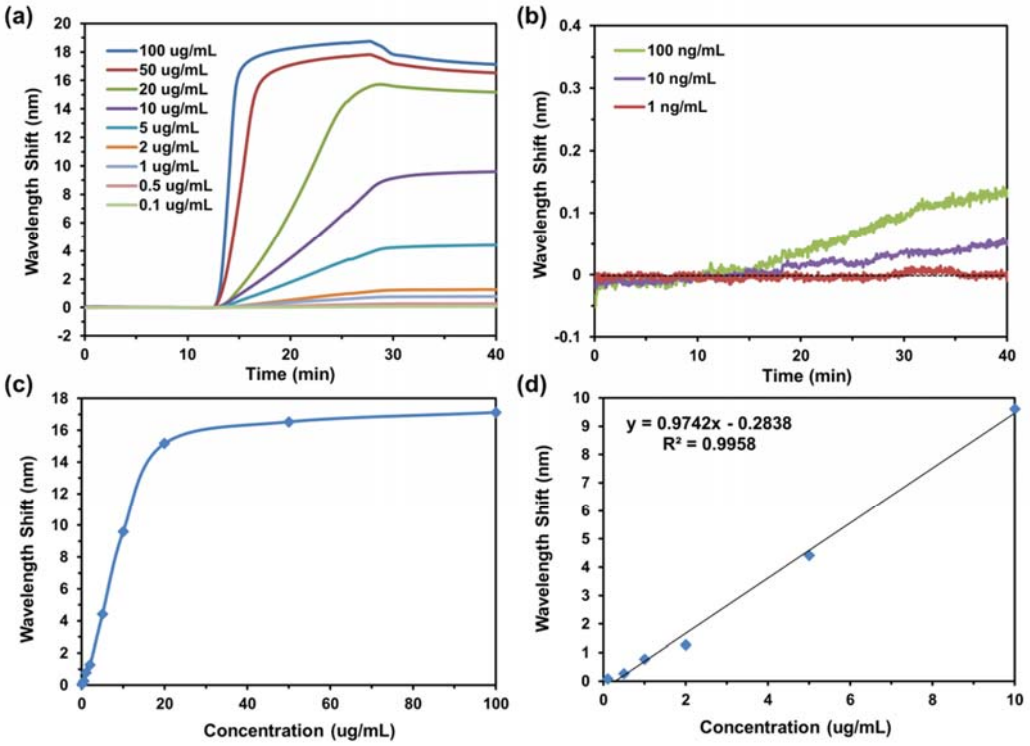

Figure 7.5 Quantification of anti-PEG

(a) (b) SPR sensorgrams of monoclonal anti-PEG IgM detection with different concentrations ranging from 1 ng/mL to 100 μg/mL in PBS. (c) Anti-PEG detection calibration curve based on the wavelength shift as a function of the concentration. (d) A linear dynamic range is shown with the concentrations ranging from 0 to 10 μg/mL.

Chapter 8 Conclusions

This dissertation explores and investigates the multifunctional surface chemistry for SERS and SPR plasmonic biosensing in complex media. The strategy and design of probe molecules for specific detection and signal amplification for SERS sensing are described. The introduction of effective zwitterionic nonfouling modification on the SERS sensor is discussed. In addition, a facile nonfouling/high antibody loading coating method is developed for the SPR sensor. Specific surface chemistry for the anti-PEG detection by SPR is demonstrated.

The first part of the dissertation (Chapter 2 and 3) discusses how to detect the analytes with small Raman activity or no Raman activity by using SERS. A solution is to immobilize a probe molecule for specific binding and signal amplification. In Chapter 2, we describe a method for sensitive and fast fructose detection in undiluted artificial urine by monitoring SERS spectral changes of 4-MPBA probe molecules upon fructose binding which breaks the structural symmetry of the probe molecules. The greater chemical enhancement of the probe molecules not only improves the detection sensitivity but also amplifies the SERS signal that effectively shields the background noise in complex media. The limit of detection of 0.05 mM fructose in PBS and undiluted artificial urine is achieved.

In Chapter 3, we immobilize 4-MBA on a gold SERS substrate to map the local pH_e of single living cells. The 4-MBA functionalized SERS substrate demonstrates good sensitivity and reproducibility. The influence of cations in detecting solutions on the responses of 4-MBA SERS spectra to pH variations is investigated and the calibration curves are established to ensure the detection and mapping accuracy in complex media

such as cell culture media. As a proof of concept, a normal cell line (NIH/3T3) and a tumor cell line (HepG2) are cultured on the 4-MBA modified SERS substrates. The values of local pH_e of living cells are detected and mapped with high spatial resolution and pH sensitivity. The tumor cells display more acidic averaged pH_e.

The second part of the dissertation (Chapter 4 and 5) explores the strategy to introduce zwitterionic nonfouling modification on the SERS sensors to enable the detection in complex media. In Chapter 4, we design and synthesize a special zwitterionic short thiol CBT and introduce it to SERS sensor. The CBT can effectively resist nonspecific adsorption from protein solutions and it possesses very weak Raman activity. This makes it be capable of hiding its own signal in the SERS spectrum, which may cover or overlap with the signal of the analyst. To further increase the nonfouling performance of the modification on SERS, we graft zwitterionic pCBAA polymer brush on the SERS surface via SI-ATRP. The densely packed polymer film can resist the protein adsorption from real-world complex media such as undiluted blood plasma. Without the nonfouling modification, bare gold SERS sensor cannot survive in blood plasma. An anti-cancer drug Doxorubicin is quantitatively detected by the pCBAA modified SERS optofluidic system directly in the human plasma. And we also apply our system for the real-time monitoring of several therapeutic drugs.

The third part of the dissertation (Chapter 6 and 7) investigates specific surface chemistry on SPR for different applications. In Chapter 6, we present a novel and facile approach to develop an ultra-low fouling and high antibody loading coating platform based on zwitterionic CBTHF composed of highly crosslinked hydrogel with whole CB moieties. The CBTHF with controlled crosslinking density and thickness shows long-

term stability. On the optimized CBHTFs, the protein fouling levels from undiluted blood serum are lower than 5 ng/cm^2 and antibody loading can reach 693 ng/cm^2, which cannot be achieved by traditional one layer nonfouling coatings. And in Chapter 7, we show a simple, rapid, sensitive and reliable technique of direct anti-PEG antibodies detection in blood samples. By coating the mPEG on the SPR sensor, we can quantitatively detect the anti-PEG from in vivo blood samples with 10 ng/mL limit of detection. The total antibodies could also be classified as IgG and IgM separately.

In summary, we propose the method to use probe molecule on SERS to detect the analytes with small Raman activity or no Raman activity. Based on the probe strategy, we select 4-MPBA for fructose sensing and 4-MBA for pH_e imaging using SERS. This strategy can easily be tuned for other applications by changing the functional group on the probe molecule. We also introduce zwitterionic nonfouling materials on SERS sensors enabling the SERS detection in the complex media. The zwitterionic short thiol CBT can effectively resist the nonspecific adsorption form single protein solutions. And the zwitterionic pCBAA modification contributes to the therapeutic drug monitoring in blood plasma. The zwitterionic materials possess small Raman activity and can be used as general protection coatings for SERS biosensing in the complex media. The zwitterionic CBTHF shows high antibody loading capacity and ultra-low fouling property, which is a novel and facile approach for surface coating of SPR sensors. This surface modification method illustrates great potentials for broad diagnostic applications. We also develop a simple but robust surface chemistry for anti-PEG detection. This reliable technique can be used to study the occurrence of pre-existing anti-PEG in the general population and help the patients to monitor the anti-PEG level in blood.

References

[1] Larmour IA, Graham D. Surface enhanced optical spectroscopies for bioanalysis. Analyst. 2011;136:3831-53.
[2] Stewart ME, Anderton CR, Thompson LB, Maria J, Gray SK, Rogers JA, et al. Nanostructured plasmonic sensors. Chem Rev. 2008;108:494-521.
[3] Bozhevolnyi SI, Volkov VS, Devaux E, Laluet JY, Ebbesen TW. Channel plasmon subwavelength waveguide components including interferometers and ring resonators. Nature. 2006;440:508-11.
[4] Nath N, Chilkoti A. A colorimetric gold nanoparticle sensor to interrogate biomolecular interactions in real time on a surface. Anal Chem. 2002;74:504-9.
[5] Stiles PL, Dieringer JA, Shah NC, Van Duyne RR. Surface-Enhanced Raman Spectroscopy. Annu Rev Anal Chem. 2008;1:601-26.
[6] Hill RT. Plasmonic biosensors. Wires Nanomed Nanobi. 2015;7:152-68.
[7] Anker JN, Hall WP, Lyandres O, Shah NC, Zhao J, Van Duyne RP. Biosensing with plasmonic nanosensors. Nat Mater. 2008;7:442-53.
[8] Cao YWC, Jin RC, Mirkin CA. Nanoparticles with Raman spectroscopic fingerprints for DNA and RNA detection. Science. 2002;297:1536-40.
[9] Cao YC, Jin R, Nam JM, Thaxton CS, Mirkin CA. Raman dye-labeled nanoparticle probes for proteins. J Am Chem Soc. 2003;125:14676-7.
[10] Wabuyele MB, Vo-Dinh T. Detection of human immunodeficiency virus type 1 DNA sequence using plasmonics nanoprobes. Anal Chem. 2005;77:7810-5.
[11] Qian XM, Peng XH, Ansari DO, Yin-Goen Q, Chen GZ, Shin DM, et al. In vivo tumor targeting and spectroscopic detection with surface-enhanced Raman nanoparticle tags. Nat Biotechnol. 2008;26:83-90.
[12] Alvarez-Puebla RA, Liz-Marzan LM. Environmental applications of plasmon assisted Raman scattering. Energ Environ Sci. 2010;3:1011-7.
[13] Halvorson RA, Vikesland PJ. Surface-Enhanced Raman Spectroscopy (SERS) for Environmental Analyses. Environ Sci Technol. 2010;44:7749-55.
[14] Kneipp J, Kneipp H, Wittig B, Kneipp K. Novel optical nanosensors for probing and imaging live cells. Nanomed-Nanotechnol. 2010;6:214-26.
[15] Golightly RS, Doering WE, Natan MJ. Surface-Enhanced Raman Spectroscopy and Homeland Security: A Perfect Match? Acs Nano. 2009;3:2859-69.
[16] Zhang XY, Young MA, Lyandres O, Van Duyne RP. Rapid detection of an anthrax biomarker by surface-enhanced Raman spectroscopy. J Am Chem Soc. 2005;127:4484-9.
[17] Dasary SSR, Singh AK, Senapati D, Yu HT, Ray PC. Gold Nanoparticle Based Label-Free SERS Probe for Ultrasensitive and Selective Detection of Trinitrotoluene. J Am Chem Soc. 2009;131:13806-12.
[18] Lee A, Andrade GFS, Ahmed A, Souza ML, Coombs N, Tumarkin E, et al. Probing Dynamic Generation of Hot-Spots in Self-Assembled Chains of Gold Nanorods by Surface-Enhanced Raman Scattering. J Am Chem Soc. 2011;133:7563-70.
[19] Yan B, Thubagere A, Premasiri WR, Ziegler LD, Dal Negro L, Reinhard BM. Engineered SERS Substrates With Multiscale Signal Enhancement: Nanoplarticle Cluster Arrays. Acs Nano. 2009;3:1190-202.

[20] Willets KA, Van Duyne RP. Localized surface plasmon resonance spectroscopy and sensing. Annu Rev Phys Chem. 2007;58:267-97.
[21] Tian ZQ, Ren B, Wu DY. Surface-enhanced Raman scattering: From noble to transition metals and from rough surfaces to ordered nanostructures. J Phys Chem B. 2002;106:9463-83.
[22] Xu JJ, Kvasnicka P, Idso M, Jordan RW, Gong H, Homola J, et al. Understanding the effects of dielectric medium, substrate, and depth on electric fields and SERS of quasi-3D plasmonic nanostructures. Optics express. 2011;19:20493-505.
[23] Shafer-Peltier KE, Haynes CL, Glucksberg MR, Van Duyne RP. Toward a glucose biosensor based on surface-enhanced Raman scattering. J Am Chem Soc. 2003;125:588-93.
[24] Rycenga M, McLellan JM, Xia YN. A SERS study of the molecular structure of alkanethiol monolayers on Ag nanocubes in the presence of aqueous glucose. Chem Phys Lett. 2008;463:166-71.
[25] Lyandres O, Shah NC, Yonzon CR, Walsh JT, Glucksberg MR, Van Duyne RP. Real-time glucose sensing by surface-enhanced Raman spectroscopy in bovine plasma facilitated by a mixed decanethiol/mercaptohexanol partition layer. Anal Chem. 2005;77:6134-9.
[26] Ma K, Yuen JM, Shah NC, Walsh JT, Glucksberg MR, Van Duyne RP. In Vivo, Transcutaneous Glucose Sensing Using Surface-Enhanced Spatially Offset Raman Spectroscopy: Multiple Rats, Improved Hypoglycemic Accuracy, Low Incident Power, and Continuous Monitoring for Greater than 17 Days. Anal Chem. 2011;83:9146-52.
[27] Vangala K, Yanney M, Hsiao CT, Wu WW, Shen RF, Zou SG, et al. Sensitive Carbohydrate Detection Using Surface Enhanced Raman Tagging. Anal Chem. 2010;82:10164-71.
[28] Kawasaki T, Akanuma H, Yamanouchi TY. Increased fructose concentrations in blood and urine in patients with diabetes. Diabetes Care. 2002;25:353-7.
[29] Brownlee M. The pathobiology of diabetic complications - A unifying mechanism. Diabetes. 2005;54:1615-25.
[30] Bray GA, Nielsen SJ, Popkin BM. Consumption of high-fructose corn syrup in beverages may play a role in the epidemic of obesity. Am J Clin Nutr. 2004;79:537-43.
[31] James TD, Sandanayake KRAS, Shinkai S. Saccharide sensing with molecular receptors based on boronic acid. Angew Chem Int Edit. 1996;35:1910-22.
[32] Jin S, Cheng YF, Reid S, Li MY, Wang BH. Carbohydrate Recognition by Boronolectins, Small Molecules, and Lectins. Med Res Rev. 2010;30:171-257.
[33] Guo ZQ, Shin I, Yoon J. Recognition and sensing of various species using boronic acid derivatives. Chem Commun. 2012;48:5956-67.
[34] Cambre JN, Sumerlin BS. Biomedical applications of boronic acid polymers. Polymer. 2011;52:4631-43.
[35] Springsteen G, Wang BH. A detailed examination of boronic acid-diol complexation. Tetrahedron. 2002;58:5291-300.
[36] Baker GA, Desikan R, Thundat T. Label-free sugar detection using phenylboronic acid-functionalized piezoresistive microcantilevers. Anal Chem. 2008;80:4860-5.
[37] Ayyub OB, Ibrahim MB, Briber RM, Kofinas P. Self-assembled block copolymer photonic crystal for selective fructose detection. Biosens Bioelectron. 2013;46:124-9.

[38] Takahashi S, Anzai J. Phenylboronic acid monolayer-modified electrodes sensitive to sugars. Langmuir. 2005;21:5102-7.
[39] Lombardi JR, Birke RL, Lu TH, Xu J. Charge-Transfer Theory of Surface Enhanced Raman-Spectroscopy - Herzberg-Teller Contributions. J Chem Phys. 1986;84:4174-80.
[40] Wang JH, Hansen EH, Gammelgaard B. Flow injection on-line dilution for multi-element determination in human urine with detection by inductively coupled plasma mass spectrometry. Talanta. 2001;55:117-26.
[41] Yu QM, Guan P, Qin D, Golden G, Wallace PM. Inverted size-dependence of surface-enhanced Raman scattering on gold nanohole and nanodisk arrays. Nano Lett. 2008;8:1923-8.
[42] Yu QM, Braswell S, Christin B, Xu JJ, Wallace PM, Gong H, et al. Surface-enhanced Raman scattering on gold quasi-3D nanostructure and 2D nanohole arrays. Nanotechnology. 2010;21.
[43] Xu JJ, Zhang L, Gong H, Homola J, Yu QM. Tailoring Plasmonic Nanostructures for Optimal SERS Sensing of Small Molecules and Large Microorganisms. Small. 2011;7:371-6.
[44] Szafranski CA, Tanner W, Laibinis PE, Garrell RL. Surface-enhanced Raman spectroscopy of aromatic thiols and disulfides on gold electrodes. Langmuir. 1998;14:3570-9.
[45] Han SW, Lee SJ, Kim K. Self-assembled monolayers of aromatic thiol and selenol on silver: Comparative study of adsorptivity and stability. Langmuir. 2001;17:6981-7.
[46] Larkin P. Infrared and raman spectroscopy : principles and spectral interpretation. Amsterdam ; Boston: Elsevier; 2011.
[47] Moskovits M. Surface-enhanced Raman spectroscopy: a brief retrospective. J Raman Spectrosc. 2005;36:485-96.
[48] Centeno SP, Lopez-Tocon I, Roman-Perez J, Arenas JF, Soto J, Otero JC. Franck-Condon Dominates the Surface-Enhanced Raman Scattering of 3-Methylpyridine: Propensity Rules of the Charge-Transfer Mechanism under Reduced Symmetry. J Phys Chem C. 2012;116:23639-45.
[49] Wang TL, Chiang HK, Lu HH, Peng FY. Semi-quantitative surface enhanced Raman scattering spectroscopic creatinine measurement in human urine samples. Opt Quant Electron. 2005;37:1415-22.
[50] Wang H, Malvadkar N, Koytek S, Bylander J, Reeves WB, Demirel MC. Quantitative analysis of creatinine in urine by metalized nanostructured parylene. J Biomed Opt. 2010;15.
[51] Fu MD, Chen WP, Lu HC, Kuo CT, Tseng WH, Chen CH. Conductance of alkanediisothiocyanates: Effect of headgroup-electrode contacts. J Phys Chem C. 2007;111:11450-5.
[52] Pristinski D, Tan SL, Erol M, Du H, Sukhishvili S. In situ SERS study of Rhodamine 6G adsorbed on individually immobilized Ag nanoparticles. J Raman Spectrosc. 2006;37:762-70.
[53] Brandhorst G, Oellerich M, Maine G, Taylor P, Veen G, Wallemacq P. Liquid Chromatography-Tandem Mass Spectrometry or Automated Immunoassays: What Are the Future Trends in Therapeutic Drug Monitoring? Clin Chem. 2012;58:821-5.
[54] Nakanishi K, Miki A, Zaitsu K, Kamata H, Shima N, Kamata T, et al. Cross-reactivities of various phenethylamine-type designer drugs to immunoassays for

amphetamines, with special attention to the evaluation of the one-step urine drug test Instant-View (TM), and the Emit (R) assays for use in drug enforcement. Forensic Sci Int. 2012;217:174-81.
[55] Shipkova M, Petrova DT, Rosler AE, Orth M, Engelmayer J, Wieland E, et al. Comparability and imprecision of eight frequently used commercially available immunoassays for therapeutic drug monitoring. Ther Drug Monit. 2011;33:501-.
[56] Brandhorst G, Shipkova M, Rosler E, Orth M, Engelmayer J, Wieland E, et al. Comparability and Imprecision of Eight Frequently Used Commercially Available Immunoassays for Therapeutic Drug Monitoring. Clin Chem Lab Med. 2011;49:S830-S.
[57] Moore C. Oral fluid and hair in workplace drug testing programs: new technology for immunoassays. Drug Test Anal. 2011;3:166-8.
[58] Melanson SEF, Baskin L, Magnani B, Kwong TC, Dizon A, Wu AHB. Interpretation and Utility of Drug of Abuse Immunoassays Lessons From Laboratory Drug Testing Surveys. Arch Pathol Lab Med. 2010;134:735-9.
[59] Krasowski MD, Siam MG, Iyer M, Pizon AF, Giannoutsos S, Ekins S. Chemoinformatic Methods for Predicting Interference in Drug of Abuse/Toxicology Immunoassays. Clin Chem. 2009;55:1203-13.
[60] Krasowski MD, Siam MG, Iyer M, Ekins S. Molecular Similarity Methods for Predicting Cross-Reactivity With Therapeutic Drug Monitoring Immunoassays. Ther Drug Monit. 2009;31:337-44.
[61] Dasgupta A. Herbal supplements and therapeutic drug monitoring: Focus on digoxin immunoassays and interactions with St. John's wort. Ther Drug Monit. 2008;30:212-7.
[62] Melanson SEF, Lewandrowski EL, Griggs DA, Flood JG. Interpreting tricyclic antidepressant measurements in urine in an emergency department setting: Comparison of two qualitative point-of-care urine tricyclic antidepressant drug immunoassays with quantitative serum chromatographic analysis. J Anal Toxicol. 2007;31:270-5.
[63] Melanson SEF, Lee-Lewandrowski E, Griggs DA, Long WH, Flood JG. Reduced interference by phenothiazines in amphetamine drug of abuse immunoassays. Arch Pathol Lab Med. 2006;130:1834-8.
[64] Aslan K, Holley P, Geddes CD. Microwave-Accelerated Metal-Enhanced Fluorescence (MAMEF) with silver colloids in 96-well plates: Application to ultra fast and sensitive immunoassays, High Throughput Screening and drug discovery. J Immunol Methods. 2006;312:137-47.
[65] Marusich MF, Aggeler R, Bernal A, Murray J, Nadanaciva S, Willis J, et al. Quantitative analysis of mitochondrial protein levels, post-translational modifications and enzyme activities with rapid immunoassays suitable for basic research, pharmaceutical drug safety screening and diagnosis of mitochondrial disease. Bba-Bioenergetics. 2006:547-8.
[66] Dasgupta A, Tso G, Szelei-Stevens K. St. John's wart does not interfere with thereapeutic drug monitoring of 12 commonly monitored drugs using immunoassays. Journal of clinical laboratory analysis. 2006;20:62-7.
[67] Du HW, Yang WP, Xing WL, Su Y, Cheng J. Parallel detection and quantification using nine immunoassays in a protein microarray for drug from serum samples. Biomed Microdevices. 2005;7:143-6.
[68] Yan X, Zhang XJ, Yuan YX, Yao JL, Gu RA. SERS Detection and Magnetic Separation of Chromium(VI) Ions. Acta Chim Sinica. 2010;68:1267-71.

[69] Hardcastle A, Boxall K, Richards J, Tomlin P, Sharp S, Clarke P, et al. Solid-phase immunoassays in mechanism-based drug discovery: Their application in the development of inhibitors of the molecular chaperone heat-shock protein 90. Assay Drug Dev Techn. 2005;3:273-85.
[70] Paul A, Wells A, Dasgupta A. Stereospecificity of antibody: Quinine, the optical isomer of quinidine and anti-malaria drug chloroquine do not cross-react with quinidine immunoassays. Ther Drug Monit. 2000;22:174-6.
[71] Steinmann L, Thormann W. Characterization of competitive binding, fluorescent drug immunoassays based on micellar electrokinetic capillary chromatography. Electrophoresis. 1996;17:1348-56.
[72] Ezan E, Emmanuel A, Valente D, Grognet JM. Effect of variability of plasma interferences on the accuracy of drug immunoassays. Ther Drug Monit. 1997;19:212-8.
[73] My LN, Wuyts N, Luckins AG, Dung NA, Thanh NTG. Drug sensitivity of Trypanosoma evansi and the use of immunoassays in diagnosing infections with T-evansi in buffaloes in Vietnam. Tropical Veterinary Medicine. 1998;849:188-94.
[74] Bright SW, Tinsley FC, Dominianni SJ, Schmiegel KK, Fitch LL, Gold G. Competitive particle concentration fluorescence immunoassays for measuring anti-diabetic drug levels in mouse plasma. J Immunol Methods. 1997;207:23-31.
[75] Schlucker S. Surface-Enhanced Raman Spectroscopy: Concepts and Chemical Applications. Angew Chem Int Edit. 2014;53:4756-95.
[76] Belpomme D. Cancer and the environment: Facts, figures, methods and misinterpretations. Biomed Pharmacother. 2007;61:611-3.
[77] Deng Y, Idso MN, Galvan DD, Yu QM. Optofluidic microsystem with quasi-3 dimensional gold plasmonic nanostructure arrays for online sensitive and reproducible SERS detection. Anal Chim Acta. 2015;863:41-8.
[78] Lindquist NC, Nagpal P, McPeak KM, Norris DJ, Oh SH. Engineering metallic nanostructures for plasmonics and nanophotonics. Rep Prog Phys. 2012;75.
[79] Conermann T, Gosalia AR, Kabazie AJ, Moore C, Miller K, Fetsch M, et al. Utility of Oral Fluid in Compliance Monitoring of Opioid Medications. Pain Physician. 2014;17:63-70.
[80] ACS releases 2005 edition of Cancer Facts & Figures. Am Fam Physician. 2005;71:1612-.
[81] Brand R, Subramanian H, Roy HK, Hasabou N, Backman V. Pilot study examining changes induced in duodenal epithelial cells by different pancreatic diseases as measured by a novel optical imaging modality, single-cell partial wave spectroscopy microscopy. Gastroenterology. 2008;134:A93-A.
[82] Han XX, Zhao B, Ozaki Y. Surface-enhanced Raman scattering for protein detection. Anal Bioanal Chem. 2009;394:1719-27.
[83] Jarvis RM, Goodacre R. Characterisation and identification of bacteria using SERS. Chem Soc Rev. 2008;37:931-6.
[84] Xu JJ, Turner JW, Idso M, Biryukov SV, Rognstad L, Gong H, et al. In Situ Strain-Level Detection and Identification of Vibrio parahaemolyticus Using Surface-Enhanced Raman Spectroscopy. Anal Chem. 2013;85:2630-7.
[85] Vendrell M, Maiti KK, Dhaliwal K, Chang YT. Surface-enhanced Raman scattering in cancer detection and imaging. Trends Biotechnol. 2013;31:249-57.

[86] Bantz KC, Meyer AF, Wittenberg NJ, Im H, Kurtulus O, Lee SH, et al. Recent progress in SERS biosensing. Phys Chem Chem Phys. 2011;13:11551-67.
[87] Stewart A, Bell SEJ. Modification of Ag nanoparticles with mixed thiols for improved SERS detection of poorly adsorbing target molecules: detection of MDMA. Chem Commun. 2011;47:4523-5.
[88] Yang J, Palla M, Bosco FG, Rindzevicius T, Alstrom TS, Schmidt MS, et al. Surface-Enhanced Raman Spectroscopy Based Quantitative Bioassay on Aptamer-Functionalized Nanopillars Using Large-Area Raman Mapping. Acs Nano. 2013;7:5350-9.
[89] He LL, Lamont E, Veeregowda B, Sreevatsan S, Haynes CL, Diez-Gonzalez F, et al. Aptamer-based surface-enhanced Raman scattering detection of ricin in liquid foods. Chem Sci. 2011;2:1579-82.
[90] Kho KW, Dinish US, Kumar A, Olivo M. Frequency Shifts in SERS for Biosensing. Acs Nano. 2012;6:4892-902.
[91] Guarrotxena N, Bazan GC. Antitags: SERS-Encoded Nanoparticle Assemblies that Enable Single-Spot Multiplex Protein Detection. Adv Mater. 2014;26:1941-6.
[92] Pallaoro A, Braun GB, Reich NO, Moskovits M. Mapping Local pH in Live Cells Using Encapsulated Fluorescent SERS Nanotags. Small. 2010;6:618-22.
[93] Kneipp J, Kneipp H, Wittig B, Kneipp K. One- and two-photon excited optical pH probing for cells using surface-enhanced Raman and hyper-Raman nanosensors. Nano Lett. 2007;7:2819-23.
[94] Guerrini L, Pazos E, Penas C, Vazquez ME, Mascarenas JL, Alvarez-Puebla RA. Highly Sensitive SERS Quantification of the Oncogenic Protein c-Jun in Cellular Extracts. J Am Chem Soc. 2013;135:10314-7.
[95] Sun F, Bai T, Zhang L, Ella-Menye JR, Liu SJ, Nowinski AK, et al. Sensitive and Fast Detection of Fructose in Complex Media via Symmetry Breaking and Signal Amplification Using Surface-Enhanced Raman Spectroscopy. Anal Chem. 2014;86:2387-94.
[96] Zayak AT, Hu YS, Choo H, Bokor J, Cabrini S, Schuck PJ, et al. Chemical Raman Enhancement of Organic Adsorbates on Metal Surfaces. Phys Rev Lett. 2011;106.
[97] Wang FL, Widejko RG, Yang ZQ, Nguyen KT, Chen HY, Fernando LP, et al. Surface-Enhanced Raman Scattering Detection of pH with Silica-Encapsulated 4-Mercaptobenzoic Acid-Functionalized Silver Nanoparticles. Anal Chem. 2012;84:8013-9.
[98] Larmour IA, Graham D. Surface enhanced optical spectroscopies for bioanalysis. Analyst. 2011;136:3831-53.
[99] Holmlin RE, Chen XX, Chapman RG, Takayama S, Whitesides GM. Zwitterionic SAMs that resist nonspecific adsorption of protein from aqueous buffer. Langmuir. 2001;17:2841-50.
[100] Chen SF, Zheng J, Li LY, Jiang SY. Strong resistance of phosphorylcholine self-assembled monolayers to protein adsorption: Insights into nonfouling properties of zwitterionic materials. J Am Chem Soc. 2005;127:14473-8.
[101] Alvarez-Puebla RA, Aroca RF. Synthesis of Silver Nanoparticles with Controllable Surface Charge and Their Application to Surface-Enhanced Raman Scattering. Anal Chem. 2009;81:2280-5.
[102] Chretien JR. The Unscrambler, the software in Chemometrics - version 7.0 from CAMO company, Oslo, Norway. Analusis. 1998;26:M11-M2.

[103] Martens H. Multivariate calibration: John Wiley & Sons; 1989.
[104] Socrates G. Infrared and Raman characteristic group frequencies: tables and charts: John Wiley & Sons; 2004.
[105] Pigorsch E. Spectroscopic Characterisation of Cationic Quaternary Ammonium Starches. Starch-Starke. 2009;61:129-38.
[106] Graff M, Bukowska J. Adsorption of enantiomeric and racemic cysteine on a silver electrode - SERS sensitivity to chirality of adsorbed molecules. J Phys Chem B. 2005;109:9567-74.
[107] Briggs D. Surface analysis of polymers by XPS and static SIMS: Cambridge University Press; 1998.
[108] Barriet D, Yam CM, Shmakova OE, Jamison AC, Lee TR. 4-mercaptophenylboronic acid SAMs on gold: Comparison with SAMs derived from thiophenol, 4-mercaptophenol, and 4-mereaptobenzoic acid. Langmuir. 2007;23:8866-75.
[109] Tasevska N, Runswick SA, McTaggart A, Bingham SA. Urinary sucrose and fructose as biomarkers for sugar consumption. Cancer Epidem Biomar. 2005;14:1287-94.
[110] Ghiculescu R. Therapeutic drug monitoring: which drugs, why, when and how to do it. Aust Prescr. 2008;31:42-4.
[111] Anema JR, Li JF, Yang ZL, Ren B, Tian ZQ. Shell-Isolated Nanoparticle-Enhanced Raman Spectroscopy: Expanding the Versatility of Surface-Enhanced Raman Scattering. Annual Review of Analytical Chemistry, Vol 4. 2011;4:129-50.
[112] Taylor RD, MacCoss M, Lawson ADG. Rings in Drugs. J Med Chem. 2014;57:5845-59.
[113] Farquharson S, Shende C, Sengupta A, Huang H, Inscore F. Rapid detection and identification of overdose drugs in saliva by surface-enhanced Raman scattering using fused gold colloids. Pharmaceutics. 2011;3:425-39.
[114] Trachta G, Schwarze B, Sagmuller B, Brehm G, Schneider S. Combination of high-performance liquid chromatography and SERS detection applied to the analysis of drugs in human blood and urine. J Mol Struct. 2004;693:175-85.
[115] Andreou C, Hoonejani MR, Barmi MR, Moskovits M, Meinhart CD. Rapid Detection of Drugs of Abuse in Saliva Using Surface Enhanced Raman Spectroscopy and Microfluidics. Acs Nano. 2013;7:7157-64.
[116] Bonifacio A, Cervo S, Sergo V. Label-free surface-enhanced Raman spectroscopy of biofluids: fundamental aspects and diagnostic applications. Anal Bioanal Chem. 2015;407:8265-77.
[117] Bonifacio A, Dalla Marta S, Spizzo R, Cervo S, Steffan A, Colombatti A, et al. Surface-enhanced Raman spectroscopy of blood plasma and serum using Ag and Au nanoparticles: a systematic study. Anal Bioanal Chem. 2014;406:2355-65.
[118] Stosch R, Henrion A, Schiel D, Guttler B. Surface enhanced Raman scattering based approach for quantitative determination of creatinine in human serum. Anal Chem. 2005;77:7386-92.
[119] Zhang Z, Vaisocherova H, Cheng G, Yang W, Xue H, Jiang SY. Nonfouling Behavior of Polycarboxybetaine-Grafted Surfaces: Structural and Environmental Effects. Biomacromolecules. 2008;9:2686-92.
[120] Jiang SY, Cao ZQ. Ultralow-Fouling, Functionalizable, and Hydrolyzable Zwitterionic Materials and Their Derivatives for Biological Applications. Adv Mater. 2010;22:920-32.

[121] Bai T, Sun F, Zhang L, Sinclair A, Liu SJ, Ella-Menye JR, et al. Restraint of the Differentiation of Mesenchymal Stem Cells by a Nonfouling Zwitterionic Hydrogel. Angew Chem Int Edit. 2014;53:12729-34.
[122] Keefe AJ, Jiang SY. Poly(zwitterionic)protein conjugates offer increased stability without sacrificing binding affinity or bioactivity. Nature Chemistry. 2012;4:60-4.
[123] Zhang P, Sun F, Tsao C, Liu SJ, Jain P, Sinclair A, et al. Zwitterionic gel encapsulation promotes protein stability, enhances pharmacokinetics, and reduces immunogenicity. P Natl Acad Sci USA. 2015;112:12046-51.
[124] Lin D, Pan JJ, Huang H, Chen GN, Qiu SF, Shi H, et al. Label-free blood plasma test based on surface-enhanced Raman scattering for tumor stages detection in nasopharyngeal cancer. Sci Rep-Uk. 2014;4.
[125] Kurouski D, Postiglione T, Deckert-Gaudig T, Deckert V, Lednev IK. Amide I vibrational mode suppression in surface (SERS) and tip (TERS) enhanced Raman spectra of protein specimens. Analyst. 2013;138:1665-73.
[126] Harder P, Grunze M, Dahint R, Whitesides GM, Laibinis PE. Molecular conformation in oligo(ethylene glycol)-terminated self-assembled monolayers on gold and silver surfaces determines their ability to resist protein adsorption. J Phys Chem B. 1998;102:426-36.
[127] Ferguson BS, Hoggarth DA, Maliniak D, Ploense K, White RJ, Woodward N, et al. Real-Time, Aptamer-Based Tracking of Circulating Therapeutic Agents in Living Animals. Sci Transl Med. 2013;5.
[128] Desoize B, Robert J. Individual dose adaptation of anticancer drugs. Eur J Cancer. 1994;30A:844-51.
[129] Wright JD, Boudinot FD, Ujhelyi MR. Measurement and analysis of unbound drug concentrations. Clin Pharmacokinet. 1996;30:445-62.
[130] Gautier J, Munnier E, Douziech-Eyrolles L, Paillard A, Dubois P, Chourpa I. SERS spectroscopic approach to study doxorubicin complexes with Fe2+ ions and drug release from SPION-based nanocarriers. Analyst. 2013;138:7354-61.
[131] Chassany O, Urien S, Claudepierre P, Bastian G, Tillement JP. Comparative serum protein binding of anthracycline derivatives. Cancer chemotherapy and pharmacology. 1996;38:571-3.
[132] Nieciecka D, Krysinski P. Interactions of Doxorubicin with Self-Assembled Monolayer-Modified Electrodes: Electrochemical, Surface Plasmon Resonance (SPR), and Gravimetric Studies. Langmuir. 2011;27:1100-7.
[133] Tawde SR, Mukesh D, Yakhmi JV, Manohar C. Dye adsorption on self-assembled silane monolayers: optical absorption and modeling. J Mater Chem. 1999;9:1847-51.
[134] Preskorn SH, Dorey RC, Jerkovich GS. Therapeutic Drug-Monitoring of Tricyclic Antidepressants. Clin Chem. 1988;34:822-8.
[135] Shakya G, Mala S, Shakya KN, Shrestha R. Therapeutic Drug Monitoring of Antiepileptic Drugs. J Nepal Med Assoc. 2008;47:94-7.
[136] Goldman L, Schafer AI. Goldman-Cecil medicine. 25th edition. ed.
[137] Alvarez-Puebla RA, Liz-Marzan LM. SERS Detection of Small Inorganic Molecules and Ions. Angew Chem Int Edit. 2012;51:11214-23.
[138] Hinderling PH, Hartmann D. The pH dependency of the binding of drugs to plasma proteins in man. Ther Drug Monit. 2005;27:71-85.

[139] Sun F, Zhang P, Bai T, Galvan DD, Hung H-C, Zhou N, et al. Functionalized plasmonic nanostructure Arrays for direct and accurate mapping extracellular pH of living Cells in complex media using SERS. Biosensors and Bioelectronics. 2015.
[140] Sun F, Ella-Menye JR, Galvan DD, Bai T, Hung HC, Chou YN, et al. Stealth Surface Modification of Surface-Enhanced Raman Scattering Substrates for Sensitive and Accurate Detection in Protein Solutions. Acs Nano. 2015;9:2668-76.
[141] Prime KL, Whitesides GM. Self-Assembled Organic Monolayers - Model Systems for Studying Adsorption of Proteins at Surfaces. Science. 1991;252:1164-7.
[142] Ratner BD, Bryant SJ. Biomaterials: Where we have been and where we are going. Annu Rev Biomed Eng. 2004;6:41-75.
[143] Langer R. Perspectives: Drug delivery - Drugs on target. Science. 2001;293:58-9.
[144] Shapiro MG, Westmeyer GG, Romero PA, Szablowski JO, Kuster B, Shah A, et al. Directed evolution of a magnetic resonance imaging contrast agent for noninvasive imaging of dopamine. Nat Biotechnol. 2010;28:264-U120.
[145] Li LY, Chen SF, Jiang SY. Protein interactions with oligo(ethylene glycol) (OEG) self-assembled monolayers: OEG stability, surface packing density and protein adsorption. J Biomat Sci-Polym E. 2007;18:1415-27.
[146] Ostuni E, Chapman RG, Holmlin RE, Takayama S, Whitesides GM. A survey of structure-property relationships of surfaces that resist the adsorption of protein. Langmuir. 2001;17:5605-20.
[147] Ishihara K, Ueda T, Nakabayashi N. Preparation of Phospholipid Polymers and Their Properties as Polymer Hydrogel Membranes. Polym J. 1990;22:355-60.
[148] Iwasaki Y, Ishihara K. Phosphorylcholine-containing polymers for biomedical applications. Anal Bioanal Chem. 2005;381:534-46.
[149] Wu L, Jasinski J, Krishnan S. Carboxybetaine, sulfobetaine, and cationic block copolymer coatings: A comparison of the surface properties and antibiofouling behavior. J Appl Polym Sci. 2012;124:2154-70.
[150] Ladd J, Zhang Z, Chen S, Hower JC, Jiang S. Zwitterionic polymers exhibiting high resistance to nonspecific protein adsorption from human serum and plasma. Biomacromolecules. 2008;9:1357-61.
[151] Yang W, Xue H, Li W, Zhang JL, Jiang SY. Pursuing "Zero" Protein Adsorption of Poly(carboxybetaine) from Undiluted Blood Serum and Plasma. Langmuir. 2009;25:11911-6.
[152] Vaisocherova H, Yang W, Zhang Z, Cao ZQ, Cheng G, Piliarik M, et al. Ultralow fouling and functionalizable surface chemistry based on a zwitterionic polymer enabling sensitive and specific protein detection in undiluted blood plasma. Anal Chem. 2008;80:7894-901.
[153] von Muhlen MG, Brault ND, Knudsen SM, Jiang SY, Manalis SR. Label-Free Biomarker Sensing in Undiluted Serum with Suspended Microchannel Resonators. Anal Chem. 2010;82:1905-10.
[154] Li GZ, Cheng G, Xue H, Chen SF, Zhang FB, Jiang SY. Ultra low fouling zwitterionic polymers with a biomimetic adhesive group. Biomaterials. 2008;29:4592-7.
[155] Sundaram HS, Han X, Nowinski AK, Brault ND, Li YT, Ella-Menye JR, et al. Achieving One-Step Surface Coating of Highly Hydrophilic Poly(Carboxybetaine Methacrylate) Polymers on Hydrophobic and Hydrophilic Surfaces. Adv Mater Interfaces. 2014;1.

[156] Huang CJ, Brault ND, Li YT, Yu QM, Jiang SY. Controlled Hierarchical Architecture in Surface-initiated Zwitterionic Polymer Brushes with Structurally Regulated Functionalities. Adv Mater. 2012;24:1834-7.
[157] Xie LY, Hong F, He CX, Ma CF, Liu JH, Zhang GZ, et al. Coatings with a self-generating hydrogel surface for antifouling. Polymer. 2011;52:3738-44.
[158] Butruk B, Trzaskowski M, Ciach T. Fabrication of biocompatible hydrogel coatings for implantable medical devices using Fenton-type reaction. Mat Sci Eng C-Mater. 2012;32:1601-9.
[159] Rao L, Zhou HH, Li T, Li CY, Duan YWY. Polyethylene glycol-containing polyurethane hydrogel coatings for improving the biocompatibility of neural electrodes. Acta Biomater. 2012;8:2233-42.
[160] Mateescu A, Wang Y, Dostalek J, Jonas U. Thin hydrogel films for optical biosensor applications. Membranes. 2012;2:40-69.
[161] Faxalv L, Ekblad T, Liedberg B, Lindahl TL. Blood compatibility of photografted hydrogel coatings. Acta Biomater. 2010;6:2599-608.
[162] Toma M, Jonas U, Mateescu A, Knoll W, Dostalek J. Active Control of SPR by Thermoresponsive Hydrogels for Biosensor Applications. J Phys Chem C. 2013;117:11705-12.
[163] Tokarev I, Minko S. Stimuli-responsive hydrogel thin films. Soft Matter. 2009;5:511-24.
[164] Larsson A, Ekblad T, Andersson O, Liedberg B. Photografted poly(ethylene glycol) matrix for affinity interaction studies. Biomacromolecules. 2007;8:287-95.
[165] Larsson A, Liedberg B. Poly(ethylene glycol) gradient for biochip development. Langmuir. 2007;23:11319-25.
[166] Ekblad T, Bergstroem G, Ederth T, Conlan SL, Mutton R, Clare AS, et al. Poly(ethylene glycol)-Containing Hydrogel Surfaces for Antifouling Applications in Marine and Freshwater Environments. Biomacromolecules. 2008;9:2775-83.
[167] Masson JF, Battaglia TM, Davidson MJ, Kim YC, Prakash AMC, Beaudoin S, et al. Biocompatible polymers for antibody support on gold surfaces. Talanta. 2005;67:918-25.
[168] Wang Y, Brunsen A, Jonas U, Dostalek J, Knoll W. Prostate Specific Antigen Biosensor Based on Long Range Surface Plasmon-Enhanced Fluorescence Spectroscopy and Dextran Hydrogel Binding Matrix. Anal Chem. 2009;81:9625-32.
[169] Lewis AL, Tolhurst LA, Stratford PW. Analysis of a phosphorylcholine-based polymer coating on a coronary stent pre- and post-implantation. Biomaterials. 2002;23:1697-706.
[170] Li Y, Liu CM, Yang JY, Gao YH, Li XS, Que GH, et al. Anti-biofouling properties of amphiphilic phosphorylcholine polymer films. Colloid Surface B. 2011;85:125-30.
[171] Tang Y, Lu JR, Lewis AL, Vick TA, Stratford PW. Structural effects on swelling of thin phosphorylcholine polymer films. Macromolecules. 2002;35:3955-64.
[172] Yang W, Bai T, Carr LR, Keefe AJ, Xu JJ, Xue H, et al. The effect of lightly crosslinked poly(carboxybetaine) hydrogel coating on the performance of sensors in whole blood. Biomaterials. 2012;33:7945-51.
[173] Zhang L, Cao ZQ, Bai T, Carr L, Ella-Menye JR, Irvin C, et al. Zwitterionic hydrogels implanted in mice resist the foreign-body reaction. Nat Biotechnol. 2013;31:553-+.

[174] Nowinski AK, Sun F, White AD, Keefe AJ, Jiang SY. Sequence, Structure, and Function of Peptide Self-Assembled Monolayers. J Am Chem Soc. 2012;134:6000-5.
[175] Bai T, Liu SJ, Sun F, Sinclair A, Zhang L, Shao Q, et al. Zwitterionic fusion in hydrogels and spontaneous and time-independent self-healing under physiological conditions. Biomaterials. 2014;35:3926-33.
[176] Conermann T, Gosalia AR, Kabazie AJ, Moore C, Miller K, Fetsch M, et al. Utility of oral fluid in compliance monitoring of opioid medications. Pain Physician. 2014;17:63-70.
[177] Xu J, Kvasnička P, Idso M, Jordan RW, Gong H, Homola J, et al. Understanding the effects of dielectric medium, substrate, and depth on electric fields and SERS of quasi-3D plasmonic nanostructures. Optics express. 2011;19:20493-505.
[178] Sun F, Zhang P, Bai T, David Galvan D, Hung H-C, Zhou N, et al. Functionalized plasmonic nanostructure arrays for direct and accurate mapping extracellular pH of living cells in complex media using SERS. Biosensors and Bioelectronics. 2015;73:202-7.
[179] Richter AW, Akerblom E. Antibodies against Polyethylene-Glycol Produced in Animals by Immunization with Monomethoxy Polyethylene-Glycol Modified Proteins. Int Arch Aller a Imm. 1983;70:124-31.
[180] Armstrong JK, Hempel G, Koling S, Chan LS, Fisher T, Meiselman HJ, et al. Antibody against poly(ethylene glycol) adversely affects PEG-asparaginase therapy in acute lymphoblastic leukemia patients. Cancer-Am Cancer Soc. 2007;110:103-11.
[181] Ganson NJ, Kelly SJ, Scarlett E, Sundy JS, Hershfield MS. Control of hyperuricemia in subjects with refractory gout, and induction of antibody against poly(ethylene glycol) (PEG), in a phase I trial of subcutaneous PEGylated urate oxidase. Arthritis Res Ther. 2006;8.
[182] Yang Q, Lai SK. Anti-PEG immunity: emergence, characteristics, and unaddressed questions. Wires Nanomed Nanobi. 2015;7:655-77.
[183] Saifer MGP, Williams LD, Sobczyk MA, Michaels SJ, Sherman MR. Selectivity of binding of PEGs and PEG-like oligomers to anti-PEG antibodies induced by methoxyPEG-proteins. Mol Immunol. 2014;57:236-46.
[184] Liu YJ, Reidler H, Pan J, Milunic D, Qin DJ, Chen D, et al. A double antigen bridging immunogenicity ELISA for the detection of antibodies to polyethylene glycol polymers. J Pharmacol Tox Met. 2011;64:238-45.
[185] Rodriguez-Emmenegger C, Hasan E, Pop-Georgievski O, Houska M, Brynda E, Alles AB. Controlled/Living Surface-Initiated ATRP of Antifouling Polymer Brushes from Gold in PBS and Blood Sera as a Model Study for Polymer Modifications in Complex Biological Media. Macromol Biosci. 2012;12:525-32.

Curriculum Vitae

Fang Sun was born in Tianjin, China. He received his Bachelor of Engineering in Chemical Engineering at Tianjin University in Tianjin, China, in 2011, and his Master's in Chemical Engineering at University of Washington in Seattle, WA in 2013. In 2016, he is expected to receive his Doctor of Philosophy in Chemical Engineering at the University of Washington.

Publications:

1. **Sun, F.***, Hung, H.C.*, Sinclair, A., Zhang, P., Tao, B., Galvan, D.D., Jain, P., Li, B., Jiang, S. and Yu, Q., 2016. Hierarchical zwitterionic modification of a SERS substrate enables real-time drug monitoring in blood plasma. *Nature Communication*, accepted.

2. Chou, Y.N.*, **Sun, F.***, Hung, H.C., Jain, P., Sinclair, A., Zhang, P., Bai, T., Chang, Y., Wen, T.C., Yu, Q. and Jiang, S., 2016. Ultra-low fouling and high antibody loading zwitterionic hydrogel coatings for sensing and detection in complex media. *Acta biomaterialia*, *40*, pp.31-37.

3. **Sun, F.**, Zhang, P., Bai, T., Galvan, D.D., Hung, H.C., Zhou, N., Jiang, S. and Yu, Q., 2015. Functionalized plasmonic nanostructure arrays for direct and accurate mapping extracellular pH of living cells in complex media using SERS. *Biosensors and Bioelectronics*, *73*, pp.202-207.

4. **Sun, F.**, Ella-Menye, J.R., Galvan, D.D., Bai, T., Hung, H.C., Chou, Y.N., Zhang, P., Jiang, S. and Yu, Q., 2015. Stealth surface modification of surface-enhanced Raman scattering substrates for sensitive and accurate detection in protein solutions. *ACS nano*, *9*(3), pp.2668-2676.

5. **Sun, F.**, Bai, T., Zhang, L., Ella-Menye, J.R., Liu, S., Nowinski, A.K., Jiang, S. and Yu, Q., 2014. Sensitive and fast detection of fructose in complex media via symmetry breaking and signal amplification using surface-enhanced Raman spectroscopy. *Analytical chemistry*, *86*(5), pp.2387-2394.

6. Galvan, D.D., Špačková, B., Slabý, J., **Sun, F.**, Ho, Y.H., Homola, J. and Yu, Q., 2016. Surface-enhanced Raman scattering (SERS) on gold nanohole arrays in symmetrical dielectric environments exhibiting electric field extension. *The Journal of Physical Chemistry C*, in press.

7. Zhang, P., **Sun, F.**, Liu, S. and Jiang, S., 2016. Anti-PEG antibodies in the clinic: Current issues and beyond PEGylation. *Journal of Controlled Release*, in press.

8. Zhang, P., Jain, P., Tsao, C., Sinclair, A., **Sun, F.**, Hung, H.C., Bai, T., Wu, K. and Jiang, S., 2016. Butyrylcholinesterase nanocapsule as a long circulating

bioscavenger with reduced immune response. *Journal of Controlled Release*, *230*, pp.73-78.

9. Wei, Y., Hung, H.C., **Sun, F.**, Bai, T., Zhang, P., Nowinski, A.K. and Jiang, S., 2016. Achieving low-fouling surfaces with oppositely charged polysaccharides via LBL assembly. *Acta biomaterialia*, *40*, pp.16-22.

10. An, J., Guo, Q., Zhang, P., Sinclair, A., Zhao, Y., Zhang, X., Wu, K., **Sun, F.**, Hung, H.C., Li, C. and Jiang, S., 2016. Hierarchical design of a polymeric nanovehicle for efficient tumor regression and imaging. *Nanoscale*, *8*(17), pp.9318-9327.

11. Bai, T., Sinclair, A., **Sun, F.**, Jain, P., Hung, H.C., Zhang, P., Ella-Menye, J.R., Liu, W. and Jiang, S., 2016. Harnessing isomerization-mediated manipulation of nonspecific cell/matrix interactions to reversibly trigger and suspend stem cell differentiation. *Chemical Science*, *7*(1), pp.333-338.

12. Zhang, P., **Sun, F.**, Tsao, C., Liu, S., Jain, P., Sinclair, A., Hung, H.C., Bai, T., Wu, K. and Jiang, S., 2015. Zwitterionic gel encapsulation promotes protein stability, enhances pharmacokinetics, and reduces immunogenicity. *Proceedings of the National Academy of Sciences*, *112*(39), pp.12046-12051.

13. Wen, Y., Yao, F., **Sun, F.**, Tan, Z., Tian, L., Xie, L. and Song, Q., 2015. Antibacterial action mode of quaternized carboxymethyl chitosan/poly (amidoamine) dendrimer core–shell nanoparticles against Escherichia coli correlated with molecular chain conformation. *Materials Science and Engineering: C*, *48*, pp.220-227.

14. Bai, T., **Sun, F.**, Zhang, L., Sinclair, A., Liu, S., Ella-Menye, J.R., Zheng, Y. and Jiang, S., 2014. Restraint of the differentiation of mesenchymal stem cells by a nonfouling zwitterionic hydrogel. *Angewandte Chemie International Edition*, *53*(47), pp.12729-12734.

15. Bai, T., Liu, S., **Sun, F.**, Sinclair, A., Zhang, L., Shao, Q. and Jiang, S., 2014. Zwitterionic fusion in hydrogels and spontaneous and time-independent self-healing under physiological conditions. *Biomaterials*, *35*(13), pp.3926-3933.

16. Wen, Y., Tan, Z., **Sun, F.**, Sheng, L., Zhang, X. and Yao, F., 2012. Synthesis and characterization of quaternized carboxymethyl chitosan/poly (amidoamine) dendrimer core–shell nanoparticles. *Materials Science and Engineering: C*, *32*(7), pp.2026-2036.

17. Nowinski, A.K., **Sun, F.**, White, A.D., Keefe, A.J. and Jiang, S., 2012. Sequence, structure, and function of peptide self-assembled monolayers. *Journal of the American Chemical Society*, *134*(13), pp.6000-6005.

18. White, A.D., Nowinski, A.K., Huang, W., Keefe, A.J., **Sun, F.** and Jiang, S., 2012. Decoding nonspecific interactions from nature. *Chemical Science*, *3*(12), pp.3488-3494.